The electronic and experimental setup of the MAIUS-2 and MAIUS-3 sounding rocket missions

Von der QUEST-Leibniz Forschungsschule
der Gottfried Wilhelm Leibniz Universität Hannover zur Erlangung des Grades

Doktor der Naturwissenschaften

- Dr. rer. nat. -

genemigte Dissertation von

Wolfgang Bartosch, M.Sc.

Erscheinungsjahr: **2021**

Referent:	Prof. Dr. rer. nat. Ernst Maria Rasel Institut für Quantenoptik, Leibniz Universität Hannover
Koreferent:	Prof. Dr. rer. nat. Claus Braxmaier Institut für Quantentechnologien, Universität Ulm
Koreferent:	Dr. rer. nat. Dennis Schlippert Institut für Quantenoptik, Leibniz Universität Hannover
Tag der Disputation:	27.09.2021

Abstract

Finding a unified theory of the physical forces is an important part of research to this day. The standard model of particle physics is fundamentally incompatible with Einstein's general theory of relativity. An approach to the unification of both theories is the string theory which may allow for new forces, leading to an apparent a violation of the equivalence principle. The equivalence principle can be tested by comparing the free fall of test masses with precisely known gravitational mass. Besides other techniques for this tests like lunar laser ranging and torsion balances, atom interferometers pose an approach to this challenge.
They are independent from mechanical machined test masses and they test the equivalence principle with quantum mechanical systems. The sensitivity of an atom interferometer depends strongly on the free evolution time T of the coherently split atomic ensemble. The T-value of an atom interferometer is proportional to the possible free-falling time of the atomic cloud. This time can be increased by building an apparatus with a large base line, levitation of the atomic cloud or by moving the experiment into a microgravity environment.
This work focuses on the microgravity approach and on how to build the electronic system for such an atom interferometer for the MAIUS-2 mission. This system must be able to operate the atom interferometer on the sounding rocket without human interaction. In this thesis, the challenges, the autonomous operation of an atom interferometer on a sounding rocket poses on the design of the electronic system, will be discussed.
This thesis presents miniaturized electronic components like current drivers, microwave sources and low noise power supply devices, that can compete with lab filling systems and are ready for the operation on a sounding rocket. Key design parameters for the system will be derived and tested. Some of these parameters are restrictions due to the operational environment of the sounding rocket. Others are derived from the atom interferometer. The challenge is finding a careful balance between the limits of miniaturization and the strict requirements of the experiments. This work builds up on the achievements of the MAIUS-1 mission, that created the first rubidium 87 Bose-Einstein-Condensate (BEC) in space, in 2017. It adds Potassium as a second species, while maintaining size and mass of the apparatus. The overall electronic system of the MAIUS-2 sounding rocket mission will be presented.
A strong focus will be on the development of a microwave evaporation system for both atomic species. This system is small enough to be feasible for the operation on a sounding rocket. At the same time it is ultra low noise while being electromagnetically compatible with the operation close to the experiment. Another important part of this work is the investigation of how noise in the chip wires impacts the performance of the experiment to derive upper limits for the noise spectrum of future devices. The microwave system as well as the current drivers can only operate using a low noise power source which is also described here. This work paves the way for future space born atom interferometer experiments by building an requirements catalog for miniaturized, precision, metrology electronics for the autonomous operation of an atom inteferometers in space.

Key words: **atom interferometer**, **electronics**, **microgravity**

Kurzfassung

Das Finden einer universellen Theorie der physikalischen Grundkräfte stellt einen großen Teil der Anstrengungen der fundamentalen Physik im letzten Jahrzehnt dar. Das Standartmodell der Teilchenphysik scheint mit Einsteins Relativitätstheorie fundamental unvereinbar. Einen möglichen Ansatz, beide Theorien zu vereinigen stellt die String Theorie da. Diese erlaubt allerdings neue kräfte welche zu einer Verletzung der Universalität des freien Falls führen können. Die Universalität des freien falls kann beispielsweise mittels lunar Laser ranging oder Torsionswaagen, aber auch mit Atominterferometern getestet werden. Letztere sind unabhängig von Imperfektionen mechanischer Fertigung der getesteten Massen und sie verwenden quantenmechanische Testmassen. Die Sensitivität eines sochen Atominterferometers hängt stark von der freien Entwicklungszeit eines kohärent geteilten atomaren Ensembles ab. Diese wiederum kann vergrößert werden, indem die Probe zum Schweben gebracht wird, indem man den Testapparat vergrößert oder indem der Test in Mikrogravitation durchgeführt wird.
Diese Arbeit fokussiert sich auf den letzteren Ansatz und darauf wie man ein Elektroniksystem, welches in der Lage ist ein Atominterferometer autonom auf der Höhenforschungsraketenmission MAIUS-2, ohne menschliches eingreifen zu steuern, bauen kann.
Die Herausforderungen welche die experimentelle Umgebung der Höhenforschungsrakete an das Elektroniksystem stellt, werden in dieser Arbeit diskutiert. Miniaturisierte Elektronikkomponenten, welche für ein solches Experiment nötig sind, wie Stromtreiber, Mikrowellen quellen und rauscharme Spannungsquellen, welche mit Laboraufbauten konkurrieren können, werden im Rahmen dieser Arbeit vorgestellt.
Schlüsselparameter für das Design solcher Komponenten werden, einerseits von den Anforderungen der Höhenforschungsrakte und andererseits denen des Experimentes hergeleitet. Dies stellt immer eine Gradwanderung zwischen Miniaturisierung und der best möglichen Performance des Geräts da, für diese hier ein Leitfaden geschaffen wird. Diese Arbeit baut auf den Erfolgen der MAIUS-1 Mission auf, welche 2017 das erste Rubidium 87 Bose-Einstein-Condensate (BEC) im Weltraum erzeugt hat, und erweitert deren Möglichkeiten um eine zweite atomare Spezies: Kalium. Dabei ändern sich Masse und Größe des Elektroniksystems und des experimentellen Aufbaus nicht wesentlich. Das komplette hierfür entwickelte Elektroniksystem wird in dieser Arbeit vorgestellt. Dabei wird verstärkt ein Augenmerk auf das System zur Mikrowellenevaporation von Rubidium und Kalium gelegt. Ein weiter Fokus wird die Untersuchung der Empfindlichkeit des Experimentes gegenüber Störungen in den Strömen des Atom Chips sein um obere Schranken für die Rauschintensität zukünftiger Komponenten festlegen zu können. Diese Arbeit legt den Grundstein für zukünftige Atominterferometer Experimente im Weltraum, indem ein Anforderungskatalog für miniaturisierte, präzisionsmesstechnische elektronische Systeme, solcher Apparate erstellt wird.

Schlüsselwörter: **Atominterferometer**, **Elektronik**, **Mikrogravitation**

Contents

List of Figures

CHAPTER 1

Introduction

The scientific method has been the base of fundamental research since the 17th century[1]. This method is a frame of 5 steps that is used to gain knowledge of nature. The steps are:

1. Form a question
2. Research
3. Form a hypothesis
4. Experiment (Test the hypothesis)
5. Analyze the results

In this scheme there is a feedback loop between the steps 5 and 3. Based on the analysis of the experimental results the hypothesis can be found confirmed or rejected. That makes a reliable and replicable experiment our best and only way to determine if a hypothesis is true or false [69] and thus to gain knowledge of nature. Therefore, measuring experimental results to the maximum of what is possible in accuracy, is almost as important as the experiment itself.
The way we measure experimental results has changed dramatically over the last centuries, from naked eye observation to high precision optoelectronic methods in some cases. Also, the experimental setups evolved from mostly mechanical or optical setups to enormous setups of lasers, vacuum technology and electronics.
This thesis is focused on a specific type of experimental setup, an atom interferometer. Such an interferometer is an apparatus using a variety of technologies, metrological methods and electronic control engineering to the limit of what is possible. An atom interferometer usually needs several lasers and every single one of this lasers needs electronic support like current drivers, thermoelectric coolers, photodiodes for detection and precision control loops for frequency stabilization. Because in the process of cooling down the atoms to the recoil limit one will need coherent light of a very narrow wavelength stabilized to the atomic transition. In this case one is operating at the limit of what is physically achievable and also on the limit of what is technically possible to produce and to measure. For an experiment operating in zero gravity environments without a human operator this challenge becomes even bigger. Experiments of this kind rely completely on their measuring and control electronics. In fact, the whole experiment is done by an electronic system since no human can survive to fly on a

[1] It is not clear when exactly the scientific method arose. Some sources name Aristotle [16] however even early cultures like the Egyptians had a similar scientific methodology [13]. In 1687 Newton published his Philosophiae Naturalis Principia Mathematica, there he mentioned four rules of reasoning quite similar to the modern scientific method [58]. Since then the scientific method got improved and reformulated to its modern form. Up to now it is a controversial discussion whether there is a universal scientific method or not [90].

small sounding rocket vessel. Even though this kind of electronic metrology of such an experiment is an essential part of the experiment it is not yet a standard part of a physicist's education to create such devices. Since every current, and every voltage in such a system has direct influence on the experiment, a person designing the system needs to have the knowledge of the physical part of the experiment and the skills to design the electronics.
In this thesis an autonomous control and metrology system for a dual species atom interferometry on a sounding rocked, is created. Since there are almost no commercial parts available most of the major components are extensive custom developments.

1.1 The universality of the free fall

Finding a unified theory of the physical forces is an important part of research in the last decades [30]. On the one hand the standard model of particle physics is capable of explaining processes in the atomic nucleus and predict a variety of observations in particle physics. On the other hand the standard model is fundamentally incompatible with Einstein's general theory of relativity [22] that explains gravity as a geometric property of space-time. The theory of general relativity was capable of predicting observed phenomena like gravitational waves [2]. Besides the problem of the unification of these two theories there are also observations that cannot be explained by any of them. For example, the accelerated expansion on the universe. That is today explained by the existence of dark energy [41].
One approach to unify general relativity and the standard model is the string theory [11]. The string theory allows for a violation of the weak equivalence principle. The weak equivalence principle arose from the general relativity and it demands the equivalence of gravitational and inertial mass. The weak equivalence principle postulates the universality of the free fall. That means that by testing the universality of the free fall one can determine upper limits to the validity of the weak equivalence principle and get closer to answering the unification question.
The universality of the free fall can be tested by comparing the free fall of test masses with precisely known gravitational mass. The result of such a comparison can be expressed with the Eötvös-ratio η:

$$\eta = \left| \frac{g_a - g_b}{(g_a + g_b)/2} \right| \tag{1.1}$$

were g_a is the gravitational acceleration for a body a and g_b for a body b. The Eötvös-ratio is named after Loránd Eötvös who performed early measurements of the universality of the free fall using torsion balances in 1922 [88]. Since the early measurements of the universality of the free fall the torsion balances improved. Modern forms of the torsion balance, using beryllium and titanium, were able to measure the Eötvös-ratio to a limit of $(0.3 \pm 1.8) \cdot 10^{-13}$ [76]. One new method of measuring the universality of the free fall is the lunar laser ranging experiment [91]. In the lunar laser ranging experiment the distance between earth and moon is measured using laser light reflected by mirrors on the moon's surface. With this technique the Eötvös-ratio can be calculated to a limit of $(0.8 \pm 1.3) \cdot 10^{-13}$ [12].
A Space born classical test of the universality of the free fall was performed in the MICROSCOPE experiment using titanium and platinum, it measured the Eötvös-ratio to a limit of 10^{-15} [86].
Even though new methods for testing the universality of the free fall arose, like the lunar laser ranging experiment [91], the so far most accurate way is still the comparison

the free fall of classical test masses and thus strongly dependent on the precise knowledge of the gravitational mass of this test masses. How good this mass is known depends on the purity and geometry of the test masses. Also, there is a dependency on how well distances and mirror placements for the detection laser interferometer can be known. Atom interferometers utilize test masses that are perfectly isotope-pure and their mass can be calculated by the atomic mass of the isotopes. They also use quantum mechanical test masses to test a phenomenon associated with the general relativity. That makes them an important third tool for measuring the universality of the free fall. Atom interferometers are also a good example of modern experiments that utilize a variety of different technologies and electronic metrology methods.

1.2 Atom interferometers

In the last decade atom interferometers have made their way into various fields of research. They have become an applied tool in precision metrology, fundamental research, molecular physics [15] and earth science [78]. This thesis is focused on atom interferometer applications in precision metrology for the measurement of the universality of the free fall in microgravity. Most of the techniques and electronics covered in this work can be applied for atom interferometers used for other applications.
Since an atom interferometer utilizes the quantum wave nature of solid particles [66], that can be manipulated with matter-wave optics (laser pulses), it is independent from human made test masses and human measured distances for spaces, in the core of its working principle. Also using ultra cold atoms as test masses it is possible to observe the test masses at the exact same point in space. Due to these facts atom interferometers are not only a complementary method for measurements of the universality of the free fall, they can potentially outperform classical methods. In an atom interferometer an ensemble of ultra cold atoms is coherently split, mirrored and recombined using laser pulses. The atom interferometer considered in this thesis is a Mach-Zehnder-type configuration. Where the initial cloud of ultra cold atoms is considered to be a three-level quantum system $|g\rangle$, $|+e\rangle$ and $|-e\rangle$ which is, when exposed to a light field, capable of rabi-oscillations between the exited states. The necessary steps to create such an ensemble of ultra cold atoms will be part of chapter 3. To form the Mach-Zehnder-inteferometer the ensemble of ultra cold atoms, which is initially in the momentum free $|g\rangle$-state, is first splitted into the two non-zero-momentum states ($|-e\rangle$ and $|+e\rangle$) using a $\pi/2$-pulse. This $\pi/2$-pulse acts similar to an optical beam splitter. After half of the free evolution time T has passed the momentum of the two atomic clouds is inverted by a π-pulse. This π-pulse is analog to a mirror in an optical interferometer. After the full free evolution time T has passed the interferometer is closed using another $\pi/2$-pulse. This Mach-Zender-type interferometer configuration is illustrated in figure 1.1. After recombining the atomic clouds, the state population can be measured with absorption or fluorescence spectroscopy. From the population P of the output states the phase-shift $\Delta\phi$ of the interferometer can be calculated using:

$$P = \frac{1}{2} \cdot (1 + K \cdot cos(\Delta\phi)) \tag{1.2}$$

were K is the contrast of the measurement. From this phase difference the acceleration acting on the atomic clouds can be calculated using:

$$\Delta\phi = \vec{k}_{eff} \cdot \vec{a} \cdot T^2 \tag{1.3}$$

were $\vec{k}_{eff}$ is the effective wave vector of the laser light.
Until today the development of atom interferometers is still in an early state of research

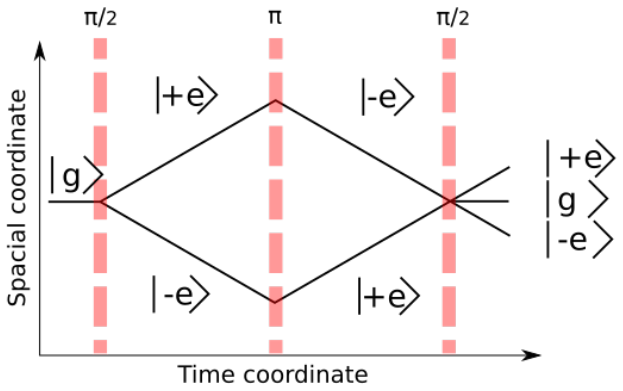

Figure 1.1: Schematic picture of a matter wave Mach-Zehnder-interferometer setup for a system at rest. The initial state $|g\rangle$ is splitted by a laser pulse at time $t = 0$, mirrored at time $t = T$ and recombined at time $t = 2T$. The trajectory is shown for a system at rest. From the difference in the probability of occupancy of the outgoing states one can obtain the relative phase $\Delta\Phi$. [33]

and measurements of the Eötvös-ratio comparing different atomic species reach a limit of $(0.3 \pm 5.5) \cdot 10^{-7}$ [77]. Tests utilizing a single species atom interferometer and a classical gravimeter however reach a lower limit of $(4.4 \pm 6.5) \cdot 10^{-9}$ [47]. However, these kind of measurements face the same challenges regarding the classical test mass as the purely classical measurements. So far the best classical test reached a precision of $1.3 \cdot 10^{-14}$ [86].
It is clear from equation 1.3 that the sensitivity of an atom interferometer is strongly dependent on the free evolution time T of the coherently split atomic ensemble. The free evolution time of an atom interferometer is proportional to the possible free-falling time of the atomic cloud squared. The possible free-falling time of the atomic cloud in an atom interferometer can be increased in three ways. One way is to increase the baseline of the apparatus. This is planned for example with the VLBAI-Experiment [67]. The free evolution time of the atomic ensemble can also be increased by enforced magnetic levitation of the ensemble [20]. Another way is to move the atom interferometer into a microgravity environment. Microgravity environments allow long free evolution times with a small overall experiment size but many challenges arise while building an atom interferometer for microgravity environments. A discussion of the technical challenges will be part of this thesis. A third way to increase the free evolution time is to create a levitation system. Experiments using this technique are then restricted to the use of a single atomic species due to differing magnetic moments [32].

1.3 The QUANTUS/MAIUS experimental family

The project: "Quantengase unter Schwerelosigkeit (QUANTUS)" was founded to research the development of sources for ultracold atoms and their application in atom interferometers for microgravity environments. The goal of QUANTUS was to demonstrate the operation of an atom interferometer in microgravity to enable future missions in earth orbit. Since the way to a facility in earth orbit leads through various steps of ground based tests, the studies were started in the drop-tower in Bremen. The drop tower can provide 110 m of free fall in vacuum, leading to a microgravity time of 4.7 s. The drop-tower can also provide a catapult-mode, leading to 9 s of maximum possible microgravity time. The QUANTUS-1 apparatus showed the first Bose-Einstein-Condensate (BEC) in microgravity in the the drop-tower [89]. The research

with the QUANTUS-1 apparatus is now continued with the QUANTUS-2 apparatus with the goal to show a dual species atom interferometer with ^{87}Rb and ^{41}K in microgravity [33]. Parallel to the development of the QUANTUS-2 apparatus the MAIUS project started. The MAIUS project was aimed towards an atom interferometer on a sounding rocket, as the next logical step towards an orbital platform. The MAIUS-1 sounding rocket mission carried the MAIUS-A apparatus that created the first Bose-Einstein-Condensate in space on the 23th of January in 2017 on a VSB30 sounding rocket. The MAIUS-1 mission will be followed by the MAIUS-2 and 3 missions, both carrying the MAIUS-B apparatus. The MAIUS-B apparatus is supposed to show a sequential dual species atom interferometer in space during its first launch, followed by a demonstration of a parallel atom interferometer on its second launch. The MAIUS-B apparatus is using a ^{87}Rb and ^{41}K similar to the QUANTUS-2 apparatus. A successor experiment of the MAIUS experiments is planned on the International Space Station (ISS) also using ^{87}Rb and ^{41}K, by a collaboration of the National Aeronautics and Space Administration (NASA) and the Deutsches Zentrum für Luft- und Raumfahrt (DLR) called Bose Einstein Condensates and Cold Atom Laboratory (BECCAL). Even thoug this thesis focus is on the MAIUS-B mission, some of the technologies presented in this thesis are developments used for MAIUS and BECCAL. Some design decisions made may only be explained by possible use in BECCAL after the MAIUS-2 mission. Many of the electronic technologies used in all the experiments of the experimental family and for other experiments, are created within the Laser Unter Schwerelosigkeit (LASUS) project. Details on the LASUS project and the technologies that arose from it can be found in section 5.2.

1.4 The scope of this thesis

This thesis is focused on the technical challenges that arise from the task of building an dual species atom interferometer for a sounding rocket for the MAIUS-2 mission. Some of the main challenges are downsizing the technology from the MAIUS-A apparatus to fit a second species and its support electronics in an experiment of roughly the same size and mass while maintaining or improving the functionality. Also, there are technical challenges that are based on the sounding rocket, like autonomous experiment operation and vibration hardness of the components. This thesis will discuss these challenges and the solutions for them.
This work was done within the development of the MAIUS-B apparatus. In chapter 2, the setup and the results of the MAIUS-1 mission will be reviewed regarding design guidelines for the MAIUS-B electronic system. It will also lay out the the scientific goals of the MAIUS-2 sounding rocket mission and present an overview of their technical implications for the design of the MAIUS-B electronic system.
Alongside with an overview of the whole experimental setup of the MAIUS-2 mission, including laser-system and vehicle information, chapter 3 will provide a theoretical explanation of the techniques used to create the ultra-cold atomic ensemble.
Chapter 4 will extend the theoretical background given, by a more detailed description of the magnetic trapping of neutral atoms and possible loss and heating rates from magnetic traps.
After design goals for the electronic system have been derived and explained in the chapters 3 and 4, chapter 5 will give a detailed description of the whole electronic system created for the MAIUS-2 mission.
This chapter will also present the precision metrology electronics fit to control an atom interferometer autonomously, that had to be developed during this work.

Chapter 6.5 will add a more detailed description of the microwave evaporation system to chapter 5.
In chapter 7, measurements concerning the performance of the flight system compared to the ground system of the MAIUS-B apparatus and the MAIUS-A apparatus will be shown. This measurements include the characterization of the microwave evaporation system, the analysis of the effects of spurious and phase noise in the microwave source on the phase transition to BEC state for rubidium 87 and measurements of atom loss and heating rates from a magnetic trap for different noise spectra in the atom chip wires. In section 8 these results will be evaluated with regard to the scientific goals.
The appendix will, among other things, contain some of the schematics of most critical components designed for the electronic system as well as the most important firmware modules.

CHAPTER 2

The MAIUS sounding rocket missions

In this chapter an overview of the MAIUS sounding rocket missions and their scientific goals is provided. After a brief introduction of the QUANTUS/MAIUS experiment family in chapter 1 this chapters focus will be the MAIUS missions. Like already mentioned in the introduction, the MAIUS missions are sounding rocket missions that are probing technologies for atom interferometers in microgravity environments. The missions are showing feasibility, testing technology and show important experimental results like the first demonstration of a BEC in space. The MAIUS-1 mission carrying the MAIUS-A apparatus successfully launched in 2017 from the Esrange Space Center in Kiruna (Sweden) on a VSB-30 rocket. This chapter will start with a vehicle description of the VSB-30 rocket that is also planned to be used for the MAIUS-2 mission, to evaluate this target platform, followed by an overview on this first mission's goals and results. After covering the MAIUS-1 mission it will provide an overview of the MAIUS-2/3 sounding rocket mission and the MAIUS-B apparatus. This chapter will briefly cover the flight configuration of the rockets and the scientific payload and lay out the scientific goals of each mission.

2.1 The VSB-30 sounding rocket

The microgravity platform chosen for the MAIUS missions is the sounding rocket. A sounding rocket is a logical step between ground based microgravity solutions like drop towers and orbital facilities like the International Space Station (ISS) and free flying platforms. It can provide microgravity times in the order of minutes, instead of seconds in a drop tower while being cost efficient compared to a satellite mission. Also sounding rockets are a good way to prove the readiness of an experiment for space applications, since the environmental challenges of a sounding rocket launch are a good first test regarding the hardness of the start of a typical low orbit transportation vessel. For the MAIUS missions the VSB-30 sounding rocket was chosen. With its comparable high apogee to payload mass ratio it was the ideal candidate for the MAIUS missions. The VSB-30 rocket is a two stage solid propellant rocket. This rocket type was developed by the Brazilian aerospace agency (IAE) in cooperation with the Deutsches Zentrum für Luft- und Raumfahrt (DLR). The VSB-30 rocket is specified with an apogee of 282 km while carrying 400 kg of scientific payload and an overall lift off mass off 2579 kg. This leads to a micro-gravity time of 489 s[1] [60]. The rocket has a maximum acceleration of 12 g with a peak vibrational acceleration of 2 g during flight.
The first motor stage is a S-31 motor with a lift off mass of 1236 kg (with fins) and an

[1] specified as time in microgravity is the time in space above 110 km

overall length of 3.2 m. This stage contains 677 kg of HTPB/AP/Al solid propellant fuel leading to a burning time of 11.2 ± 0.5 s with 241 ± 23 kN of maximum thrust. The second stage is a S-30 motor with a lift of mass of 1218 kg and an overall length of 3.29 m. This stage contains 898 kg of the same solid state propellant as the S-31 motor, leading to a burning time of 19 ± 1 s with 108 ± 5 kN of maximum thrust. The vibrational spectra during a flight is shown in appendix A.2. The acceleration during the flight pose a major design criteria for the development of the payload. The physics package as well as the electronic modules need to be able to withstand the 12 g of motor acceleration, the 2 g of RMS vibrational acceleration as well as up to 40 g of peak accelerations at touch down and opening of the parachute. This is of special concern for the design of the MAIUS-B payload, since it is planned to be reused in a second flight during the MAIUS-3 mission. During the reentry phase the payloads hull temperature rises up to 200 °C on the outside of the hull. This temperature poses strict requirements for the inter-module wiring inside the payload. Another environmental factor inside the payload is the rotation rate of the rocket. The rocket is equipped with a yoyo-system for the rotational stabilization during microgravity time, housed in the motor adapter, but the peak rotation rate 3.4 Hz during boost-phase still pose a threat for the payload. The motor adapter also houses a pneumatic separation system for the payload. The maximum possible payload mass of the rocket is usually limited by the salvage system, but a payload mass above the specified 400 kg will always come at the cost of microgravity time or respectively apogee height. The mass of nosecone, motor adapter and service module has to be counted as payload mass. Graphs about expected rotation rates and accelerations during reentry-phase can be found in appendix A.3 and appendix A.2. To rule out the influence of pressure gradients during the flight the payload on the MAIUS sounding rocket missions is pressurized. More detailed descriptions of the pressurization system and solutions to the various environmental challenges can be found in chapter 3 and in [23].

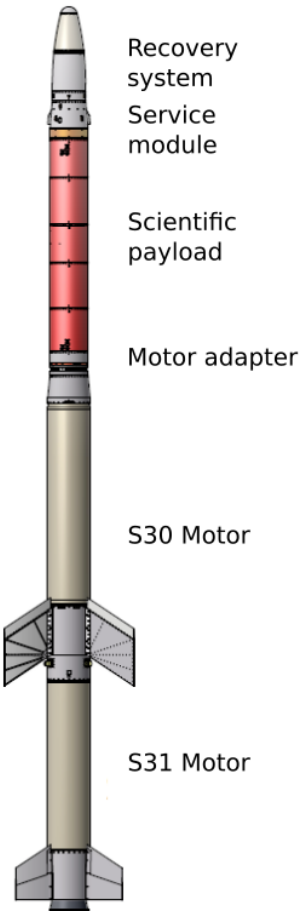

Figure 2.1: VSB-30 rocket in configuration for the MAIUS-1 mission. Overview picture taken unchanged from from [79]

2.2 The MAIUS-1 sounding rocket mission

The MAIUS-1 sounding rocket mission was launched on the 23th of January 2017 on a VSB-30 sounding rocket from the Esrange Space Center in Kiruna (Sweden). Its main goal was to demonstrate and test methods required for atom interferometry in space. Technical details regarding the the MAIUS-1 mission are well documented in [79]. Among many other experiments the production, transport and release of ^{87}Rb Bose-Einstein-Condensates (BEC) and the reproducibility of this process in space was tested and could be compared to theoretical simulations and to ground performance, deliv-

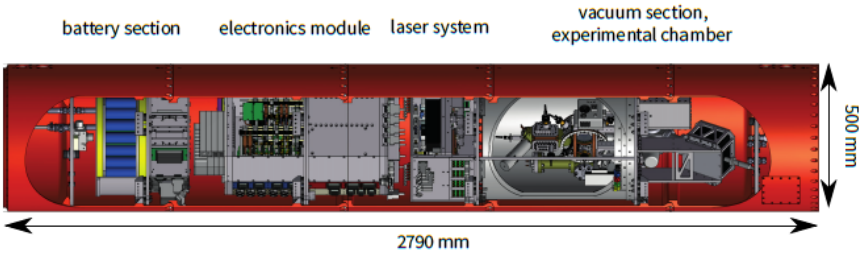

Figure 2.2: CAD-drawing of the MAIUS-1 scientific payload. The shown modules from bottom (left side) to top are: Battery module, electronic module, laser system, physics package. Picture taken unchanged from [65].

ering vital data for future missions. Besides that, techniques like the Delta Kick Collimation (DKC) were tested in space. Other experiments executed during the 6 min of microgravity time included the demonstration of an adiabatic rapid passage into an non magnetic state and the Bragg beam-splitter. Furthermore the mission demonstrated the general feasibility of transferring a ground based experiment to the space environment and showed the fitness of atom-chip based Magneto-Optical Trap's for space applications [10]. In order to build an experimental apparatus fit for the sounding rocket, based on the ground test bed and the drop tower capsules, especially the vacuum system and the laser system required modifications to harden them against the vibrational accelerations of the rockets boost phase and the rockets rotation. Besides that, the system had to be downsized to a cylindrical form of only 50 cm in diameter to fit in the rockets payload section. Due to this area restriction an elongated form was the obvious choice. The final configuration consisted of stackable modules described in this section and reached an overall height of 279 cm and a total mass of 275 kg for the scientific payload only. An overview of this modular payload structure is given in figure 2.2. The modules (from top to bottom) were:

1. (Service module) [2]
2. The physics package
3. The laser system
4. The electonics module
5. The battery module

The modules were mounted on shock mounts described in [23] to absorb some of the shock- and vibrational accelerations. The operation in space made it necessary to implement heat-sinks to absorb the heat produced by the electronic system. The heat-sinks are made from aluminum 7075 cooled by water. A detailed description of the similar heat-sink system of the MAIUS-B experiment can be found in [23]. The requirement of this heat-sinks is one factor that leads to a substantially higher mass for the MAIUS experiments compared to the QUANTUS capsules. The following sections will give an overview over setup and functions of this modules. Since the MAIUS-B system that is the focus of this thesis is based on the MAIUS-A system the following sections will provide the necessary information to understand certain MAIUS-B design decisions but will not go into a detailed description. A detailed description will be provided for the MAIUS-B System in sections 3 and 5.

[2] The service module is outside the pressurized section on the payload and thus not shown in the picture.

2.2.1 The MAIUS-A physics package

The physics package is based on the design of the QUANTUS-2 capsule that is described in detail in [33]. This setup already used the atom chip technology for the Magneto-Optical Trap (MOT) that is discussed in the section 3.1.1. The atom chip technology is a key component in downsizing the MOT setup so far as to fit into a drop tower capsule or a sounding rocket. It is also one of the fastest ways to create a BEC, which is of major importance considering the short microgravity time available during a drop tower launch [33]. The experimental chambers vacuum is created using an ion-getter pump and a titanium-sublimation pump. This setup reaches a residual pressure of 10^{-11} mbar [79]. The ion-getter pump is run continuously while the titan sublimation pump is activated in intervals. The MOT is loaded using an atomic beam generated in an additional $2D^+$ MOT system, that is described in section 3.2.2. The atomic source is an Rb-oven containing ^{87}Rb and ^{85}Rb in the natural isotope ratio. To reduce magnetic disturbances the physics package is shielded with three layers of mu-metal. A detailed description of the science-chamber can be found in [40]. The physics package includes a Charge-Coupled Device (CCD) camera of type PCO 1400 [62] for detection and a small electronic stack for operating the ion-getter pump and the UHV-pressure sensor. The separate stack of vacuum electronic is necessary to allow the continuous operation of the vacuum system while the module is in transit and to ensure high voltage safety.

2.2.2 The MAIUS-A laser system

The development of the MAIUS-A laser system is the combined work of multiple project partners. It is a Distributed Feedback (DFB), Master Oscillator Power Amplifier (MOPA) design especially developed for compact applications and mechanical insensitivity [75]. For the laser module these miniaturized lasers have been combined with ZERODUR-based micro-benches. These lasers are able to operate over a wide temperature range without suffering significantly from thermal expansion. A total of 8 lasers (2 reserve, 2 technology demonstration, 4 experiment) are used in the laser module. One of them is not used with an amplifier. This laser is used as a reference laser and is stabilized to the D_2-transition of ^{85}Rb. The laser system provides an optical output power of 70 mW for the 2D-MOT, 50 mW for the the 3D-cooling system and 25 mW for the interferometer beams. The lasers are switched by Acousto-Optic Modulator (AOM)s and mechanical shutters on the ZERODUR benches [40]. The light is transferred to the physics package by single-mode polarization maintaining fibers.

2.2.3 The MAIUS-A Service module, recovery-system and ARCS-System

The service module provides bidirectional communication between the ground team and the scientific payload during the flight. This radio telemetry is limited to 5 Mbit/s from the scientific payload to the ground-station at a carrier frequency of 2310.5 MHz and 38,4 kBit/sec and is shared with the service module. Telecommands from ground station to the physics package can be uploaded at 449.95 MHz. The communication with the payload could not be guaranteed during the rocket flight. The frequencies used in the service module restrict the available operating frequencies in the electronic system. A frequency in use for telemetry cannot be used in the electronic system to guarantee interference free communication with the payload. The available data rate sets hard limits for the monitoring capability of the payload, especially for the cameras of the detection system.

Another task of the service module is to monitor flight performance parameters like position, acceleration, rotation rate and altitude. The service module also provides power to the battery module and supply triggers for stages of the flight, such as:

- Lift-off (LO)
- Start of experiment (SOE)
- Start of data storage (SDS)

The service module interfaces with the scientific payload via a RS422 UART and can provide a millisecond precision timestamp. Part of the service module is the Attitude and Rate Control System (ARCS-System). This subunit controls the orientation of the payload during the time in microgravity using a cold-gas thruster system. The recovery-system is placed on top of the service module and provides the parachute for the landing of the scientific payload, as well as a radio beacon to locate the payload after landing [81]. The MAIUS-1 service module is planned to be reused for the MAIUS-2/3 missions.

2.2.4 The MAIUS-A electronic and battery module

This section will give a brief overview of the electronic system of the MAIUS-A experiment. The focus will be on components that differ from the setup used in the MAIUS-B experiment. All other components will be discussed in detail in chapter 5. It will discuss functional groups that caused difficulties during the MAIUS-1 campaign in more detail.
The electronic system consist of two electronic modules: The battery module and the electronic module. These modules have the following tasks:

- autonomous control of the experiment
- supply of currents for:
  - DFB-master lasers
  - Optical power amplifiers
  - Atom-chip structures
  - MOT-coils
  - Thermo electric coolers
- frequency stabilization for reference lasers
- provide RF-signals for evaporation
- monitoring of currents
- monitoring of temperature
- capturing of analog inputs from photodiodes
- supply voltage for the physics package and the electronics

The two electronic modules (electronic-module and battery module) are mounted separately within the payload. This configuration is different from the MAIUS-B configuration discussed in 5.

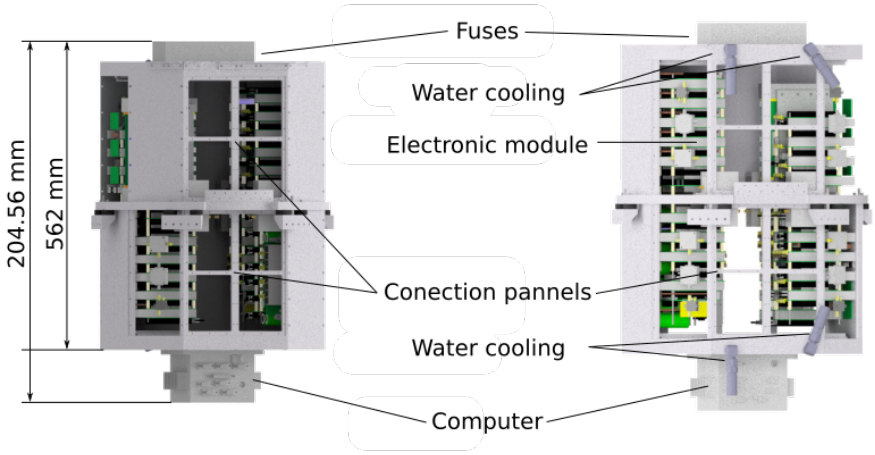

Figure 2.3: CAD-drawing of the MAIUS-1 electronic module. The hull is partially removed in the drawing.

The MAIUS-A electronics module

The electronics module also houses the payloads main computer, which is an off-the-shelf component of type RTD CMA34CRQ2100HR [72]. A similar onboard computer with an additional USB module installed in the same case is used for the MAIUS-B apparatus. Further information can be found in chapter 5. Core components of the electronic system are electronic cards specifically developed for the QUANTUS/MAIUS experimental family by Dr. Thijs Wendrich [84]. This cards are developed under his own TBus-standard. That means that all the cards come in a common size of 100 mm $\times$ 100 mm. The cards are stackable and communicate using their own bus-system. This technology is widely FPGA-based. The TBus standard will be discussed further in chapter 5. Stacks of up to 10 of these cards are housed in the electronic modules and handle most of the control tasks. Besides the TBus-electronics some non-TBus electronic components were designed especially for the MAIUS-A apparatus.
The electronics module can be separated into two sub-modules located on the different sides of the heat-sink. The electronic module contains extra batteries for the chip current driver to ensure galvanic separation of the atom chip from the rest of the payload. Besides the main computer and fuses it also contains the TBus stacks mentioned above. It also houses special atom chip and coil current drivers developed by Dr. Manuel Popp [65]. This current drivers have been specifically developed for atom-chip apparatuses. Since the cold atomic ensemble is very sensitive to magnetic fields this current drivers have to provide a very low noise output current with very short pulse times. These current drivers have been updated for MAIUS-B and will be discussed in detail in chapter 5. Between the chip current drivers and the atom chip a special atom-chip protection electronic is installed, that prevents the flow of destructive currents in the atom chip structures. The experimental sequence is controlled by the main computer and the individual steps are managed by the firmware of the electronics. The communication within the payload is Ethernet-based.
A more detailed description of the electronic components used in the electronic module and an introduction to the firmware system and the experimental control is provided in chapter 5. A overview of the electronic module is illustrated in figure 2.3.

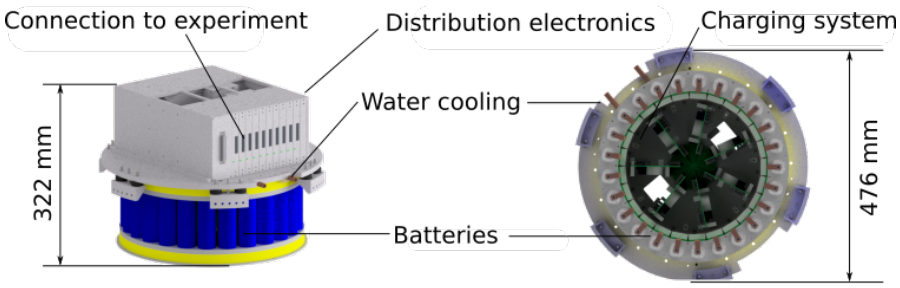

Figure 2.4: CAD-drawing of the MAIUS-1 battery module. LHS: side view, RHS: Bottom view. The bottom housing is not shown.

The MAIUS-A battery module

The battery-module consists of two sides separated by the module heat-sink. The lower side contains 25 battery cells of the type: Headway 38120SE with a nominal voltage of 3.3 V and a capacity 10 Ah. Combinations of parallel and serial arrangement of these cells lead to a variety of supply voltages available in the payload. The available supply voltages are: 3.3 V, ± 6.6 V, ± 14 V and ± 20 V[3]. The batteries are a situated in a ring and connected to a mainboard containing the main fuses at 30 A, monitoring- and charging-electronics, in the bottom of the module. The monitoring contains the temperature of the module, output currents and voltages of the battery packs. For balanced charging commercial overcharge protection elements are mounted on the inside of the battery ring. These protection elements are of type: LiFePo4 LiNANO 2,1A [44] and can direct the charging current of a full battery in a pack through three ceramic 1 Ohm resistors when the cell is full but the pack has not reached its nominal voltage. On the topside of the battery-module heat-sink a distribution module is located that provides switchable outputs for the payload. Accidents with the battery module before the MAIUS-1 mission indicated that the monitoring inside the battery module needs to be extended.
An overview picture of the battery-module is shown in figure 2.4.

2.2.5 The MAIUS-A flight and results

The MAIUS-1 sounding rocket mission started from the Swedish Space Corporation (SSC) launch facility Esrange in Sweden. During the flight numerous experiments with ultra cold atoms including the Bose-Einstein condensation of rubidium and the atom interferometry of ^{87}Rb was performed for the first time in space. The preparation of an atomic ensemble in a MOT started directly after the launch and showed the feasibility of such a technique during the rough launch conditions.
In the six minutes of microgravity time above the Kármán-Line (100 km) the phase transition was investigated, followed by state preparation, beam-splitter, magnetic lensing and the interferometry itself right before reentry. 30 seconds before lift off the experimental phase started with the focus on the influence of launch conditions on atom cooling and trapping in a Magneto-Optical Trap (MOT) and on the expansion time of the atomic cloud After the burning phase of the rocket and the separation from booster and nose cone, the rotation control was executed, starting with the Yo-Yo dispersion

[3]The mentioned voltages are only the nominal voltages of the cells times the number of cells in the corresponding pack. The true voltages are depending on the charging state of the battery. A charging curve of this battery type can be found in appendix figure A.4. Furthermore the available voltage at a device in the payload can be lower due to Ohmic losses in the supply lines.

and followed by cold gas stabilization like mentioned in section 2.1. These measures reduced the residual rotation to 5 mrad/s. The interferometry axes was the aligned parallel to the direction of gravity. After this alignment experiments regarding the phase transition were executed. After the payload reached the apogee of 243 km experiments regarding the atom interferometry were executed.
After the characterization of the phase transition the transportation and shaping of the BEC on the atom chip was investigated, before the measurements regarding the interferometry started. This measurements are discussed in detail in [10] and [40].
During the flight the total number of atoms was higher compared to ground operation. This also resulted in a lower condensate fraction which can be explained by a higher initial number of atoms in the magnetic trap due to a better spacial overlap of the different cooling steps [10]. Some more technical results and lessons learned from the MAIUS-A campaign with impact on the design of MAIUS-B are discussed in chapter 5.
The payload was salvaged three days after reentry and touch down due to weather conditions. These three days gave rise to a further study of the toughness of the payload. The payload was functional after the three days in -34 °C with only minor damage to the cooling system. The payload should have shut down before touchdown to avoid damage caused by the touch down shock. Due to a system failure the payload collected data until 45 min after touchdown when the batteries were empty.
The experimental results of the MAIUS-1 mission are discussed in detail in: [10] and [40].

2.3 The MAIUS-2 and 3 sounding rocket missions

The MAIUS-2 and MAIUS-3 sounding rocket missions are the follow up missions of the MAIUS-1 sounding rocket mission. Both missions will use the MAIUS-B apparatus to carry out various experiments central to matter-wave interferometry, building on the achievements of the MAIUS-1 mission.
The scientific goals of the MAIUS-2 mission, defined in the grant proposal, are:

- Demonstration of a potassium BEC in space.
- Measurements of the delta kick collimation with rubidium atoms, to minimize the expansion rate of 500 pK or less.
- The sequential interferometry of potassium and rubidium.

The second launch of the MAIUS-B apparatus, the MAIUS-3 mission, will have the following mission goals:

- Simultaneous generation and manipulation of quantum degenerate ensembles (rubidium and potassium) in space.
- Simultaneous atom interferometry with potassium and rubidium BECs.

Both missions will launch from the Esrange Space Center in Kiruna Sweden on a VSB-30 Rocket, like their predecessor. The MAIUS-B apparatus expands the functionality of the MAIUS-A apparatus by a second atomic species. As the second species potassium is chosen for various reasons. The mass difference of 46.37 amu between rubidium and potassium makes potassium a good candidate as a second test mass for tests of the equivalence principle. Furthermore the wavelength of potassium's D2-transition with 767 nm is within the operating range of most of the optics used for rubidium at 780 nm. Especially ^{41}K can be overlapped with rubidium due to the intra-atomic scattering

length [40]. Using potassium as a second species the MAIUS-2 mission is planned to show, among other experiments, sequential atom interferometry with potassium and rubidium. The data collected in the MAIUS-2 mission will enable the possibility for the demonstration of a parallel interferometer with the MAIUS-3 mission. The simultaneous creation of the condensates is realized by the sympathetic cooling technique, that is extensively described for the MAIUS-B experiment in [64].
The potassium is cooled by interacting with the rubidium ensemble that is cooled, below the Doppler limit, in the same way like in the MAIUS-A apparatus but with a microwave driven evaporation. This technique will be discussed further in the chapter 3. The microwave electronic system specifically developed for the purpose of evaporating two atomic species will be a focus of this thesis and will be discussed in chapter 5. Measurements regarding the performance of this system can be found in chapter 7. Together the MAIUS-2 and 3 missions will pave the way for a satellite-based implementation of an atom interferometer and provide vital insight into experiments with cold atoms in space that can build the foundation for an International Space Station (ISS) based mission.
Fitting the laser system and support electronic for a second atomic species in a vessel of almost the same size and mass as the MAIUS-A apparatus poses some challenges. Especially the mass limitation of 320 kg for the scientific payload by the recovery system is critical. It became clear in an early state of the developments of the MAIUS-B apparatus that some conceptional changes became inevitable to create a lighter system. The deployment of 7 different supply voltages like carried out in MAIUS-A is no longer on option for the MAIUS-B apparatus. The 25 battery cells necessary to realize the 7 voltages alone have a total mass of 11.88 kg. For the MAIUS-B apparatus it was decided to use only two supply voltages of +6.6 V and 20 V. This two supply voltages lead to a total of 8 battery cells in the main battery module. Even though this decision lead to a battery module of only 18.1 kg[4], it also leads to the need of several redesigns of electronic components used in the MAIUS-A apparatus. Also the communication system within the payload has been updated to Plastic Optical Fibre (POF), on the one hand to save mass for wiring and on the other hand to avoid ground loops that occur when using cable based transition lines via the shielding. Most of these modifications made on the lessons learned from the first MAIUS mission, will be discussed in detail in the chapters 3 and 5.

[4] Without supply cables and connectors.

CHAPTER 3

The experimental setup of the MAIUS-B experiment

The requirements for the electronic system that is the focus of this thesis stem from the necessary experimental steps for the degeneracy of potassium and rubidium as well as from their realization in the apparatus. A short overview on the setup and the cooling methods is given in the following chapter. A more detailed description of the experimental setup can be found in [64].
The first section of this chapter will provide a short review of the theoretical background of the steps necessary for cooling potassium and rubidium atoms to the point of degeneracy. The second section will focus on the specific implementation in the MAIUS-B experiment.

3.1 Theoretical background

The necessary steps of cooling potassium and rubidium atoms to the point of degeneracy are:

1. Trapping and cooling in a magneto-optical trap,
2. optical molasses,
3. optical pumping and loading in a purely magnetic trap,
4. evaporation by microwave field in the magnetic trap.

After reaching the condensed state the ensembles are state prepared for following experiments.

3.1.1 Trapping and cooling in a magneto-optical trap

In the first step of the BEC creation a combination of magnetic and light fields is used to trap and cool the atomic ensemble. This is done by applying a magneto optical trap. In a magneto optical trap atoms are exposed to circular polarized cooling light from all directions. This light is slightly red shifted to an atomic transition of the target species. This light then excites the alkali atoms that move towards the source of the laser light, due to the Doppler effect. Due to directed absorption and undirected spontaneous reemission of absorbed photons a force in direction of the cooling beam arises. This force in all room directions narrows the thermal velocity distribution of the alkali atoms and thus cools the ensemble. The absolute value of this force is proportional to the scattering rate. The latter can be calculated knowing the detuning of the cooling beams to

the atomic transition, by [82]:

$$R_{sc} = \frac{\Gamma}{2} \cdot \frac{\frac{I}{I_{sat}}}{1 + 4 \cdot (\frac{\Delta}{\Gamma})^2 + (\frac{I}{I_{sat}})}. \tag{3.1}$$

Where Δ is the detuning of the laser light from the resonance, I the laser light intensity, I_{sat} the saturation intensity and Γ the natural line width of the transition. Since the line width of an alkali transitions is 6 MHz and its absolute frequency needs to be the cooling laser frequency in addition to the detuning, applying this technique requires a very precise laser frequency stabilization scheme. The electronics used to drive the laser and stabilize its frequency to the atomic transition are discussed in chapter 5. In the case of rubidium-87 atoms the D_2-Line transition $|5^2S_{1/2}, F = 2\rangle \rightarrow |5^2P_{3/2}, F = 3\rangle$ can be used as transition for a cooling scheme. This transition is almost closed, but due to the non-zero line width of the cooling light a fraction of the atoms can be excited to the $|F' = 2\rangle$-state. These atoms are then lost for the cooling cycle because a significant portion of these atoms decay to the $|5^2S_{1/2}, F = 1\rangle$-state. The transition from the $|5^2S_{1/2}, F = 1\rangle$-state to the excited state is not resonant with the cooling light.
In order to bring this off-resonant atoms back into the cooling process a second laser beam is used. This beam (re-excitation beam) is resonant to the $|5^2S_{1/2}, F = 1\rangle \rightarrow |5^2P_{3/2}, F = 2\rangle$ transition. From this state the transitions to the excited hyperfine states are resonant to the cooling beam and can be repopulated. The same technique can be applied for potassium-41. Since the resulting force from applying laser cooling is only dependent on the atoms velocity there is an additional position dependent force required in order to trap the cooled atoms. The magnetic trapping of neutral atoms depends on the Zeeman-effect. Exposing alkali atoms like potassium and rubidium to an external magnetic field leads to a non-vanishing magnetic moment due to the hyperfine splitting of their m_F-states [82]. This effect can be exploited to create a position dependent force. This force is achieved by applying a magnetic quadrupole field with a field minimum in the overlapping region of the cooling beams. Choosing the right geometry for the external magnetic field, a position dependent trap can be created. This technique is described further in chapter 4.
The theoretical temperature limit of this technique is the Doppler limit. This limit depends on the detuning Δ and the lifetime of the upper cooling state. It is fundamental for the technique of Doppler cooling and it can be calculated by equation 3.2:

$$\tau_{doppler} = \frac{\hbar\Gamma}{4k_B} \cdot (\frac{\Gamma}{2\Delta} + \frac{2\Delta}{\Gamma}) \tag{3.2}$$

[82]. Were Γ is the lifetime of the cooling transition, $\hbar$ the plank constant and k_B the Bolzmann constant. From equation 3.2 it is clear that the lowest possible temperature can be achieved for a detuning of:

$$\Delta = \frac{\Gamma}{2k_B} \tag{3.3}$$

Resulting in a simplified form of 3.2:

$$\tau_{doppler} = \frac{\hbar\Gamma}{2k_B} \tag{3.4}$$

Using equation 3.4 the Doppler limits for rubidium and potassium can be calculated. The theoretical limit for rubidium using the transition $|^2S_{1/2}, F = 2\rangle \rightarrow |^2P_{3/2}, F' = 3\rangle$ is 146 µK [82]. The limit for potassium using the transition $|^2S_{1/2}, F = 2\rangle \rightarrow |^2P_{3/2}, F' = 3\rangle$

is also 146 µK, since the line width of the transitions are equal. However the theoretical Doppler limit is valid only for a pure two level quantum system which is a good approximation for rubidium. But since the cooling transition of potassium-41 is only 10 MHz apart from the $|^2S_{1/2}, F = 2\rangle \rightarrow |^2P_{3/2}, F' = 2\rangle$ transition with a line width of roughly 6 MHz this approximation does not apply.

3.1.2 Optical molasses

The previous section described how to trap and cool atoms towards the fundamental Doppler limit. In the next phase an optical molasses is applied. The quadrupole fields are removed and compensation fields for residual magnetic fields are applied. During the following not position trapped phase laser cooling is applied. This leads to thermalization and expansion of the ensemble. To minimize the expansion while allowing for sufficient thermalization this cooling step needs to have a well-defined timing. The optimal time has been determined experimentally to be 2.1 ms.
The optical molasses is applied for rubidium, the potassium atoms are cooled sympathetically during the thermalization. The fundamental limit for this technique is the photon recoil. The photon recoil is the momentum transferred by a single absorbed photon during the cooling process. In practice the minimum temperature achieved is higher when using an atom chip apparatus, due to stray light from and interaction with the atom chips surface. The fundamental photon recoil limit is given by equation 3.5:

$$\tau_{recoil} = \frac{h^2}{m k_B \lambda^2} \tag{3.5}$$

Where λ is the wavelength of cooling laser used and m is the mass of one atom, h the Planck constant and k_B the Bolzmann constant. For rubidium the recoil limit is 361 nK.

3.1.3 Optical pumping and loading in a purely magnetic trap

After the optical molasses phase the ensemble needs be state transferred into a magnetically trappable state for the purely magnetic trap before the evaporation towards degeneracy can begin. The magnetically trappable states for rubidium 87 and potassium 41 are the $|F = 2, m_f = (1, 2)\rangle$-states. The $|F = 2, m_f = 2\rangle$-state is used in the experiment due to its higher magnetic moment. The atoms are transferred to the desired states using the cooling lasers. Since states with higher magnetic moment experience a higher influence of the quadrupole field and thus a deeper trap, the $|F = 2, m_f = i\rangle$-states are coupled to the $|F = 2, m_f = i + 1\rangle$-states by laser light, while applying a magnetic quantization field along the beam direction. This technique is described in detail in [40]. After the ensemble is state prepared the first purely magnetic trap can be applied. The magnetic trapping of neutral atoms is described in detail in chapter 4. With the atoms trapped in the magnetic trap the final step required to achieve the phase transition is the evaporation.

3.1.4 Microwave evaporation to degeneracy

Once the atomic ensemble is trapped in the magnetic trap, the atoms of high kinetic energies need to be removed, in order to reach the critical temperature at which the phase transition to the BEC-state occurs. This removing of atoms of high kinetic energy can be achieved by coupling in a microwave frequency resonant with the transition between the states of higher kinetic energy and untrapped states. Repeating this process while letting the ensemble rethermalize to equilibrium after every evaporation the overall temperature of the ensemble can be lowered and thus the phase space density can be increased. This technique will be described in more detail in this section. The microwave evaporation signal used in the MAIUS-B experiment is generated by microwave system presented in chapter 6.5 and measurements of the phase transition achieved with this system can be found in chapter 7.
The phase transition to the BEC-phase, occurs at a phase space density of $\rho = 2.6124$ [48]. The phase space density of the ensemble describes the probability to find a particle of with a certain momentum at a given point in space and time, it is given by:

$$\rho = n_0 \cdot \lambda_{db}^3 \tag{3.6}$$

where λ_{db} is the de Brogli wavelength of the atoms and n_0 the gas density. This wavelength λ_{db} is given by:

$$\lambda_{db} = \frac{h}{3mk_BT} \tag{3.7}$$

where m is the mass of the atom and k_B is the Bolzmann constant. One can see that by decreasing the temperature, the phase space density of the ensemble can be increased. The gas density n_0 is given by:

$$n_0 = \frac{N}{2\sqrt{2\pi^3}\sigma_{x,y,z}} \tag{3.8}$$

where $\sigma_{x,y,z}$ is the ensembles size in the index directions. The phase space density for an atomic ensemble at room temperature and pressure is typically in the $\rho \sim 10^{-6}$-regime [48]. In order to achieve the phase transition the phase space density thus, needs to be increased. By removing atoms of high kinetic energy from the ensemble it becomes clear that from equation 3.8 that n_0 falls and thus ρ in equation 3.6 has the tendency to lower. However, by removing atoms of high kinetic energy from the ensemble also the overall temperature T lowers due to thermalization. It becomes clear from equation 3.7 that for sinking T the de Brogli wavelength of the atoms increases. One can see that the phase space density increases with the de Brogli wavelength cubed. Thus an overall increase of the phase space density can be achieved by removing atoms of high kinetic energy from the ensemble by microwave evaporation. The evaporation is achieved by coupling the atoms with high kinetic energies to untrapped states using a microwave frequency. The microwave frequencies of 6.8 GHz and 256 MHz for rubidium and potassium are generated by the microwave evaporation system described in chapter 5.

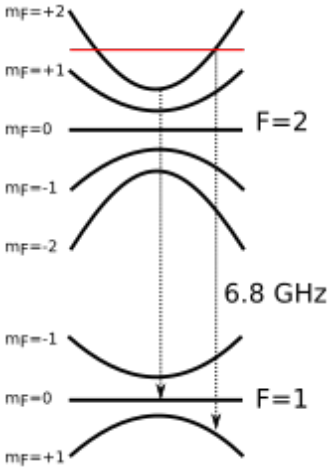

Figure 3.1: Level diagram illustration of rubidium 87 microwave evaporation. The plot shows the hyperfine states of the rubidium 87 $|^2S_{1/2}, F = 1/2\rangle$-states in a magnetic trap and the applied evaporation frequencies.

In the MAIUS-B experiment only direct rubidium evaporation is used and the potassium is cooled sympathetically. The microwave signal of 6.8 GHz is transferred to the atoms via the base U-structure. It couples the trapped $|5^2S_{1/2}, F = 2, m_F = +2\rangle$-state to the untrapped $|5^2S_{1/2}, F = 1, m_F = +1\rangle$-state. During this process atoms can be excited in the $|5^2S_{1/2}, F = 2, m_F = +1\rangle$-state by the same microwave signal du to width of the transition and the evaporation signal. These atoms are then lost for the evaporation and they furthermore showed to heat the potassium atoms in the $m_F = 2$ state due to collisions. These atoms need to be removed by applying a second depumper frequency on the $|5^2S_{1/2}, F = 2, m_F = +1\rangle$ to the $|5^2S_{1/2}, F = 1, m_F = 0\rangle$-state [14]. A schematic picture of the rubidium-87 level diagram with the microwave signals during the evaporation process is illustrated in figure 3.1.

At the beginning of the evaporation process the ensembles temperature is way higher than the critical temperature at which the phase transition occurs. Thus the kinetic energy distribution within the ensemble can be described by the Boltzmann distribution.

$$f(\epsilon) = n_0 \lambda_{db}^3 e^{\frac{-\epsilon}{k_B T}} \tag{3.9}$$

where n_0 is the gas density, k_b the Boltzmann constant, T the temperature, λ the de Brogli wavelength of the ensemble and ϵ the energy of the ensemble. The density of states within the ensemble is given by:

$$g(\epsilon) = \frac{\epsilon^2}{2(\hbar\bar{\omega})^3}. \tag{3.10}$$

Where $\bar{\omega}$ is the mean value of the trap frequencies [73]. From 3.9 and 3.10 the total number of atoms can be calculated from:

$$N = \int_0^\infty g(\epsilon) \cdot f(\epsilon) d\epsilon. \tag{3.11}$$

The total number of atoms occupying states up to an energy threshold ϵ_t can thus be calculated by subtracting the total number of atoms by the same integral from a higher low boundary:

$$\begin{aligned} N_t &= \int_0^\infty g(\epsilon) \cdot f(\epsilon) d\epsilon - \int_{\epsilon_t}^\infty g(\epsilon) \cdot f(\epsilon) d\epsilon \\ &= N - \int_{\epsilon_t}^\infty g(\epsilon) \cdot f(\epsilon) d\epsilon \\ &= N[1 - e^{(\frac{\epsilon_t}{k_B T}) \cdot (1 + \frac{\epsilon_t}{k_B T} + \frac{1}{2} \cdot (\frac{\epsilon_t}{k_B T})^2)}]. \end{aligned} \tag{3.12}$$

Applying a microwave frequency of f leads to a selective lowering of the trap depth, by coupling atoms of higher kinetic energy to untapped states, and the maximum allowed energy for atoms in the trap is given by:

$$\epsilon_t = |m_f| \cdot h(f - f_0) = \eta k_B T. \tag{3.13}$$

where η is the truncation factor and f_0 the resonance frequency at the trap bottom [73]. The remaining atoms in the trap can than rethermalize to a lower overall temperature. In practice the truncation is realized keeping η approximately constant at a high value to minimize the loss of atoms from the trap while ramping down the evaporation frequency exponentially until a value slightly above the trap bottom. Equation 3.12 has been measured in [73] by measuring the number of remaining rubidium atoms in the trap using absorption spectroscopy, for different truncation energies. This measurement with the MAIUS-B experiment can be found in chapter 7.
Once the atomic ensembles are in the condensed state, they need to be prepared for further experiments. The preparation of the BECs and the experimental sequences planned with the MAIUS-B apparatus are documented in [64].

3.1.5 State Preparation

The magnetically trapped atoms in the state $|F = 2, m_f = 2\rangle$ are sensitive to external magnetic disturbances. For the precise measurement of inertial forces necessary for measurements of the universality of the free fall, it is inevitable to reduce this possible disturbances to a minimum. This can be done by transferring the atoms from the $|F = 2, m_f = 2\rangle$-state to the magnetically neutral $|F = 2, m_f = 0\rangle$-state. The direct transition $|F = 2, m_f = 2\rangle \rightarrow |F = 2, m_f = 0\rangle$ is restricted by the selection rules. According to these rules an atomic transition between m_f-states is only possible if $\Delta m_l = 0, \pm 1$. Also the direct transitions $|F = 2, m_f = 2\rangle \rightarrow |F = 2, m_f = 1\rangle$ followed by $|F = 2, m_f = 1\rangle \rightarrow |F = 2, m_f = 0\rangle$ are prohibited by $\Delta l = \pm 1$.
One way of transferring the atoms from the $|F = 2, m_f = 2\rangle$-state to the $|F = 2, m_f = 0\rangle$-state is to perform two Adiabatic Rapid Passage (ARP). Using the two ARP the atoms are gradually transferred from the $|F = 2, m_f = 2\rangle$-state to the $|F = 1, m_f = 1\rangle$-state and than to the $|F = 2, m_f = 0\rangle$-state. The first ARP is applied by coupling the states by radio- or microwave frequencies (depending on the atomic species) while ramping up the quantisation field with the Y-coil. The necessary frequencies for the coupling of the m_f-states of 256 MHz for potassium and 6800 MHz are generated by the microwave evaporation system. This ARP between the first exited state $|e2\rangle = |F = 2, m_f = 2\rangle$ and second excited state $|e1\rangle = |F = 1, m_f = 1\rangle$ can be followed by a similar ARP between $|F = 1, m_f = 1\rangle \rightarrow |F = 2, m_f = 0\rangle$. This state preparation technique has already be shown and described for potassium in [40] and for rubidium in [33].

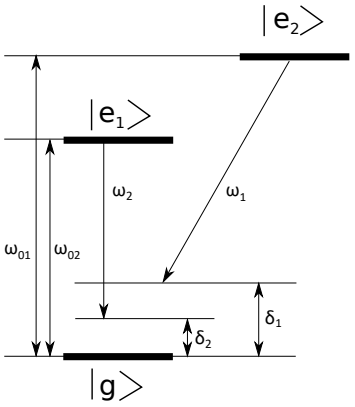

Figure 3.2: Hyperfine splitting of the rubidium 87 ground state. The schema shows the microwave frequencies and detunings relevant for the STIRAP process. In case of rubidium 87 the states relevant for the described STIRAP process are:
$|e_2\rangle = |5^2S_{3/2}, F = 2, m_F = +2\rangle$,
$|e_1\rangle = |5^2S_{3/2}, F = 2, m_F = 0\rangle$,
$|g\rangle = |5^2S_{3/2}, F = 1, m_F = +1\rangle$.

An alternative for the state transfer via ARP is the Stimulated Raman Adiabatic Passage (STIRAP) technique described in [21]. In the case of rubidium 87 the $|e_2\rangle \rightarrow |e_1\rangle$ can be driven directly without violating the selection rules. This can be achieved by coupling the two excited states to the ground state by two fixed frequency microwave signals $\omega_{1,2}$. To achieve the direct transition, the microwave frequencies coupling the excited states to the ground state need to be detuned by $\delta_{1,2} = \omega_{01,02} - \omega_{1,2}$, were $\hbar\omega_{01,02}$ is equal to the energy difference between the ground and the respective exited state. In the case of rubidium 87 this model can be applied with the states $|F = 2, m_f = 1, 2\rangle$ as excited states and $|F = 1, m_f = 1\rangle$ as the ground state. With the coupling applied, ramping the microwave signal amplitude of ω_1 up while decreasing the amplitude of ω_2, the direct transition between the two states can be achieved. The $|F = 2, m_f = 1\rangle \rightarrow |F = 2, m_f = 0\rangle$ can be achieved with the same technique. The selection rules are not violated because the eigenvalues of the triplet system for $\delta = \delta_1 - \delta_2 = 0$ are independent from the ground state. A schema of the levels, microwave frequencies and detunings involved in this process is shown in figure 3.2. Further information about this technique can be found in [21]. Since this technique is planned to be tested with the MAIUS-B apparatus the microwave evaporation system needs to be capable of ramping the output amplitude.

3.2 Implementation

Before starting with the description of the MAIUS-B experimental setup, two important concepts have to be introduced. These concepts are the atom chip and the 2D-MOT.
After the introduction of these concepts this section will provide a general description of the physics package followed by a more detailed description of the vacuum system. In the last part of this chapter the laser system will be described.

3.2.1 The atom chip MOT

The MAIUS-B apparatus uses an atom chip MOT in the science chamber. This means that the creation of the quadrupole fields for the MOT as mentioned in 3.1.1 is realized with a combination of external coils and an atom chip. An atom chip is a setup of multiple planar conduction structures that can be used to form trapping fields for neutral atom, like described in section 4.
The atom chip is inside the vacuum of the science chamber very close to the atomic ensemble. This technique poses several advantages over classical systems, where the magnetic fields have been created with only the external coils. An atom chip MOT device is smaller compared to a classical setup, it is less power consuming due to the

small distance between the atoms and the field generating structures and it allows a faster switching of magnet fields. The smaller distance between the source of the trapping magnetic field and the atomic ensemble allows higher field gradients compared to classical MOT setups. Higher field gradients lead to higher trap frequencies.
Disadvantages of using an atom chip are that a higher complexity of the vacuum system for fitting and connecting the atom chip is required and the volume in which experiments can be executed is limited by the atom chips surface area.
The conducting structures on the atom chip layers are used to produce magnetic fields by leading currents through the different geometries. A current conducted through a straight conductor gives rise to a magnetic field that provides a trap in one dimension like described in chapter 4.
A 3D trapping configuration can be achieved by adding two orthogonal conductors (H-structure) and lead current through them in opposite directions. This configuration can form a trapping quadrupole field. Using this configuration a MOT can be realized. For the pure magnetic trapping of atoms, a configuration with parallel currents in the orthogonal conductors is necessary because the magnetic state of the trapped atoms can flip in the trap minimum. Using the orthogonal wires in parallel a magnetic field is created that has a residual field in its minimum called the trap bottom. The H-structure can be simplified to a (one wire) U-structure for the quadrupole field and a (one wire) Z-structure for the harmonic part. A more detailed explanation of elementary atom chip theory can be found in [65] and [39].
The MAIUS-B atom chip in particular consists of three layers. The mesoscopic structures, the base chip and the science chip. The mesoscopic structure is the bottom layer of the chip and consists of copper wires forming a H- and an U-structure [79]. The copper wires forming the structures are of a diameter of 0.6 mm. Three of them are used for each connection of the H-structure and seven of them are used for the U-structure. They are designed for a maximum current of 10 A.
The middle layer of the atom chip is the base chip. It is glued to the mesoscopic structure by UHV-compatible epoxy (Epotek H77). The base chip is build on a 635 μm thick 48 mm $\times$ 48 mm aluminum nitride substrate. The base chip structures include a middle wire and four perpendicular wires in a distance of 2 mm. The wires are made from a 500 µm wide and 10 µm high, layer of gold. Different Z-structures can be achieved with this configuration. In addition to that two U-structures are used. The base chip gold structures are capable of conducting 6.5 A for a few milliseconds [74]. To avoid damage to the atom chip due to overcurrent coming from a failing current driver, a special atom chip safety PCB is used. This component is described further in chapter 5.
The top layer of the atom chip is the science chip. This layer consists of a 25 mm $\times$ 25 mm aluminum nitrate substrate with 50 μm gold structures. The science chip structures include straight middle wires and a Z-structure. All structures in one layer are electrically connected. This eases down the manufacturing process but gives rise the need of galvanically isolated current drivers for the atom chip. Pictures of the atom chip layers can be found in figure 3.3. For the MAIUS-B experiment the mesoscopic U- and H-structures, the base chip Z-structure and the science chip Z-structure is used.
The contact pattern as well as resistance and inductance values of the MAIUS-B atom chip structures can be found in appendix A.2.
The current drivers providing the atom chip currents are a central part of the experiment. They need to supply high currents while being galvanically isolated, very accurate and very low noise. The current drivers developed for the MAIUS-A mission are discussed in [65]. The updated version used for the MAIUS-B experiment can be found in chapter 5. The current drivers described there are also used for the external coils of

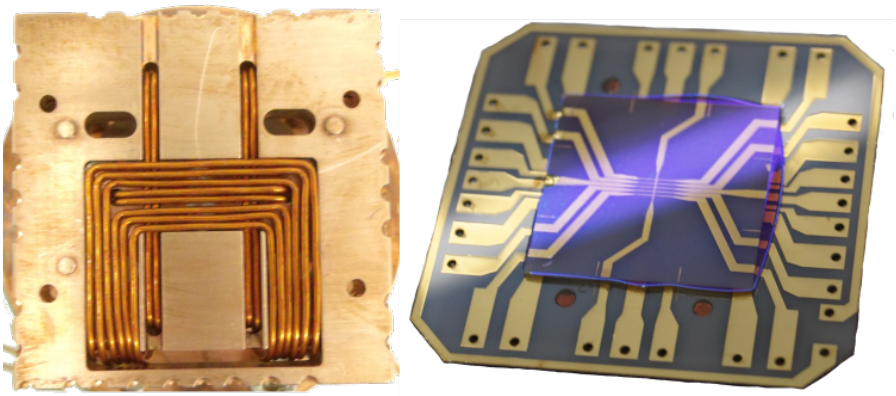

Figure 3.3: Pictures of the MAIUS-B mesoscopic and sience chip layers and their wire topologies. LHS: The mesoscopic structure providing the quadrupole field in the MOT phase of the initial magnetic trap. It is also used for Stern Gerlach experiments. RHS: The science chip is used for the final magnetic trap and the evaporative cooling. It is glued to the base chip that generates the field for the initial magnetic trap, the radio frequency for the evaporation, the adiabatic rapid passage and is used for delta-kick collimation.

the science chamber. They provide two galvanically isolated channels. The power supply system that provides a low noise supply for these current drivers while being galvanically isolated from the main battery is also described in chapter 5. The total power consumption of the chip- and coil structures also poses a challenge regarding the heat load. A more detailed description on the fields used to trap neutral atoms, that can be created by an atom chip and external coils can be found in chapter 4.

3.2.2 The 2D MOT

To increase the loading rate of the MOT inside the science chamber, a $2D^+$-MOT can be applied. In the MAIUS-B apparatus a $2D^+$-MOT is realized in the source chamber. A $2D^+$-MOT is a MOT like described in section 3.1.1 but with cooling light only in 2 dimensions. This is realized by four lateral cooling beams and two longitudinal beams in combination with a magnetic quadrupole field. The quadrupole field needs to have a minimum line in the desired atomic beam direction. To achieve this type of magnetic field the quadrupole coils in the MAIUS-B experiment are situated in a racetrack configuration. The longitudinal beams are called pusher beam (from source- to science chamber) and retarder beam (from science- to source chamber). With the right power distribution between pusher and retarder beam, a beam of cooled alkali atoms from the source chamber into the science chamber that increases the loading rate of the 3D-MOT significantly compared to loading from the background, can be created. The MAIUS-B apparatus reaches loading rates of $2.5 \times 10^8\ s^{-1}$ for potassium-41 and $1.8 \times 10^9\ s^{-1}$ rubidium-87 loading the MOT with beams from the 2D-MOT [8]. The measured loading curves can be found in [64].
To further increase the loading rate, in MAIUS-B the technique of Light-Induced Atomic Desorption (LIAD) is used. Alkali atoms are desorbed from the chamber walls by shining in UV-Light during the MOT phase. By applying LIAD the concentration of relevant alkali atoms in the background gas rises and thus more atoms can be captured directly from the background [38].

3.2.3 The physics package

In the core of the physics package all experiments are carried out in an ultra-high vacuum system. The physics package is separated by the heat-sink into an upper and a

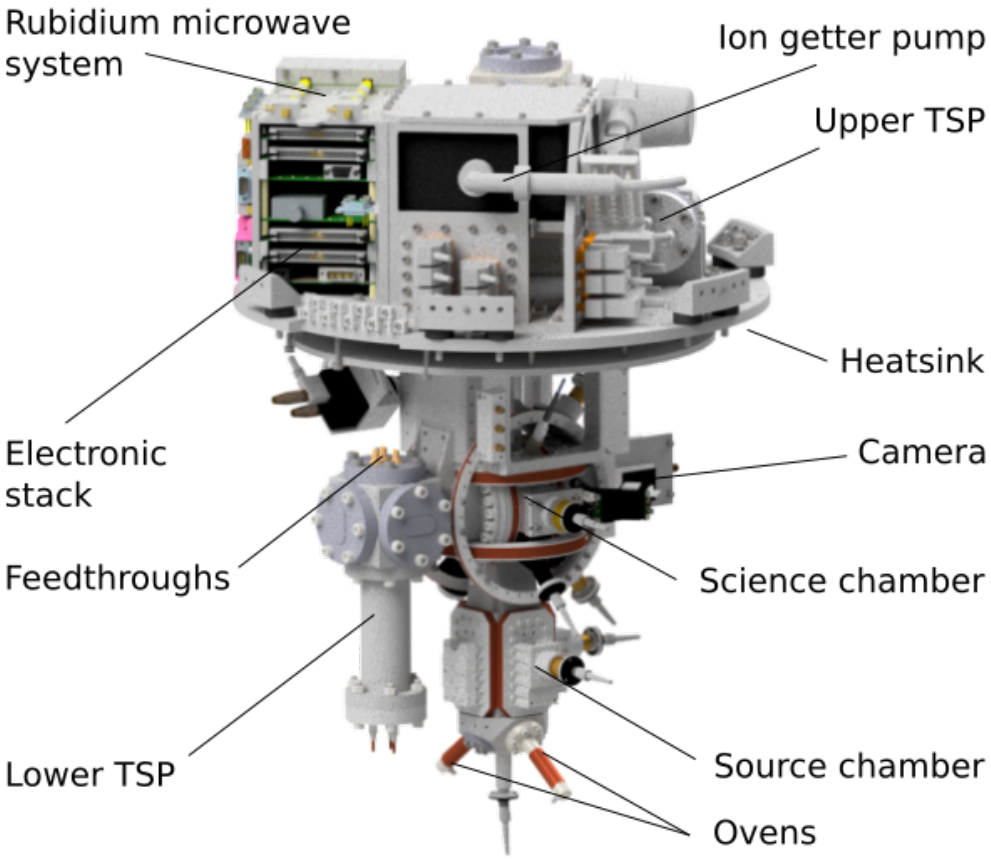

Figure 3.4: CAD drawing of the MAIUS-B physics package. The magnetic shield and the hull is not shown. The extra electronic stack is shown in more detail in B.53. The vacuum system is illustrated separately in 3.5.

lower section. In the lower section, the vacuum system, the beam shaping optics, coils, a Titanium Sublimation Pump (TSP) and the detection systems are situated. In the upper section support electronics, the pressure sensor, the upper TSP and an ion getter pump are located. Separated support electronics in this module are necessary to keep the wires for the microwave evaporation signals short and to have the high voltage vacuum electronics close to the vacuum system for safety reasons. The latter is also important to ensure operation of the vacuum system in a case where the modules of the scientific payload are separated, for example during transit. The vacuum chamber is shielded by three cylindric layers of NiFe against magnetic disturbances. These layers provide a shielding factor of 10000 in lateral and 2000 in longitudinal direction [25]. The detection systems are also included in the magnetic shielding. A CAD drawing of the physics package without the magnetic shielding is shown in figure 3.4. The physics package has a total mass of 71 kg.

3.2.4 Vacuum system

For the execution of experiments with cold degenerate quantum gases an Ultra High Vacuum (UHV) environment is indispensable. Only such an environment allows the creation and observation of Bose Einstein condensates. By lowering the pressure, the collision rate between the cold atomic gases and background gas particles is minimized. The creation of Bose Einstein condensates is possible below a pressure of 10^{-9} mbar [79]. The vacuum system of the MAIUS-B apparatus is a two chamber design of

source and science chamber. The whole structure is made of Ti6A14V titanium that provides a low magnetic susceptibility of $3.3\,e^{-6}$ cgs/g [6]. A low magnetic susceptibility is important to reduce magnetizing effects of the coils on the vacuum chamber, which can disturb the measurement.
The source chamber serves to create the cold atomic beam with a 2D-MOT configuration for a fast loading of the 3D-MOT in the science chamber. Therefore, ovens with glas ampules of 1g rubidum and potassium, respectively, are attached as atomic reservoirs to the source chamber. The glass ampules have been chosen over dispensers due to the successful use of glass ampules in MAIUS-A.
To reach a high atomic flux the partial pressure in the source chamber is raised by heating the potassium oven to 46°C. The cold atomic beam is directed towards the science chamber. The atoms pass a differential pumping stage that enables a difference in background pressure between the chambers of a few orders of magnitude. This is of advantage for further manipulation of the atoms due to reduced collisions with the background gas.
The atoms from the source are than processed in a 2D-MOT and directed towards the science chamber. The $2D^+$-MOT is described in section 3.2.2. The science chamber is held at a pressure in the 10^{-11} mbar regime [64]. In the science chamber the atom chip is located. The science chamber is the place where the experiments are carried out.
To maintain a partial pressure difference between source and science chamber while maintaining a vacuum connection for the beam of cold atoms, the two chambers are connected by a differential pumping stage. The differential pumping stage is a cone tube with an initial diameter of 1.5 mm that widens towards the science chamber. It maintains the pressure difference by its geometry, the small opening towards the high pressure site restricts the travel of undirected particles towards the low pressure side. A graphene insert is placed in the differential pumping stage. Graphene provides a large surface and it reacts with alkali metals, it absorbs part of the atomic beam and lowers the pump cross section further [79].
The UHV pressure inside the chambers is realized using an ion getter pump (Agilent VacIcon Plus 20) and two Titanium Sublimation Pumps. One TSP is of type Vg Sienta ST 22 and one is a self-build model. The ion getter pump needs a high voltage power supply, that has been developed for this mission, it is described in section 5. Before the initialization of the vacuum the chambers are heated over several days to heat out particles from the titanium. The vacuum initialization process and the application of copper pinch-off tubes is described in [79]. The Ion Getter Pump (IGP) is located on top of the physics package and the TSPs are located on different positions that can be seen in figure 3.4. The pressure in the science chamber is measured with a vacuum sensor of type Pfeiffer IKR-270 [63], its support electronics are described in section 5.
To test the fitness of the vacuum system against the vibrational accelerations during the boost phase of the sounding rocket, vibration tests have been performed, the results can be found in appendix A.3.
The optical access to the science chamber is realized by AR-coated indium sealed N-BK7 view ports. The laser access is realized by optical fibers and external telescopes to collimate and adjust the beams in diameter and shape [25]. The detection system includes a camera of type Point Grey Grasshopper 3 [28] for absorption and photodiodes for fluorescence detection. A CAD drawing of the vacuum system is shown in figure 3.5

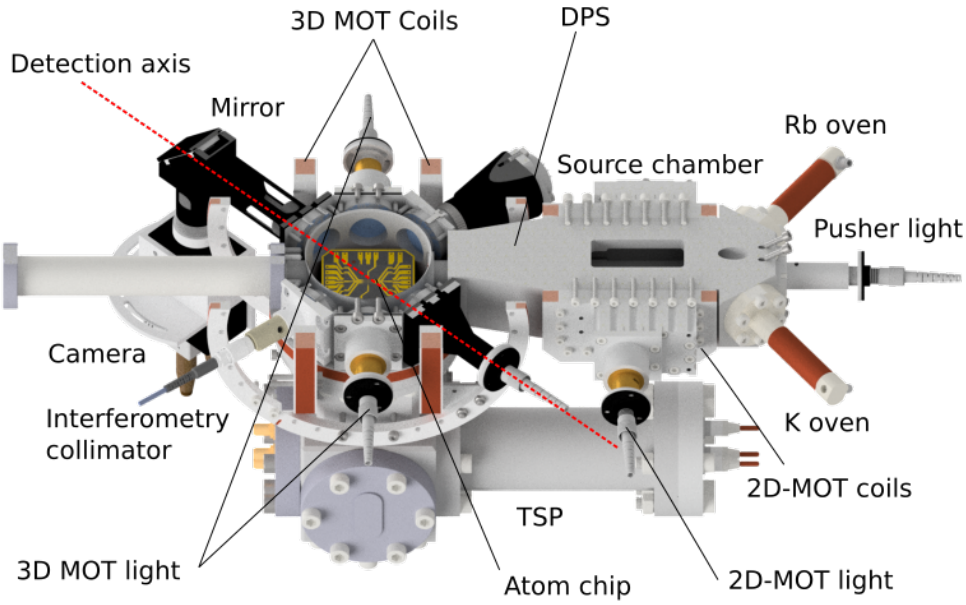

Figure 3.5: CAD drawing of the MAIUS-B Vacuum system. The half section view shows the atom chip inside the experimental chamber. The dashed red line indicates the axis of the absorption detection camera. The axis is tilted to the weak axis of the atom chip by 45°.

3.2.5 Detection system

In the MAIUS-B experiment trapped atoms can be detected by fluorescence or absorption detection. The two detection systems are build in a perpendicular setup and are based on two Charge-Coupled Device (CCD) cameras of type Point Grey Grasshopper 3 (GS3-U3-15S5M) with a 1384×1032 pixel resolution with a pixel size of 6.45 µm [28]. These cameras have a 128 MB internal image buffer that is read out by the main computer by an USB-3 interface. With the image size of 2.79 MB and a typical data rate of 300 MB/s the theoretical maximum number of images per second is 107. The USB-3 connection can also be used to power the camera. However the cameras are also powered over their external connector by the main battery to increase the reliability. More detailed information about the detection system can be found in [64].
The fluorescence detection system is used for state selective detection of atoms. The absorption detection system is used to measure size, form and density of an atomic ensemble. From these measurements multiple key parameters of a cold atomic ensemble can be obtained. For the data analysis of these pictures a specialized software based on [68] is used to extract data from absorbtion images in the MAIUS-B experiment. By comparing two pictures of a BEC taken with the absorption detection system separated by a time t the expansion rate of the BEC can be obtained. Even though the assignment of a thermodynamic temperature is not appropriate for a BEC, it is convenient to use the label "temperature" to describe an atomic ensemble with an average Kinetic energy $\langle E_{kin} \rangle$ as:

$$\langle E_{kin} \rangle = \frac{1}{2} k_B T, \tag{3.14}$$

where k_B is the Bolzmanns constant and T the temperature [48]. The temperature of a BEC can be obtained from the expansion rate by:

$$\sigma = \sigma_0^2 + (\frac{k_B T}{m} t^2), \tag{3.15}$$

were σ_0 is the initial size of the atomic cloud, σ the size after a free evolution time t. This measurement technique is called time of flight measurement. This technique can also be used to measure a heating rate, by comparing two time of flight measurements, were one of the measurements was exposed to a disturbance. This technique was applied for some of the measurements shown in chapter 7.

3.2.6 The MAIUS-B laser system

This section will provide a short overview of the MAIUS-B flight laser system, to explain some design criteria relevant for the description of the laser-electronic module in chapter 5 and the laser current driver in section 5.9. Information on the ground laser system can be found in [64]. The flight laser system was build by the Humboldt Universität Berlin, it has a total mass of 53 kg. A more detailed description of the flight laser system can be found in [25].
The laser module provides the laser light for the experiments. Seven special micro-integrated External Cavity Diode Laser (ECDL) in a Master Oscillator Power Amplifier (MOPA) configuration are providing 350 mW of optical power with a narrow line width of 730 kHz[1] [27]. The lasers are custom build for the MAIUS missions by the Ferdinand Braun Institut (FBH). They are build in a micro-bench setup with the light distribution components on a special ZERODUR-based bench. One additional External Cavity Diode Laser Master Oscillator Power Amplifier laser with a wavelength of 1064 nm is used for the dipole trap. In addition to this total of eight lasers, two Distributed Feedback (DFB) Master Oscillator Power Amplifier lasers are used as frequency reference lasers. One of them providing 780 nm light for the rubidium reference and one providing 767 nm light for the potassium reference. The DFB reference lasers have a tuning coefficient of 1.1 GHz/mA. Their absolute maximum rating for their injection current is 200 mA [36]. The MOPA lasers have a tuning coefficient of 4 MHz/mA. Their maximum injection current rating is 2 A [35]. Given the typical linewidth of an atomic transition of an alkali atom of 6 MHz, that leads to a hard limit of noise in the laser current drivers. To address such a transition effectively, the current drivers need to have a RMS noise of below 4 µA. To achieve reliable detection the noise should be one tenth of this maximum value leading to an upper limit for this noise of 0.4 µA. These values will discussed further in section 5.9 as design parameters for the laser current drivers.
The rubidium reference laser is stabilized to the $^{85}\mathrm{Rb}|F = 3\rangle \rightarrow |F' = 4\rangle$ transition and the potassium reference laser to the $^{39}\mathrm{K}|F = 3\rangle \rightarrow |F' = 4\rangle$ transition. The stabilization is based on two Modulation Transfer Spectroscopy (MTS) modules in the laser module.
The External Cavity Diode Laser Master Oscillator Power Amplifier lasers are offset locked to the reference lasers. The offset stabilization is realized using small fractions of laser light of each laser, that are directed to the beat module by polarization maintaining fibers. In the flight configuration a new type of lock based on an all digital phase locked loop realized in firmware on the frequency controller will be tested. This technique is described in [61]. The exact stabilization theme and the performance of the

[1] Measured in a self-delayed heterodyne measurement using a 2 km fibre delay line on a 10 µs time scale. The intrinsic line with was measured to be 39,7 kHz using the same delay line. [27]

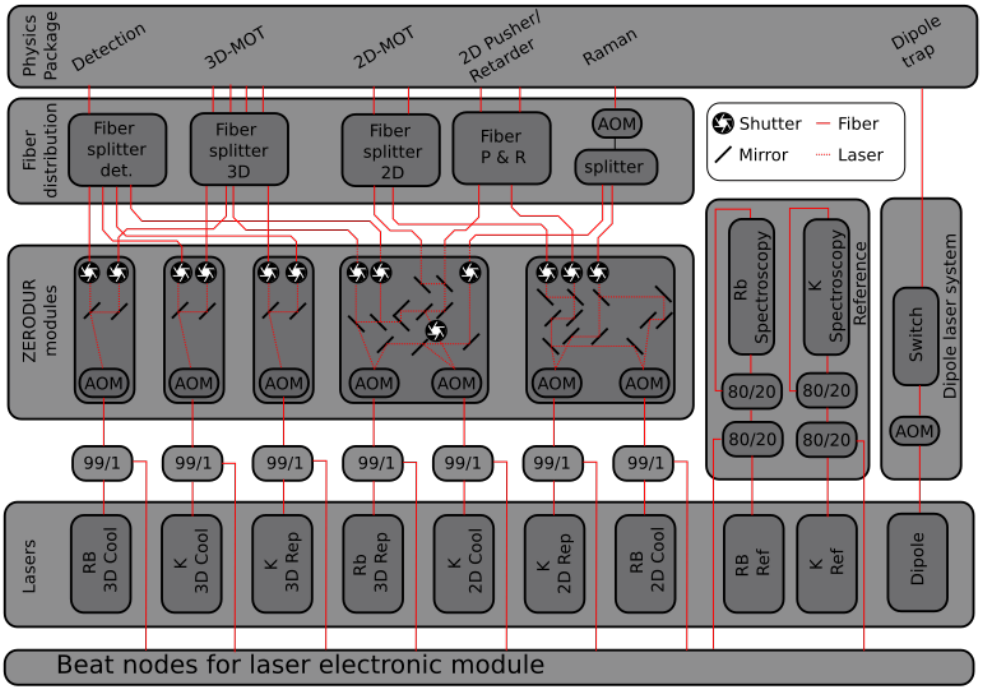

Figure 3.6: Schematic picture of the MAIUS-B laser system. 7 micro-integrated External Cavity Diode Laser (ECDL) in a Master Oscillator Power Amplifier (MOPA) configuration provide the laser light for the physics package (3 on the rubidium frequency and 4 on the potassium frequency). One additional External Cavity Diode Laser Master Oscillator Power Amplifier laser (rightmost laser in the picture) with a wavelength of 1064 nm is used for the dipole trap. Two Distributed Feedback (DFB) Master Oscillator Power Amplifier lasers are used as frequency reference lasers. The AOM and shutter configuration of the laser system can be seen in the schematic. Electrical connections are not shown.

lock is discussed in chapter 5. A schematic picture of the laser system can be found in figure 3.6.
A total of 9 "Fibre-Q" [31] AOMs with a typical frequency shift of up to 200 MHz are used to shift the output frequency of the TA lasers, the tuning is realized with DDS cards located in the laser electronic module. The signals of these DDS cards pass nine 1 W amplifiers of type AMPA-B-34 [59] in the AOM amplifier assemblies to match the need for signal strength of the AOMs in the laser system. The AOM assembly is described in section 5.
16 mechanical shutter of type "Faulhaber Precistep" [26] are used inside the laser system to beam-block unused laser light during an experimental sequence. These shutters are controlled by two shutter cards in the laser electronic module. The light generated in the laser system is directed to the optical ports of the physics package by eleven polarization maintaining fibers.

CHAPTER 4

Trapping of neutral atoms with planar surface structures

The general outline of the necessary techniques for cooling down an atomic ensemble to the point of degeneracy, applied in an experimental sequence performed with the MAIUS-B experiment, has been discussed in section 3. This chapter will provide a deeper inside into the trapping techniques mentioned. This discussion is vital for the characterization of the system and the derivation of limits for the noise performance of the microwave evaporation and current driver systems. The general concept of trapping neutral atoms with surface mounted structures will be reviewed and possible atom loss and heating mechanisms will be introduced. The review of the theoretical background of the heating and loss mechanisms is necessary to understand the design goals for the electronic system. The experimental verification of design goals and limits derived in this section will be part of the measurements chapter 7.

4.1 Trapping of neutral atoms

Trapping of neutral atoms like rubidium and potassium can be achieved by means of their electromagnetic interaction [29]. The magnetic trapping can be realized, even though the atom is neutral, by utilizing the Zeeman effect. In the presence of an external magnetic field the $(2l+1)$ degenerate states belonging to a certain state of angular momentum separate by $\mu_b \cdot B$, were μ_b is the Bohr magneton and B is the absolute value of the magnetic field. This results in a non zero magnetic moment for these states [17]. In a real atom the angular momentum is coupled to the total spin F of nucleus and electron ($F = j + I$) with $j = l + s$ and I being the spin of the nucleus. Considering the spin of electron and nucleus and the spin orbit coupling, every atomic fine state splits into $2F + 1$ hyper-fine states within the presents of an external magnetic field. Each of this states has a magnetic moment of:

$$\mu = g_F \mu_B m_F. \tag{4.1}$$

Where μ is dependent on the hyper-fine state m_F, the Bohr magneton μ_b and the Landrè factor g_F of the atomic hyper-fine state. Depending on the hyper-fine state, the atom experiences a potential in the presence of a magnetic field B, of:

$$V = -\mu \cdot B. \tag{4.2}$$

The coupling of μ and B leads to a motion of the atom with a precession of the magnetic moment with the frequency $\omega_L = \mu_B B/\hbar$ of the magnetic moment, called the

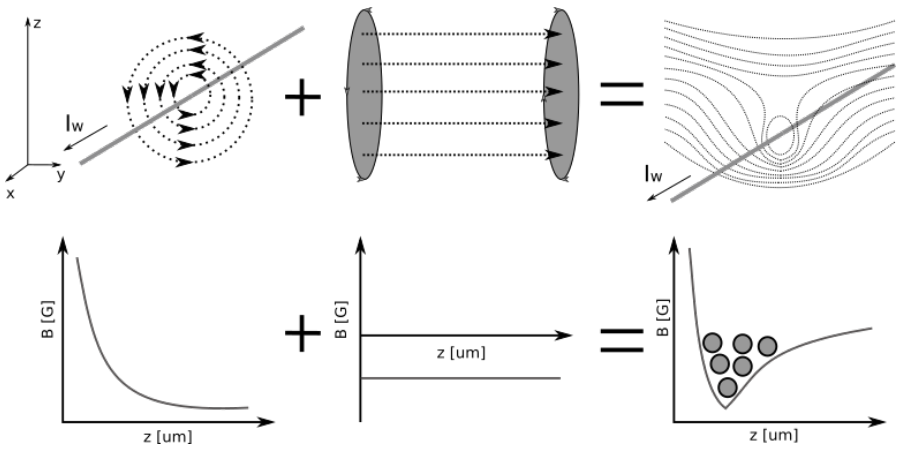

Figure 4.1: Illustration of a simple trap setup consisting of a conducting wire and the magnetic field of a coil setup. The graphs and field lines are to interpret qualitatively.

Lamor precession or Lamor frequency. For the case of $\omega_L >> \omega_{trap}$ an adiabatic approximation can be applied.
Depending on the orientation of μ in the external magnetic field the atom can either be in a strong field seeking state if $V < 0$ or in a weak field seeking state otherwise. Atoms in a weak field seeking state can be trapped in minima of the local magnetic field. In contrast to local maxima that could be used to trap strong field seeking states, the local minima of a magnetic field are not forbidden by the Earnshaw theorem. Thus this discussion will thus focus on traps utilizing weak field seeking states.
The field generated by a conducting wire can be calculated using the Biot Savart law with:

$$\vec{B}(\vec{r}) = \frac{\mu_0}{4\pi} \int_V \vec{j}(\vec{r'}) \times \frac{\vec{r} - \vec{r'}}{\left|\vec{r} - \vec{r'}\right|^3}. \tag{4.3}$$

Where $\vec{j}$ is the current density through the conductor at the position $\vec{r}$ and $\vec{r'}$ is the vector to a given point in the space around the wire. This field can be combined with a magnetic field perpendicular to the conducting wire to form a simple guide for neutral atoms. This guide has a trapping potential along the wire with a local minimum at a distance to the wire of:

$$d = \frac{\mu_0 \cdot I_{wire}}{2\pi \cdot B_{bias}}. \tag{4.4}$$

This bias field can for example be generated using conducting coils in a Helmholz configuration. The potential of such a setup is illustrated in figure 4.1. The described trap setup is called side guide [39] and can trap atoms in two directions. It can also be used as a guide for an atomic beam by adding a magnetic field along the wire direction. Instead of a conducting wire in free space the same trap can be formed using a conducting structure on the surface of an atom chip. This is illustrated in figure 4.2. The trap can be closed by either bending the wire at the end of the trap volumes projection on the atom chip and using a homogeneous bias field, or by simply using an inhomogeneous bias field [39].
In the described wire trap setup the magnetic fields of wire and bias field cancel exactly at the position of the trap minimum. At this point the hyper-fine states of the trapped atom are degenerate and flip into magnetically untapped hyper-fine states are possible. These spin flips lead to trap losses that are called Majorana losses. To

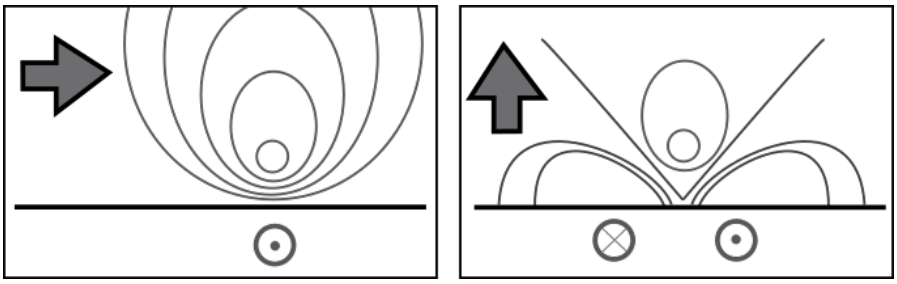

Figure 4.2: Illustration of trapping fields generated by surface mounted structures. LHS: Simple guide generated by a current through a single wire track on the atom chip with an external bias field (thick gray arrow). RHS: Replacement of an external offset field with currents trough chip wire tracks.

avoid these losses an additional offset field can be applied in direction of the wire current. This leads to an increase in field strength at the position of the trap minimum. This trap is then called an Ioffe-Pritchard trap and the offset field B_{ip} is called Ioffe-Pritchard field [39]. Additional types of trap losses will be discussed in more detail in in the following section. By applying an Ioffe-Pritchard field to the trap the potential at the minimum also becomes harmonic. And the magnetic field gradient is given by:

$$\left.\frac{dB}{dr}\right|_{r_0} = \left(\frac{2\pi}{\mu_0} \cdot \frac{(B_b)^2}{I_\omega}\right) = \frac{B_b}{r_0} \tag{4.5}$$

Using a harmonic oscillator approximation the eigenfrequenzy of the potential is given by,

$$\frac{\omega}{2\pi} = \frac{1}{2\pi}\sqrt{\frac{\mu_B g_F m_F}{m}\left(\frac{d^2B}{dr^2}\right)}. \tag{4.6}$$

and can be approximated by,

$$\frac{\omega}{2\pi} \approx \frac{B_b}{r_0}\frac{1}{mB_{ip}} \tag{4.7}$$

were m is the mass of the atom. ω is called the trap frequency of the trap. The trap frequency is a characteristic value of a trap [39].
The MAIUS-B atom chips scientific layer has several Z-type and a H-type structures to form different type of traps. The atoms-chips structure and connection pattern is shown in appendix A.2. The surface structures shown in figure there are not galvanically isolated and the desired pattern can be addressed simply by applying a voltage between the corresponding connections. While this has the advantage of a simpler manufacturing process and a homogeneous structure depth between different geometries, it also leads to the need for galvanically isolated current drivers. Possible trap types that can be applied with this structure are discussed in [65].

4.2 Losses and heating in atom chip traps

Noise and spurious signals of chip current drivers, power supply and systems that have any kind of electric coupling with the trapped atomic ensemble in general, can lead to different types of negative effects like atom losses and heating of the trap. Heating in the scope of this thesis means the excitation of trapped atoms into higher trap states due to the transfer of kinetic energy. Even though these loss mechanisms are extensively discussed in [39] this section will give a brief summery of the dominating mechanisms.

4.2.1 Loss of atoms from the trap

Spill over the trapping potential

Trapped atoms can be lost from the trap by different mechanisms. During the compression phase of the MOT losses can occur if the temperature of the higher trap states is higher then the residual trap depth of the compression. This "spill over" can happen even though the compression is adiabatic. Since only the atoms in the higher energy states can get lost due to this mechanism it can also be used to evaporate the MOT.
Losses due to spill over the trapping potential can be circumvented by using deep trapping potentials.

Majorana spin flips

Furthermore, Majorana losses can occure if the adiabatic limit described in 4.1 does not hold and Majorana spin flips between trapped and not trapped hyper-fine states inside the trap minimum can occur. Residual Majorana losses can also occure in Ioffe-Pritchard traps with a non zero minimum of the trap potential. The residual loss rate due to Majorana spin flips in such a trap can be estimated by:

$$\begin{aligned}\gamma_{msf} &= \frac{\pi\omega}{2\sqrt{e}} e^{\frac{-\mu_p B_{ip}}{\hbar\omega_{tr}}} \\ &= \frac{\pi\omega_{tr}}{2\sqrt{e}} e^{-\omega_L/2\omega_{tr}}.\end{aligned} \tag{4.8}$$

Where ω_L is the Lamor frequency, ω_{tr} the trap frequency of the trap, e the Euler constant and B_{ip} the magnetic field strength of the Ioffe-Pritchard field. One can see from 4.8 that this loss rate is strongly dependent on the ratio: $-\omega/\omega_L$ so that in the adiabatic case for $\omega_L >> \omega_{tr}$ this loss rate becomes small.
The loss rate due to majorana spin flips for the MAIUS-B values of $\omega_{tr} = 126\,\text{Hz}$ and $\omega_L = 2.24\,\text{MHz}$ can be neglected.

Noise-induced losses

Atom losses from the trap can also be induced by current noise. Current noise in the conductor creating the trapping potential can be caused by thermally excited currents, technical noise of the current driver or supply noise that passes through the current driver. The loss rate from thermally excited currents in the atom chips substrate can be estimated by:

$$\gamma_{th} \approx 75 s^{-1} \frac{(\mu/\mu_B)^2 (T_s/300K)}{\rho/\rho_{cu}} (TrY_{ij} \times 1\mu m) \tag{4.9}$$

[39]. Were ρ is the substrates resistivity, ρ_{cu} is the resistivity for copper, T_s the substrates temperature, μ the magnetic moment, μ_b the Bohr magneton and Y_{ij} the geometric tensor of the field volume ($Y_{ij} = \pi/h$ for a half space over a substrate). One should note that the loss rate for thermally excited currents is independent from the Lamor frequency but dependent on the distance to the chips surface. This dependency can be enlarged and thus the loss rate decreased while maintaining the distance to the chip by using thin layers instead of usual wire tracks on the chip. In case of thin layer conductors the geometric tensor becomes $Y_{ij} = \pi d_l/h^2$ where d_l is the thickness of the thin layer [39].
The loss rate corresponding to technical noise from the current driver or power supply

is dependent on the noise at the Lamor frequency $S_I(\omega_L)$. Knowing this amplitude the corresponding loss rate is given by:

$$\gamma_{tn} \approx \frac{\mu^2}{2\hbar^2}(\frac{\mu_0}{2\pi h})^2 S_I(\omega_L). \tag{4.10}$$

[39]. The loss rate due to current noise in the MAIUS-B experiment will be investigated further in chapter 7.

Losses due to collisions

Additional losses occur due to collisions. These collisions can happen with atoms in the background gas or with other trapped atoms. The loss rate due to collisions with background gas atoms can be calculated by:

$$\gamma_c \approx n_{bg}\bar{v}_{bg}\sigma \tag{4.11}$$

[39]. Where n_{bg} is the number of particles in the background volume, $\bar{v}_{bg}$ their velocity distribution and σ is the cross section of the background gas trap interaction.
Collisions of trapped particles can occur in the form of spin exchange or spin relaxation by an inelastic two body collision. The two body collision processes scale with the density of particles in the trap volume. Furthermore trapped atoms can form a molecule that is not trapped (three-body recombination). The loss rate associated with three-body recombination scales with the density of atoms in the trap cubed.

Losses due to tunneling

Additional losses occur due to the tunneling of trapped atoms close to the surface of the atom chip out of the trap area. The associated loss rate can be estimated by:

$$\gamma_t \approx \omega_t \int_{w_b} \frac{1}{\hbar} e^{-\sqrt{2m(U(z)-E)}} dz \tag{4.12}$$

[39]. Where $U(z)$ is the energy of the trapping barrier, E the energy of the trapped particle and w_b the width of the barrier. This loss rate can be minimized by increasing the thickness of the barrier.

Losses due to stray light interaction

Losses from the trap can also occur due to the interaction with stray light. The associated loss rate is proportional to the intensity of the stray light. These losses can be avoided with a good shielding of the experiment against stray light. In the MAIUS-B experiment losses due to stray light interactions can be neglected due to the three layers of magnetic shielding.

4.3 Heating of trapped atomic ensembles

Atoms trapped in low energy states of the trap can be excited to higher trap states. This effect does not necessarily lead to trap losses, except for atoms that get excited to an energy state above the trapping potential, but it can prevent the creation of a BEC [39].

Possible sources for this heating process are again thermally induced currents in the substrate and noise in the current source. One has to differentiate noise that leads to a position fluctuation of the trap center (amplitude noise) and noise that leads to changes in trap frequency (frequency noise).
In a theoretical one dimensional, harmonic potential amplitude noise at the trap frequency ω_T leads to a displacement of the trap minimum. This displacement is equivalent to a force acting on the atom, that can excite the transition from the ground state to the first excited state with a rate of:

$$\Gamma_{0\to1} = \frac{S_F(\omega)}{4\hbar\omega m} \tag{4.13}$$

[39]. Where $S_F(\omega)$ is the force spectrum caused by fluctuations in the wire currents. The excitation rate leads to an energy transfer of $\Gamma_{0\to1}\hbar\omega$. This energy transfer can be interpreted as a heating rate.
Furthermore frequency noise at twice the trap frequency can lead to fluctuations of the trap frequency that excites the $\Gamma_{0\to2}$ transition [39]. The transition rate induced by this noise is given by:

$$\Gamma_{0\to2} = \frac{1}{4}S_\omega(2\omega_{tr}). \tag{4.14}$$

Where $S_\omega(\omega)$ is the frequency noise spectrum. For frequency noise of $1\omega_{tr}$ the trap width fluctuates with the trap frequency and a trapped atom is not in resonance. A source for frequency noise could be a common mode current noise in bias and trapping current, while a disturbance in only the wire or the bias field coil would lead to amplitude noise.

Heating due to technical current noise

Considering the more realistic case of an atom chip based trap potential with bias field and Ioffe-Pritchard type field, with a current in the chip wire of I_ω with a noise spectrum of $S_I(\omega)$ the transition rate from equation 4.13 for fluctuations of the trap position becomes:

$$\Gamma_{0\to1} \approx 2.7s^{-1} \times (\frac{M}{amu})(\frac{\omega}{2\pi 100kHz})^3 \frac{S_I(\omega)/S_{SN}}{(B_b/G)^2}. \tag{4.15}$$

Where S_{SN} is the associated shot noise limit of the wire current and amu the atomic mass unit. Excitations due to fluctuations of the trap frequency in this case are then given by:

$$\Gamma_{0\to2} \approx 10^{-7}s^{-1} \times \frac{(\omega/2\pi 100kHz)^2}{(I_\omega/A)^2}\frac{S_I(2\omega)}{S_{SN}} \tag{4.16}$$

[39]. In general excitations due to frequency noise can be avoided by using a galvanically isolated supply for bias and trapping field, while the single mode amplitude noise is than unavoidable. The effect of heating due to noise in the chip wire currents will be investigated further in the measurements chapter 7.

Heating due to thermally excited currents

Thermally excited currents in the substrate also can excite the $\Gamma_{0\to1}$ transition, but not the $\Gamma_{0\to2}$ transition since their source is located in the substrate and thus only acting on the trapping current. The associated loss rate is given by:

$$\Gamma_{0\to1} \approx 0.7s^{-1} \times \frac{(\mu/\mu_b)^2(T_s/300K)}{(m/amu)(\omega/2\pi 100kHz)(\rho/\rho_{cu})(h/1\mu m)^3}. \tag{4.17}$$

Where m is the atomic mass in amu, ρ is the substrates resistivity, ρ_{cu} is the resistivity for copper [39].

Heating due to light interaction

Heating of atoms in the trap can occur due to the interaction with light used for the detection and manipulation of the ensemble.
In the MAIUS-B experiment this heating rate can be neglected since beams are blocked by mechanical shutters while they are not directly used in the experiment. A more detailed description of loss and heating mechanisms from magnetic traps can be found in [39].

CHAPTER 5

The electronic system of the MAIUS B experiment

5.1 Overview

The electronic system of the MAIUS-2 mission consist of three major modules, the battery module, the laser electronic module and the electronic module.
The battery module contains the $LiFePO_4$ batteries that power all other modules within the payload.
The laser electronic module delivers currents to the lasers within the laser module, it also provides the control loops for frequency stabilization techniques.
The electronic module contains the support electronics for the physics package. Besides monitoring and control purposes it is responsible for delivering currents to the MOT coils and the atom chip structures. It also contains the payloads main computer and extra batteries. These extra batteries provide voltages for the chip and coil current drivers that are galvanically isolated from the main battery. The extra batteries are described in section 5.5.
Besides the three major modules there is an additional electronic section within the physics packages. It is located close to the experimental chamber since the microwave and vacuum electronics are located in this section. This way the losses of the microwave signals can be minimized, the operation of the vacuum system can continue independently from the other modules during transit and the separation improves the high voltage safety.
The electronic section in the physics package will be discussed in the same section as the electronic module.
The majority of the control electronics are designed in a special standard to ensure maximum compatibility and a common form factor. This standard is described in section 5.2. The electronic modules as well as the physics package are held at atmospheric pressure during the flight of the rocket. The pressurization is necessary to allow for the same experimental environment on the ground and during the flight. Thus all electrical connections between the payload and the ground support electronics are feed-through umbilicals in the rocket hull and through sealing plates at the top and bottom of the scientific payload. The umbilicals, feed-throughs and pressurization techniques are described in [24]. An overview over the entire scientific payload is provided in figure 5.1. During ground operation of the scientific payload the system is connected to a Ground Support Equipment (GSE) unit through the upper and lower umbilical. The lower umbilical contains connections for the charging current to the main battery module. The upper umbilicals contain charging currents for the extra batteries, the TiSub currents and monitoring signals. The connection patterns of umbilicals and feed-throughs can be found in [23]. Besides the electrical connections the payload is,

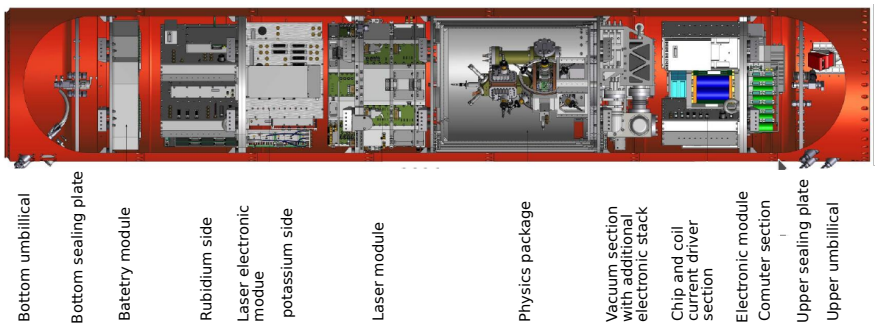

Figure 5.1: CAD drawing of the scientific payload of MAIUS-B. The bottom of the payload is the left side of the picture. The shown modules from bottom to top are the battery module, the laser electronic module, the laser module, the physics package and the electronic module. The upper and the lower sealing plates and the connections to the upper and lower umbilicals are shown left and rightmost in the drawing.

during ground operation, connected to chiller units in ground operation mode. The chillers and water connection are described in detail in [23].
A full electronic circuit diagram of the scientific payload is created using a make script. This make script creates hierarchical circuit diagrams of the whole scientific with ground support. The top layer schematic shows the connections between payload modules and between modules and ground support. On the module layer a schematic of the connections between assemblies inside a module is created. It includes the component level schematics and automatically builds eagle libraries for the hierarchy. A script based connection to the CAD software is planned but not implemented.

5.2 The TBus-standard and basic system infrastructure

The TBus standard is an internal design standard for PCBs specifically created to fulfill the needs of laser based experiments in micro gravity environments. It is optimized for compact and autonomous operated systems like drop tower capsules and sounding rockets. It was originally developed by Dr. Thijs Wendrich for the application in the QUANTUS drop tower missions. Within the project Laser Unter Schwerelosigkeit (LASUS), founded by the Deutsches Zentrum für Luft- und Raumfahrt (DLR), several PCBs with integrated microelectronics for the use in atom optic experiments have been created.
This work paved the way for the electronic system described in this thesis. In the context of this thesis PCBs designed in the TBus standard are called cards. Multiple cards can be mechanically piled to a stack, forming a connection using two board to board connectors, one for analog signals and one for digital signals. The connectors are equal to the PC104 standard but differ in pin assignment and position, making it mechanically incompatible. A stack of TBus cards can be accessed via an interface card. USB, NI-FPGA, Ethernet and Plastic Optical Fibre (POF) are available for the TBus. Additionally the TBus can be connected to the PC104 bus by an adapter board.
For the MAIUS-2 mission a special POF interface card, combined with a 6.6 V and 19.8 V power input, was created. This card is described in more detail in section 5.7.1. Since the MAIUS 2 payload has a great demand for saving mass in the design process it was decided to combine the two cards. Also POF was chosen as the communication interface due to its lighter mass compared with cat-6 Ethernet cables but also due to its isolation property. Parasitic ground loops formed by the shielding of coaxial and Ethernet wires have proven to be a problem in MAIUS 1. For the purpose of using POF within the payload combined Ethernet and POF switches had to be created. The switches and

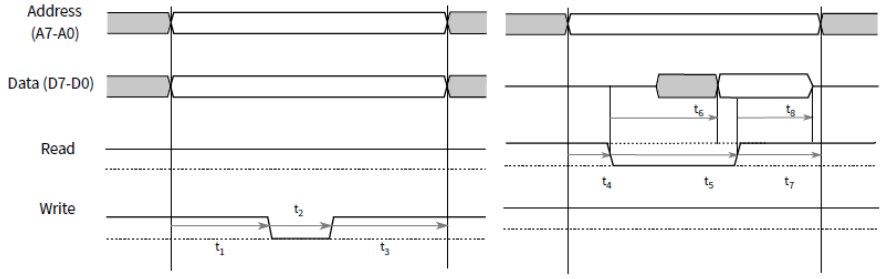

Figure 5.2: LHS: Illustration of a standard TBus write cycle. After the control software requested a write, the interface card provides address and data on the bus connector. After a setup time of t_1 a falling edge on write triggers the write operation. During the time t_3 Write is held low and the card writes its register. After t_2 the data is held valid for a hold time of t_3 to compensate for possible differences in run time on the bus lines. RHS: Standard TBus read operation. After the control software requested a read, the interface card provides the address on the bus connector and releases the data pins. After t_4 a falling edge on read triggers the addressed card to writs the requested data on the data pins. The data must be valid after $t_6 < t_5$ were t_5 is the time of the transmission of a rising edge on read to close the process. The data is held valid for t_8.

the connection to Ethernet based main computer are described in 5.7.1 and 5.6.
The TBus is an 8-bit bus system (8 data lines, 8 address lines, 2 command lines, 13 trigger lines and one clock line). A typical read and write cycle of the TBus is illustrated in figure 5.2. The communication between the stacks uses a 3-byte protocol.
The new generation of the communication protocol, that is also used for the POF communication, has no fixed packet size, can transfer more complex commands and uses run-length compression making it more efficient. The TBus can be clocked externally at 10 MHz or 24 MHz. Every card in a stack is assigned a unique address using a rotary encoder. The 8 address lines theoretically allow for 255 addresses per stack. To create the possibility of addressing multiple registers on more complex boards, the 4 most significant bits of the address byte are used to address a card while the remaining 4 least significant bits are used to address registers on a specific card. This allows theoretically to address 16 cards with 16 registers each per stack.
However to create more complex cards with the need for even more registers it is possible extend the address space of a card using one register as an address- and one as an data-register. This technique is described in section 5.7.1. The timing specifications for TBus read and write cycle can be found in 5.2. From Windows PC's the TBus can be accessed via the TBUS Dynamic Link Library (DLL). In order to specify the address space of a TBus environment two additional files are required. A stack.xml file for every stack specifies the interface type, address and the types of cards in a stack. A card.xml for every card in a stack describes the register addresses of this card.
For the operation of the MAIUS-B experiment a UNIX based control software created by the Zentrum für angewandte Raumfahrttechnologie und Mikrogravitation (ZARM) is used. For the flight configuration the control software was designed by the DLR-SC. A typical implementation of a TBus environment is illustrated in figure 5.3. The transport layer protocol translation between the control software and the POF interface, including the firmware for the switches was designed for the MAIUS 2 mission by the Institute for Microelectronic Systems in Hannover.

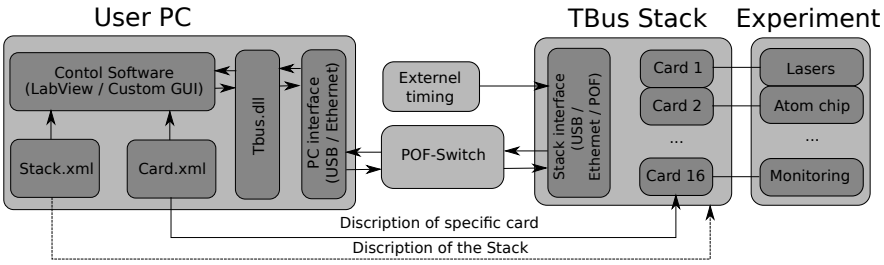

Figure 5.3: Schematic picture of a TBus implementation. The user PC is shown on the left, the Stack.xml and Card.xml files are stored on the user PC and describe the hardware configuration. The TBus.dll translates the register values requested by the control software to actual TBus data words. The interface can be connected directly to a stack (Ethernet or USB) or via a switch (POF/Ethernet/USB). The external timing is optional. The connection between user PC and TBus stack can be through one of the interface types mentioned in this section.

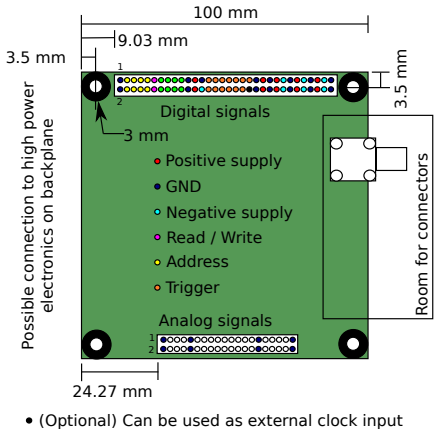

Figure 5.4: Schematic picture of a TBus card layout. The pin functions of the PC104 connectors are shown in colors. The exact pin configuration can be found in the appendix. The colorless pins depend on the specific card

The mechanical design of TBus cards is a 100 mm × 100 mm PCB with the PC104 connectors on the sides. The mechanical design is illustrated in figure 5.4. The exact pin assignments of the PC104 connectors can be found in appendix A.7. The height of the PC104 connectors of 16 mm and the PCB thickness of 1.6 mm lead to a height of 17.6 mm for a cart in a stack. This unit height also limits the number of carts in a stack within the payload since the overall length of the payload is fixed. It also limits the available space on a back plane for power intensive parts.
The TBus was originally designed to supply seven different voltages, see also appendix A.7. However the use of seven different voltages was not practical for the application in the MAIUS-B apparatus, because every voltage corresponds to a heavy $LiFePO_4$ pack. The topic of the available supply voltages will be discussed in chapter 5.5.
However some of the TBus cards had to be updated to work with only the two supply voltages used in the MAIUS-B apparatus. The TBus cards used in the MAIUS-B apparatus and their basic functions are listed in the next section. From the variety of cards shown in this section only the laser current driver cards, the chip and coil current drivers and the microwave card will be explained in detail in sections 5.7.1 and 5.6.

5.3 Specification of TBus cards used in the MAIUS-B experiment

This section will give a brief overview of the specification of TBus cards used in the MAIUS-B experiment. This section is not meant to give a deep technological inside into the cards, it is only supposed to present key features like their general purpose and the number of available channels. The microwave back-end is described in more detail in 6.5. The current driver are discussed in more detail in section 5.9.

- POF and power interface board. This card is a combination of stack power supply

and a POF interface for the TBus. It has a MAX 10 main FPGA to handle the communication. The power input is realized with a Dsub 3W3 connector, the power electronics are mounted on a seperate aluminum board that can be mounted on the backside of the stack. The average power consumption is 1 W.

- The frequency controller board. This board is designed to process signals from laser beats and form control loops with the laser current drivers. The MAIUS-B version of the frequency controller is based on a MAX-10 FPGA. This cards has a total of 8 SMA connectors. One AC coupled for the input of a spectroscopy signal with a 12 bit input ADC with a high sample rate of 40 MHz. Three DC coupled inputs for beat signals up to 1 GHz. One modulation output the enable frequency modulation spectroscopy with an external demodulation mixer and three additional multi purpose inputs. Additionally 4 fast signal outputs with a 14 bit DAC at a sample rate of 25 MHz for current drivers are connected over the Bus. 4 slow outputs with a 14 bit DAC at a sample rate of 100 kHz are also connected over the Bus.
- Master laser current driver. This card controls up to two lasers with a maximum output current of 230 mA per laser. The current setpoint can be selected by control software. A fast current offset can be driven over the bus to form control loops. The maximum current offset over this channel is 32 mA [9].
- TA current driver. This card is a TA variant current driver that can provide laser current for one laser with up to 1.7 A. One SMA connector is used for the current output. One additional SMA input can be used to read a photodiode input, that can be used to form an output power control loop.
- Shutter driver card. This card is designed to operate up to 16 2-coil stepper motors, it can operate on 3.3 V or 6.6 V. The board is based on a MAX 10 FPGA.
- UHV Sensor card. This card is designed to read data from a IKR-270 UHV pressure sensor. One sensor is connected via a SubD-9 connector.
- Ion-getter controller. This card is designed to drive an IGP with 8 kV
- Fan controller. This card drives up to 8 fans. The fans can be connected through 8 separate molex connectors.
- Photodiode input. Reads the signal of up to 25 photodiodes that can be connected by a boxed pin header. This card can be used for monitoring purposes.
- NTC input. Reads the signal of up to 25 NTC sensors.
- DDS card. Output frequencies between 25 MHz and 200 MHz.

5.4 The communication timing and trigger system

The central part of the communication, timing and trigger system of the payload is a combined Ethernet and POF switch, based on a Microsemi SmartFusion2 FPGA [50]. The Smart fusion FPGA was chosen over the usually used MAX 10 FPGA for its higher radiation tolerance. This was necessary since its a critical single point of failure of the experiment due to its relevance for the timing. The combined Ethernet and POF switch consists of a commercial Ethernet switch of type NETGEAR FS108 with 8 100 MBit/s ports and a self build 12 port POF switch, that contains the main FPGA. The two parts

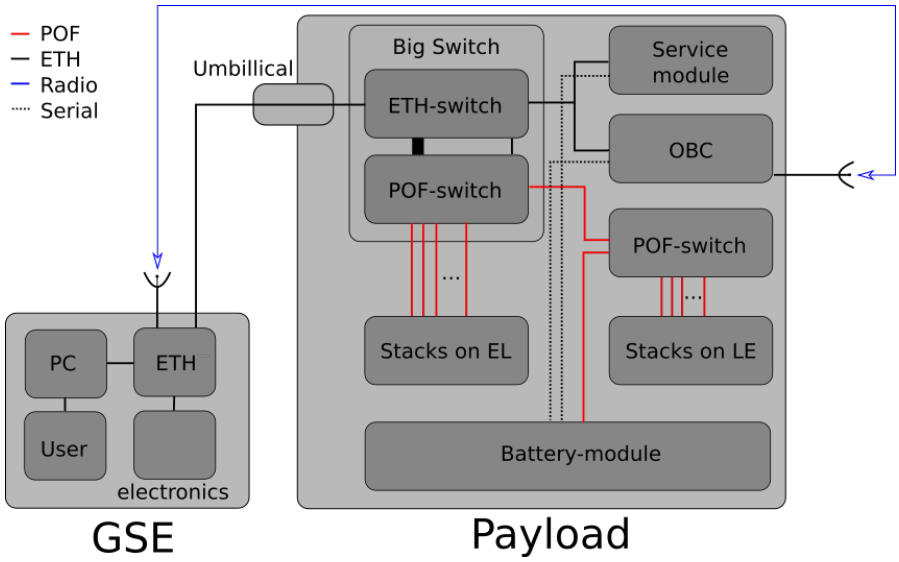

Figure 5.5: Schematic of the payloads network system and connections to ground control and ground support electronics. Solid black lines show ethernet connection, blue lines show radio connections, dashed black lines electrical trigger lines and red lines indicate POF connections. POF connections also include timing and trigger.

are connected by a ribbon cable and housed in the same case. The main switch is housed in the EL section of the payload to be close to the upper umbillical, the service module and the onboard computer. These modules are connected via the Ethernet switch, since these components have not been available in a POF variant. The interface cards of the the EL section are connected via the POF ports and translate the POF protocol to the TBus protocol described in 5.2. One POF connection is used as an up-link to a second POF-only switch in the LE section of the payload. The service module radio connection to the ground control is on ground translated to a Ethernet connection. A schematic picture of the connections is shown in figure 5.5.
The main POF switch contains the central timing. A Abracon AOCJY2-10.00 MHz [3] oven stabilized crystal oscillator is used as the central timing reference. Its signal is processed by a PLL on the switches main FPGA to a frequency of 50 MHz and distributed through the POF system. The switch also provides an output port for this 50 MHz clock via an SMA connector, that is used as a reference for the microwave system.
While the experiments start trigger is handeled by the OBC, the following sequence triggers are handled by the switches FPGA, they are also distributed through the POF system. The latency of the sequence triggers is 400 ns for the connection between the switches. These values a fixed and synchronized for all output ports. Further information on the protocoll used for the POF communication and the protocol translation to TBus are well described in [80].

5.5 The battery module

5.5.1 Design goals of the main battery module

The main battery module developed for the MAIUS-B experiment had to be designed with two major goals besides the requirements dictated by the experiments. It had to drive an electronic system double the size of the one it predecessor was used for and it had to be reduced in mass and size compared to its predecessor due to the overall limitation of the payload.
The module needs to have 24 separately switchable output channels that can provide

10 A for each output voltage.
Based on experience with the MAIUS-A battery module it was required to be able to monitor the voltages of every single battery cell and every battery-pack, as well as the overall current delivered by the module and the current through each output channel. An overcharge protection system for the case of unbalanced charge in a battery pack is needed. The charging system needs to monitor the state of every cell in a pack to allow for reduction of the charging current in case of an unbalanced charging case, to avoid overheating of the overcharge protection circuits. The logic circuits of the battery module need to be supplied by either the service module or the ground support to guarantee operation independent from the battery packs to ensure a full shut down even if the battery firmware fails. The battery module must allow for at least 45 min of experiment time without charging. Furthermore the battery module represents the intended common ground for electronic systems and the ground support. The different grounds of the scientific payload are connected by 1 MOhm resistors.
To allow for a galvanically isolated power supply of the chip and coil current drivers and the microwave system, extra battery packs for these components are necessary. Layout and schematics of both extra batteries are shown in appendix B.1.2.

5.5.2 Implementation of the battery module and the extra batteries

To reduce the module mass it was decided that the module in contrast to its predecessor would only provide two output voltages, 6.6 V and 19.8 V. Leading to a total amount of 8 $LiFePO_4$ batteries.
The electronic part of the battery module consist of five major components:

1. Motherboard that contains the charging electronic and connects all components
2. Overcharge protection system
3. 8 Cell $LiFePO_4$ battery pack
4. Communication plug-in board
5. 24 Plug-in boards containing the output channels.

This components are described in the following sections. The module is mounted on an water and glycol cooled aluminum heat-sink and is encased in an aluminum sheet casing. The motherboard is mounted on the heat-sink and it contains plug-in connectors for the communication board and the output channel boards. The battery pack is also mounted to the heat-sink and connected to the motherboard with two DSUB 2W2 connectors. The connection pattern of these connectors can be found in appendix B.1. The overcharge protection system is mounted on top of the battery pack. Connections between the battery pack and the overcharge protection system are soldered. The overcharge protection system is connected to the motherboard by a ribbon cable. A cooler with fans is mounted on the heat-sink and air guides are milled in the heat-sinks.
The CAD drawings of heat-sink and cooler can be found in appendix B.1 A schematic picture of the connections inside the battery module can be found in figure 5.6. The battery module represents the common grounding point of the whole electronic system. The grounding concept focuses on avoiding parasitic ground loops. Therefor every connection between the grounds of GSE, service module and electronic system is on the motherboard over 1 MΩ resistors. All other signals and supply lines are led through opto- or magnetic couplers to ensure galvanic isolation. One reason for

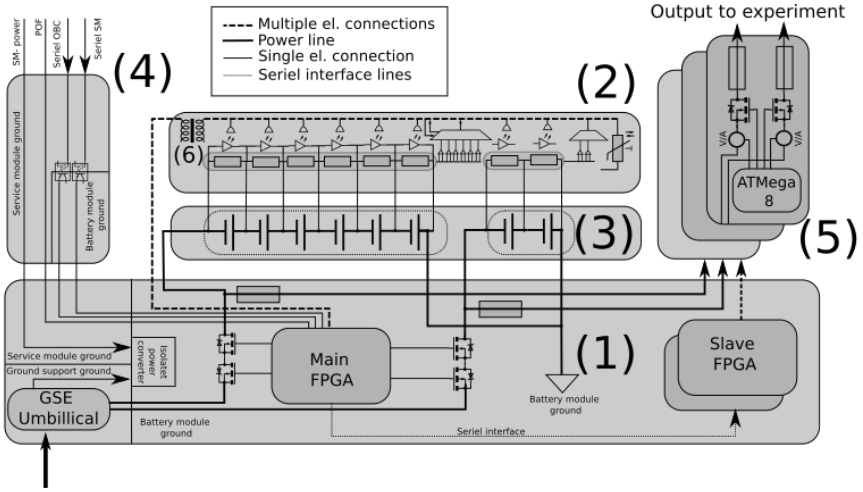

Figure 5.6: Schematic picture of the MAIUS-B battery module. (1) Motherboard, (2) Overcharge protection system, (3) battery pack, (4) communication board, (5) 24 Output channel plug-in boards, (6) Magnetic coupling devices for logic signals and power supply. The System grounds of servive module, ground support and electronic system connect at the shown location. The power supplies from service module and ground support are connected isolating DC/DC converters of type: TEN 5-2411 [83]

choosing Plastic Optical Fibre (POF) for the communication is to avoid ground loops formed by the shielding of Ethernet cables. However parasitic ground loops are still expected to form by the shielding of coaxial cables. The overall grounding concept of the scientific payload is illustrated in appendix B.46.
The MAIUS-B battery module provides 24 output channels each delivering 6.6 V and 19.8 V. Every voltage of every output channel is separately switchable. Output voltage and current are monitored for every output port and for every battery. The module has an overall height of 82 mm and a total mass of 15 kg. A CAD drawing of the module is illustrated in figure 5.7. The maximum power of the battery module is 996 W and it has a capacity of 15 Ah. The results of thermal simulations regarding the battery module can be found in appendix B.1. The extra batteries for the microwave system and the chip and coil current drivers are 2 cell and 6 cell standalone versions of the the main battery.
The six cell extra battery delivers two output ports providing 20 V for the current drivers of the MOT coils. The five 2 cell extra batteries provides 6.6 V with one output channel per battery for the chip current drivers and the microwave system.
The extra batteries are both located in the electronics module, nevertheless they are described in this chapter in section due to their similarity to the main battery and their overall importance for the general grounding concept.
The electronic system also uses two external 28 V power sources, the ground support electronics and a supply from the service module. These external supplies are necessary to guarantee for a clean shutdown and are connected to the main battery module. A schematic picture of the power supply concept inside the scientific payload is shown in appendix B.46. A summary of power consumer and the calculation of possible experiment operation time with the batteries can be found in appendix B.1.

The motherboard and batteries

The motherboard contains the charge control, the connections to the plug-in boards and fuses. The $LiFePO_4$ battery pack is connected to the board via four DSUB 2W2 connectors. The currents from the battery pack are fused at 30 A. The motherboards

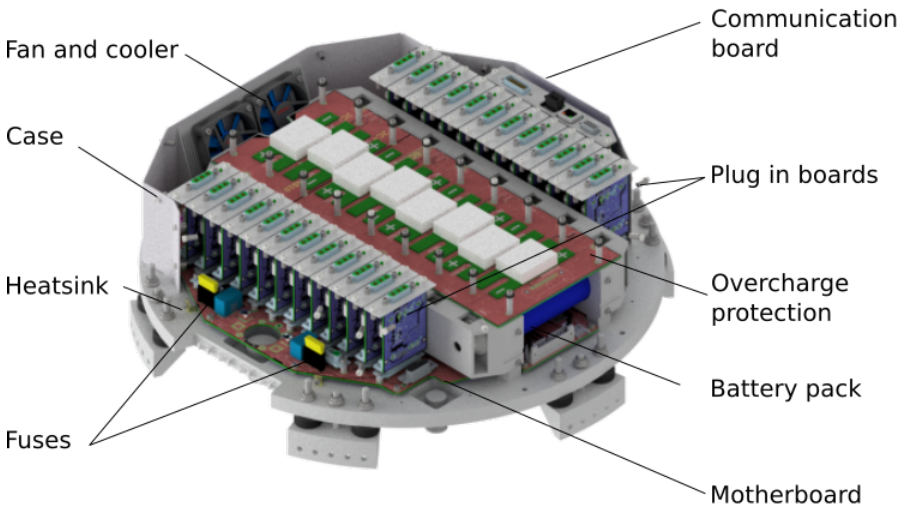

Figure 5.7: CAD model of the MAIUS-B batetry module. The cover is not shown. On the module sides 24 plug-in cards with output channels and the communication board are visible. In the center the overcharge protection system is visible. It is mounted on the battery pack.

main processor is a MAX10 Intel FPGA (10M08DCF256C8G) [37]. It controls the charging system, the communication with the plug-in boards, the main computer and the service module. Two smaller Complex Programmable Logic Devices (CPLD) of type EPM240F100C4 are used as an input/output extension for the main FPGA. The current on the main power lines is measured by two sensors of type LEM CASR-15 [42]. These sensors have a usable range of -51 A to 51 A sufficient to measure the currents on the motherboard. Their signal is converted by an MCP3425 16 bit analog to digital converter [49]. This leads to a Least Significant Bit (LSB) resolution of 12 mA. The motherboards logic circuits can be supplied by the GSE or the service module. Supply of the motherboard by the battery packs is avoided to avoid discharging due to leakage current inside the measurement electronics when the system is not in use. The supply lines are converted and galvanically isolated by two TEN 2411 DC/DC converters [83]. The motherboard represents the common ground of the electronic system. The grounds of the Ground Support Equipment (GSE), the service module and main ground of the apparatus are present on this board and are connected through 1 MΩ resistors. The battery pack consists of 8 $LiFePO_4$ batteries. Connected in a six cell pack and a two cell pack. The batteries used are of type: "15 AH 3,2V 10C Headway 40152SE" [45]. $LiFePO_4$ batteries have been chosen due to their high energy density of 100 Wh/kg. This battery type has a nominal voltage of 3.2 V, a charging end voltage of 3.65 V and a discharge end voltage of 2.5 V. The batteries can deliver five times their capacity constantly and ten times their capacity for peak output.
The $LiFePO_4$ batteries have to be charged in a constant current / constant voltage charging pattern, where they are charged with a constant current up to a battery specific threshold followed by a period of charging with a constant voltage until the charging current fades. The charging system for the $LiFePO_4$ battery pack is designed to generate such a charging pattern and avoid deep discharge and overcharging. It is a located in the ground support and connected to the battery module via the lower umbillicals, the use of sens wires gives the capability of compensating for Omic losses between ground support and battery module. The battery module also has an internal charging system. Due to the power and heat limitations in the payload, this system is only designed as an additional layer of safety and not as the main charging system. The

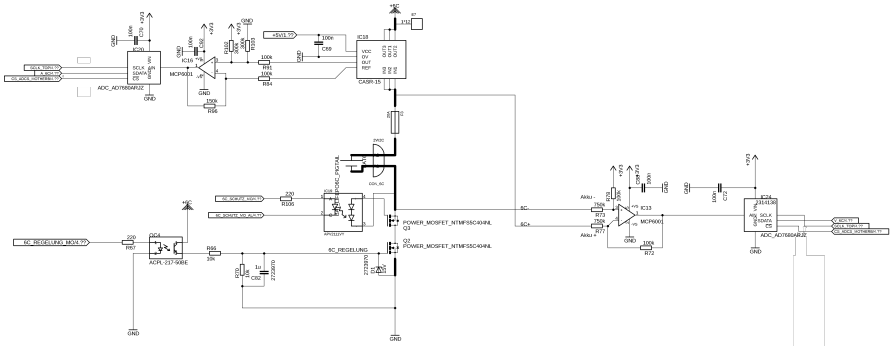

Figure 5.8: Schematic of the main batteries six cell battery charging system. The MOSFETs Q5 and Q4 are connected in opposite directions. For the states charging and discharging one of them is incapable of blocking the current flow. Q5 is regulating the charging current in the constant current phase of a charging cycle, while charging Q4 cannot block the charging current. While discharging Q4 is open until the deep discharge threshold is reached. IC17 is a LEM current sensor described in this section and IC25 measures the battery voltage. The MOSFET gates are isolated from the logic supply by optocouplers.

charging system schematic of the main battery modules six cell battery is shown in figure 5.8, the two cell system is the same. The charging and output currents have to pass two n-type MOSFETS that are connected in opposite directions. For the states charging and discharging one of the n-type MOSFETs is incapable of blocking the current flow. For the case of charging the blocking MOSFET is driven by a low pass filtered PWM signal from the FPGA. It takes care of limiting the charging current in the constant voltage phase of a charging cycle. The other one can only block while discharging. It cuts the output if the battery voltage falls under a threshold level to avoid deep discharging. The charging system is designed for a peak charging current of 30 A (two battery capacities) leading to a charging time of 30 min. While charging the thermal power output due to the resistance of the MOSFETs and the inner resistance of the batteries is 5.87 W. While the balancing modules are active the charging current is reduced to 1 A while the MOSFETs operate in linear mode and the total power will be 4.54 W.The schematics of the motherboard can be found in appendix B.0.2. The motherboard writes its monitoring data to a micro SD card, to be able to investigate the data in case of a critical system failure.

Plug-in output channel boards

The plug-in output boards each contain an ATMega8 microcontroller [7]. This microcontroller is connected to the main FPGA on the motherboard via an Serial Peripheral Interface (SPI). The SPI interface of the plug-in output channel boards is specified in appendix A.9. The motherboards main FPGA controls the switching of the output channel and sends the monitoring data of output current and voltage back to the motherboard. The Mega8 has an eight channel build in 10 bit ADC that is used for the monitoring. The current is measured by two LEM current sensors similar to the model used on the motherboard but with a limited current range of 15 A this leads to an LSB accuracy of 58 mA for the current measurement. The voltage is measured using a resistance divider with 10 kΩ to 15 kΩ for the 2C voltage and 10 kΩ to 68 kΩ for the 6C voltage. This leads to an LSB resolution of 32 mV for the 2C voltage and 100 mV for the 6C voltage. The output channels of the board are also fused at 10 A. The switching of the output channels requires a logical high and a logical low to avoid unwanted turn on events during the tri-stated part of the main FPGA power cycle. The output boards are connected to the motherboard via DSUB 13w3 combi connectors. The schematic

of the power switch boards can be found in the appendix B.1

The overcharge protection system

The overcharge protection module is mounted on top of the battery pack and contains eight commercial overcharge protection elements of type: "LiFePo4 LiNANO Lastmodul mit LED (95mm)" [44] (one for each cell). These protection elements can lead the charging current though three 3 Ω power resistors if one cell in the battery pack is full while the others still need to be charged, they indicate to be in overcharge state by an indicator LED.
To avoid overheating of the module the status of this protection elements is monitored by reading the status of their indicator LEDs with optocoupplers and the charging current is limited to 1 A in case of unbalanced charging, or less in case of overheating. The overcharge protection module also contains the monitoring system for the main battery pack. The voltage of every cell is measured and analog digital converted before it is send back to the motherboard over a multiplexing system. The multiplexer channel is selected over a SPI interface between the output channel board and the motherboard. The SPI connection between multiplexer and main FPGA is isolated by magnetic couples of type: Analog Devices ADUM 5411 [19]. These couplers can isolate up to 4 logic channels and include an isolated DC/DC supply for the isolated side that can deliver up to 150 mW.
Besides the voltages the temperature on the overcharge protection system is monitored using three 10 kΩ NTC thermistors also connected to the multiplexer. Since the measuring system needs to be connected to the main battery pack the signals to the motherboard are isolated using magnetic couplers. To avoid discharging of the batteries due to the connected measuring electronics the measurement electronics can be disconnected using transistors. The schematic of the overcharge protection module can be found in the appendix B.1

The communication board

The communication boards connects inputs from service module, onboard computer and electronic system on its top side to the motherboard on its backside. The grounds of the signal sources are not connected on this board. While the POF interface is intrinsically isolating its transceiver is operating on the ground of the motherboard. The RS232 serial communication to the onboard computer is isolated on the comboard using optocoupplers. The signals from RS422 serial communication and trigger signals between battery module and the service module are isolated on the mainboard. The schematic of the communication board can be found in the appendix B.1

5.6 The laserelectronic-module

5.6.1 Overview of the laser-electronic module

The laser electronic module contains the electronics to support the laser system of the MAIUS-B apparatus. It is separated into an upper and an lower section with a heat-sink in between the two modules. The heat-sink consists of two aluminum plates with a water pipe meander in between, the heat-sink is described in detail in [24]. The lower section on the laser electronic module contains the rubidium laser electronic and a POF switch. The upper section contains the potassium laser electronics.

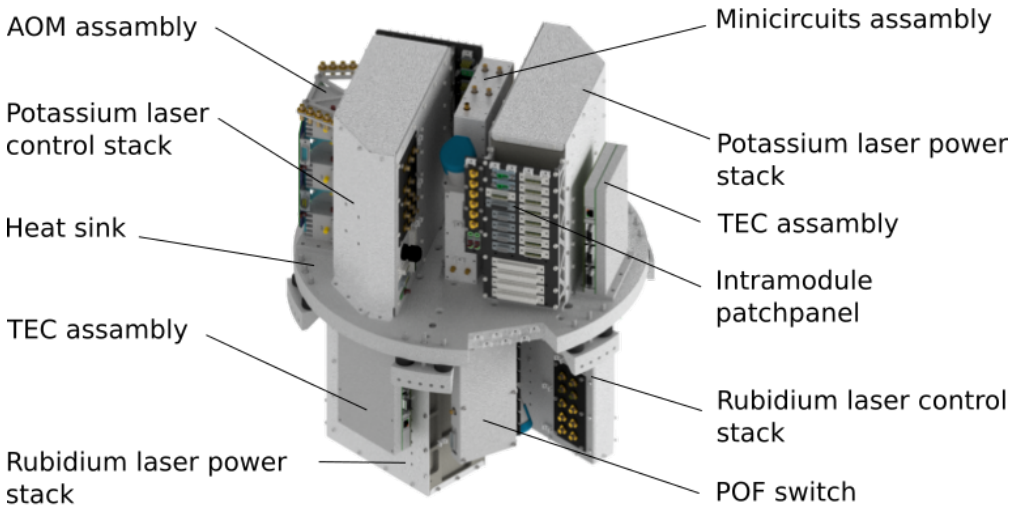

Figure 5.9: AD model of the MAIUS-B laser electronic module. The upper section of the module shows the potassium laser electronics with connection panels on top of the heat-sink. The lower section shows the rubidium laser electronics. Ring eyelets are visible on the top side, they are meant for the construction phase and will not be part of the flight configuration. Technical drawings can be found in appendix B.2.

The upper side also contains patch panels to connect cables coming down from the modules higher up in the payload. Also the connections to the lower section are patched at this panels to make the assembly of the module easier.
Each side carries two stacks with TBus cards. One laser control stack for laser locking and spectroscopy referencing and a laser power stack containing the TA current drivers for the TA lasers. In addition to these TBus stacks both sides carry an almost identical amplifier system for the Acousto-Optic Modulator (AOM) inside the laser system, a Thermo Electric Cooler (TEC) controller assembly and a MiniCircuit assembly, for the amplification and prescaling of spectroscopy and beat signals. All the mentioned modules are described in the following sections. Since the sides are almost identical only the rubidium side will be shown in detail and only differences to the potassium side will be listed. A CAD drawing of the laser electronic module is shown in figure 5.9. The heat-sink design is based on thermal simulation done by the ZARM, the results of this simulations are summarized in appendix B.2 and detailed information regarding the cooling system can be found in [24] The average power consumption of the laser electronic module is 379 W. Its mass is 34.6 kg with a total length of 531 mm.

5.6.2 Rubidium laser electronics

The rubidium laser electronic side contains six separately encased modules.

1. The laser control stack
2. The laser power stack
3. An amplifier and prescaler system for beat and spectroscopy signals
4. An amplifier system for the laser system AOMs
5. A POF switch
6. A TEC control system

The potassium side does not contain a separate network switch and the configurations of the TBus stacks as well as the amplifier systems are slightly different. Of the modules listed, only the laser control stack and the laser power stack will be discussed in more detail in the following section. The focus will be on these modules due to their direct relevance for the experiment. The amplifier system for beat and spectroscopy signals will be discussed alongside with the laser control stack and the amplifier system for the laser system AOMs will be part of the discussion of the laser power stack. More detailed information on the network switch can be found in section 5.4. The basic functionality of a TEC control system will not be discussed in this thesis. The placement of these modules on the heat-sink is shown in figure 5.9.

The laser control stack

The rubidium laser control stack is encased in a special case designed to house up to 12 TBus cards and a fan. The same case design is used for all TBus stack inside the payload. The case is made from aluminum sheets with the exception of the back panel of the stack. The back panel is made from solid aluminum, it holds external power components of the TBus cards inside and acts as thermal bridge to the heat-sink. A CAD drawing of the rubidium laser control stack inside such a case is shown in figure B.49 in the appendix. The laser control stack contains seven TBus cards:

- Power and POF interface
- Shutter (16 channels)
- Fan controller (8 channels)
- DDS (2 channels based on AD9958)
- Frequency controller (spectroscopy, 3 beat channels, 4 laser channels)
- 2 × Laser current driver (MO-version with 2 output channels with 300 mA each)

The laser control stack drives the rubidium reference laser and locks it on a rubidium spectroscopy using the control loop described in section 5.9. The reference laser is beated in the laser module with the three remaining rubidium lasers. The signal from the spectroscopy and the beat photodiodes are amplified in the amplifier system for beat and spectroscopy signals and lead into the frequency controller card. The frequency controller card then calculates the necessary offset currents and provides an offset signal for the two current drivers (4 channels in total). This scheme is further described in section 5.9. The shutter card in this stack besides shutters in the laser system controls a multiplexer inside the amplifier system for beat and spectroscopy signals that picks the output signal from this group. The DDS card provides the signal for the rubidium AOMs inside the laser system. The fan controller provides power for the fans inside the whole laser electronic module. The potassium laser control stack has the same task for the potassium reference lasers. Since it needs to support one more laser, one more frequency controller and one more laser current driver are necessary here. The potassium laser control stack also does not contain a DDS or shutter card, but a 2C-6C adapter board to power the TEC assembly and a photo diode input board. The 2C-6C adapter board is a simple component that generates a 2 cell output voltage from a 6 cell voltage input. This is necessary since the drain of the TEC controllers on the 2 Cell battery would lead to a short lifetime of the 2 cell battery while the 6 cell battery would remain almost full.

The rubidium laser power stack

The rubidium laser power stack powers the rubidium power amplifiers of the MOPA lasers and provides the signals for the AOMs. It contains the following cards:

- Power and POF interface
- 3 × DDS (2 channels based on AD9958)
- 4 × TA current driver (TA-version with one output channel with 2 A per card)

The TA current drivers are a special variant of the laser current drivers also described in section 5.7.3. Since these laser current drivers have to provide 2 A for the TA lasers, they have power electronics mounted on the back side of the stack and a separate power input from the main battery. The potassium laser control stack houses one more laser current driver card.

Amplifier and prescaler system for beat and spectroscopy signals

The amplifier and prescaler system for beat and spectroscopy signals is located in both, the potassium and the rubidium section, in between the laser power and the laser control stack. The rubidium system consists of four amplifier chains. Beat signals from the laser system are amplified by two Minicircuits ZX60-14012L amplifiers with a bandwidth of 300 MHz to 14000 MHz and a gain of 12 dB (typical) [55].
After passing the last amplifier the signals are feed into RF-splitters. One output port of the splitters is connected to an output port on the side of the module, while the other is connected to a mechanical RF Multiplexer of type: Minicircuits MSP4TA-18+ [53]. The output ports are connected to the frequency controller card in the laser control stack to form offset locks. The output ports of the mechanical multiplexer are connected to the an input of a frequency controller card in the potassium section. This input allows to check the beat signals from the laser modules over a broader frequency range. CAD model and schematic of this module can be found in appendix B.2.3

5.6.3 Theory of operation of the laserelectronic module

The light from the reference lasers described in section 3.2.6 is splitted in an 80/20 ratio with 20% feed into a Modulation Transfer Spectroscopy (MTS). The light from the MTS is detected by a photodiode. The signal of this photodiode is then lead to the frequency controllers spectroscopy input inside the laser control stack in the laser electronic module, via the amplifier and prescaler system. The signal is analog to digital converted on this card by a 12 bit ADC with 25 M samples per second and demodulated by the FPGA. The signal generated by this technique provides a zero crossing at the exact position of the atomic transition addressed by the reference laser. This feature can be used to form a control loop and lock the laser to this transition. Even though other techniques have been described [9] the technique described here is the most tested one for the task and has proven to be capable of zero gravity application.
With the reference laser locked to an atomic transition the experiment lasers can now be offset locked to the reference laser. The exact configuration of the control loop on the frequency controller and the current driver is discussed in section 5.9. Every experiment laser provides a 99/1 ration fiber splitter. While the bulk of the light is directed to the experiment, 1 % is feed into beat nodes with the reference laser. The beat signals from these nodes are also directed to frequency controller cards in the laser electronic module. Before they are feed into the frequency controllers they are amplified

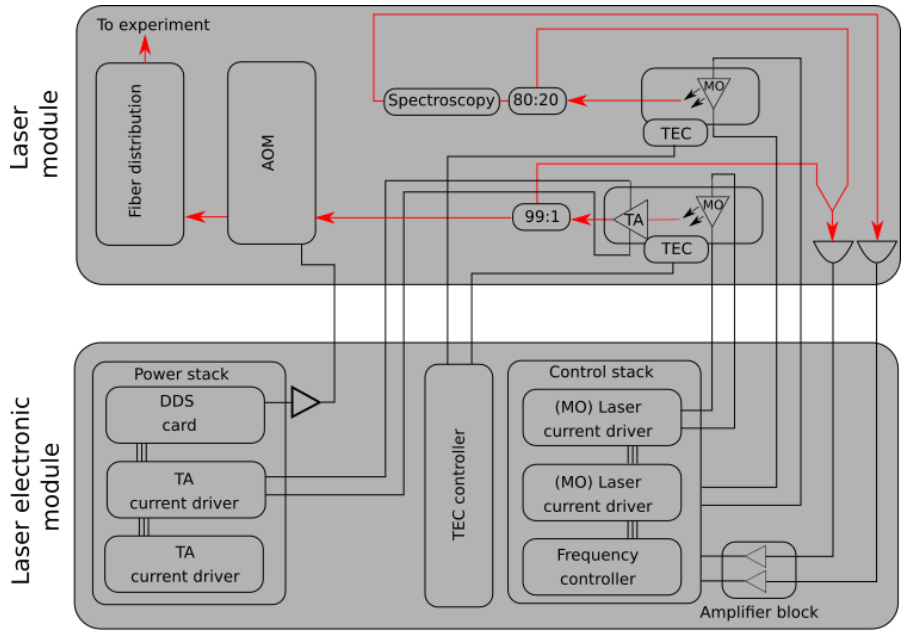

Figure 5.10: Schematic picture of the laser electronic modules working principle. The picture shows a reference laser and an experiment laser inside the laser module. The reference laser is feed into a spectroscopy cell and the spectrum measured by a photodiode is lead into the frequency controller in the laser control stack. There the set-point for the reference laser is determined and feed to the current driver forming a control loop. 1% of the experiment lasers light is lead back to beat node with the reference laser. This photodiode signal is also processed on the frequency controller an offset lock with the second current driver is initiated. The TA current drivers in the power stack supply the optical amplifiers and the DDS card in this stack feeds the AOMs.

in chain of amplifiers in the amplifier system for beat and spectroscopy signals that is described in 5.6.2. Using frequency counters on the frequency controller and knowing the absolute frequency of the reference laser by the atomic transition it is locked to, an offset lock can be applied to the experiment lasers. This offset locks allows to stabilize the experiment lasers in reference to the reference laser. For the flight configuration this locks will be replaced by a digital phase lock software module. This module is described in [61]. The current drivers in the laser power stack supply the Tapered Amplifier (TA) in the laser module. This current driver delivers up to 2 A. Additionally the laser power stack contains DDS cards that generate the signals that control the AOM in the laser electronic module. For this purpose the signals from the DDS cards are amplified in the AOM amplifier assembly that houses a power amplifier of type AMPA-B-34 [59] for each AOM in the laser system. A schematic picture of the working principle described above is illustrated in figure 5.10. The combined POF and Ethernet switch present on the rubidium section is described in section 5.4. The TEC control system that is present on the rubidium and the potassium side is a simple carrier module for commercial Meerstetter TEC-1091 TEC controller [46] with a cooling power of up to 42 W that will not be described in detail in this thesis. Each module carries six of this meerstetter modules that control Peltir elements on the heat-sinks of TA lasers and other components in the laser system. CAD model and schematic of this module can be found in appendix B.0.2

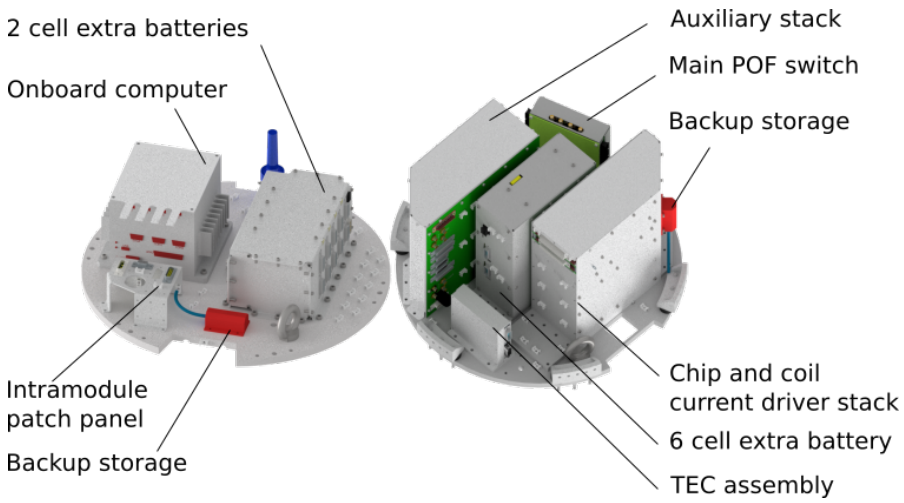

Figure 5.11: CAD model of the electronic module on the top side the onboard computer and the two cell extra batteries are visible. Ring eyelets are visible on the top side, they are meant for the construction phase and will not be part of the flight configuration.

5.7 The electronic module

5.7.1 Overview of the electronic module

The electronic module contains the electronics to support the physics package. Like the laser electronic module it is separated into upper and lower section with the heat-sink in between the two modules. The upper part (computer section) contains the on-board computer and a set of two cell extra batteries needed for a galvanic isolated supply of the chip current drivers and the microwave system. The lower section (chip and coil current driver section) contains two TBus stacks. One responsible for the operation of the chip and coil current driver and one for a variety of different tasks to support the physics package. Besides the two TBus stacks the lower section houses a TEC controller for the physics package, a combined POF and Ethernet switch described in section 5.4 and a six cell extra battery pack responsible for the operation of the coil current drivers described in 5.5. From the components housed in the electronics module the extra batteries and the TBus stack will be discussed in more detail in the following sections.
The electronic modules consumes an average electrical power of 174 W from the main battery and additional 200 W from the extra batteries. The module weighs 31.2 kg with a total height of 400 mm. A CAD drawing of the module is shown in figure 5.11

5.7.2 Computer section

The computer section is the upper most section of the pressurized part of the payload. The main computer is a PCIe-104 module computer in an IDAN-case. The board containing the main CPU is an Intel core i7 CPU with 4 GB of RAM and a 32 GB SSD of type: CMA34CRQ2100HR [72]. It is connected to an 190 W IDAN power supply module of type: RTD IDAN-ATX3510HR-190W. The PC is outfitted with an additional USB extension for the two detection cameras and USB drive backup data storages. The onboard computer is connected to the main battery module over a serial connection of type RS 232 and to the Service module over a serial connection of type RS 422.
The two cell extra battery module is an assembly of six TBus cards. Five two-cell battery cards and one POF and power interface card. The two cell extra battery cards

are designed as an galvanic isolated power supply for the chip current drivers and the microwave system. Each board carries two $LiFePO_4$ cells of type: A123-Systems ANR26650M1B [1] with 2.5 Ah capacity. The outputs of these cards is fused to 10 A and the charging current is limited to 1.6 A. The charging current for this extra batteries is delivered by the ground support through the upper payload umbilical. The computer section also contains a patch panel that connects to the connectors in the upper sealing plate

5.7.3 Chip and coil current driver section

The chip and coil current driver section contains two TBus stacks, one in the same cases design described in 5.6.2 and one in a slightly modified version. The modified stack contains the chip and coil current drivers and the other contains additional electronics to support the physics package. Both stacks will be discussed in detail in the following section. Besides these two stacks this section contains a six cell extra battery for the coil current drivers, a TEC control group and a combined POF and Ethernet switch. The six cell extra battery supplies the coil current drivers. Its design is widely identical to the design of the main battery with the two cell pack and charging electronics missing. The combined POF and Ethernet switch is described in section 5.4.

The chip and coil current driver stack

The chip and coil current driver stacks task is to provide current for the structures of the atom chip and the MOT coils. This is done using four chip and coil current driver TBus boards. Each board provides output for two coils or chip structures. The output stages of this current drivers are powered by the extra batteries described in 5.7.2 and 5.7.3. The chip and coil current driver boards are based on the design used for the QUANTUS and the MAIUS 1 missions designed by [65].
Before the current is lead into the atom chip structures it is guided through two chip protection boards. These boards contain fuses, monitor the current and are able to switch the current into the chip structures and coils off. The chip protection boards are compatible with the TBus but need a larger form factor, that leads to a different case design for the case of the chip and coil current driver stack, this chip protection boards are explained alongside the chip and coil current drivers in section 5.9. A CAD drawing of this case can be found in appendix B.2 Additionally to the current drivers and the protection boards the chip and coil current driver stack contains a POF and power card. A more detailed description of the chip and coil current driver cards can be found in section 5.9.

The AUX stack

The second stack on the chip and coil current driver section contains eight TBus cards in total:

- POF and power card
- $2 \times$ DDS card (2 channels based on AD9958)
- Trigger output card
- $2 \times$ Microwave back-end cards (2 channels each)
- NTC input card (25 channels)

- Photodiode input board (25 channels)
- Fan controller card (8 channels)

The two DDS cards are generating the signals for mixing with the microwave sources outputs, to generate the microwave evaporation signal. The microwave back-end cards are controlling the microwave electronics that are mounted on the electronic stack inside the physics package. The exact configuration of the microwave evaporation system is described in 6.5. The NTC and photodiode input boards serve monitoring purposes and are connected to sensors inside the physics package. On the side of the aux stack the microwave system for potassium is mounted. This system is mounted on the EL layer to conserve space on the top side of the physics package. It includes a microwave front-end, a frequency mixer and and two additional amplifiers. This system is explained in more detail in section 6.5.

5.7.4 Concept of operation

The chip and coil current drivers inside the chip and coil current driver stack generate the currents required by the experiment. The power inputs of this current drivers are connected to the extra batteries on the the computer and chip and coil current driver section to guarantee isolated supplies for the chip structures and the coils. The stack itself is powered by the main battery. The 4 chip and coil current drivers have 8 output channels in total, the connections between theses channels and the atom chip structures and the coils are listed in table 5.1.
The corresponding connection pattern of the atom chip can be found in appendix A.2.

Current driver	Channel	Function	Current range	Polarity
1	A	Science chip Z-structure	2 A	Unipolar
1	B	Base chip Z-structure	6 A	Unipolar
2	A	Mesoscopic U-structure	10 A	Unipolar
2	B	Mesoscopic H-structure	10 A	Unipolar
3	A	Y-coil	10 A	Bipolar
3	B	X-coil	10 A	Bipolar
4	A	Z-coil	10 A	Bipolar
4	B	2D-coils	10 A	Unipolar

Table 5.1: Functions of the 4 chip and coil current drivers used in the experimental setup. Every current driver provides 2 channels (A and B). The exact connection pattern on the atom chip can be found in appendix A.2. The same type of current driver is used for coils and chip structures.

The 3 connections of the mesoscopic H-structure are conneced in series. The currents generated by the current drivers are generating the trap configuration like described in section 3 and 4. More detailed information can be found in [64].
The auxiliary stack contains DDS cards used to generate the evaporation signals. Two DDS signals are mixed with outputs from microwave front-ends in the physics package to generate the rubidium evaporation signals, see also 6.5. One additional signal DDS signal is mixed with the output of a microwave front-end potassium variant board on the side of the aux stack to generate the potassium re-excitation signal. A fan card in the auxiliary stack powers the fans in the other assemblies. The shutter card inside the auxiliary stack is used to switch the microwave power amplifier inside the physics package. The onboard computer is used for data storage and overall experiment control. A schematic of connections related to the most important functions of the electronics module is shown in figure 5.12

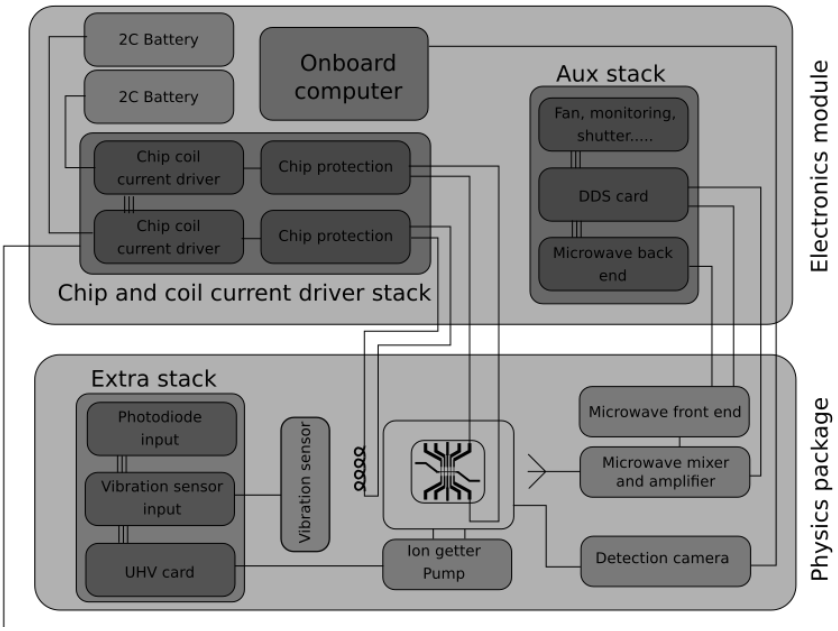

Figure 5.12: Schematic picture of the electronic modules working principle. The picture shows the connections between the physics package and the electronic module. The chip and coil current drivers inside are supplied by the extra batteries. They power the MOT coils and atom chip structures. The chip protections boards inside the same stack fuse and monitor these currents. DDS cards in the auxiliary stack supply the signal for the microwave evaporation system in the extra electronic stack inside the physics package.

5.8 Electronics inside the physics package

The electronic section inside the physics package is housed in an aluminum frame mounted on top of the physics package. Inside it contains a TBus stack with:

- POF and power card
- Photodiode input board (25 channels)
- Vibration sensor input board
- Vaccuum sensor card (for Pfeiffer IKR-270)
- IGP driver card (single channel, 8 kV, 50 µA)

Two microwave front-end boards described in section 6.5 are mounted on top of the stack. This front-ends are tasked with generating the microwave frequencies needed for the evaporation of rubidium 87. The top side also contains 2 filters and 2 additional amplifiers for the microwave systems. Two frequency mixers for the evaporation system are present on the side of the stack. The final amplifier stage for the potassium re-excitation microwave signal and the rubidium evaporation signal is located on the back side of the stack. The side of the stack also contains an additional electronic box, that contains a circuit for the switching of the power amplifiers on the backside of the stack, controlled by a shutter card. Layout and schematic of this circuit can be found in appendix B.4.1. The potassium microwave source and additional amplifiers are located on the side of the AUX-stack on the EL layer to conserve space around the extra stack. Detailed information on the setup of the microwave system can be found in 6.5. The electronic system inside the physics package enables the operation of the vacuum system during transport when the physics package is not connected to the electronic

module. It also increases the high voltage safety of the the electronic system, be moving the HV IGP controller card close to the IGP. Furthermore the proximity of the rubidium microwave front-ends to the experimental chamber helps to prevent losses in the microwave signals on long transmission lines. A CAD drawing of the extra stack can be found in appendix B.53.

5.9 The current drivers

Three types of current drivers are used in the MAIUS-B experiment: Master oscillator laser current driver, tapered amplifier laser current driver and Chip and coil current driver. Different to the MAIUS-A setup, the later are a combined device for chip structures and coils. Since the laser current drivers as well as the chip and coil current drivers for MAIUS-A have been part of the work in [9] and [65] this section will only focus on differences and improvements to the MAIUS-A versions.

5.9.1 The laser current drivers

Both the laser and the TA current driver are based on their predecessors described in [9]. The MAIUS-B models are like their predecessors build by Dr. Thijs Wendrich based on an article by [43]. They are designed for very low current noise and optimal DC stability. Both models allow for a change of set points within a range set by soldering options, by the control software. Each Maser Oscillator (MO) current driver has two independent outputs with a maximum current of 230 mA and provide a high speed modulation input with a modulation current is 32 mA for locking applications. This modulation current can be delivered by a frequency controller over the TBus. The maximum modulation current sets the maximum free tuning range of a laser connected to the current driver depending on the lasers tuning coefficient. The TA variant current drivers have one output that is capable of delivering up to 2.5 A. They have an additional input for a signal from a photodiode, that allows for power stabilization of the connected TA laser. The power control scheme is realized with a digital Proportional Integral Derivative Controller (PID) inside the current drivers main FPGA. Other than the previous variant of this current driver described in [9] the MAIUS-B variants power output is not powered over the TBus. This was not possible with the 4 TA current drivers present in the rubidium laser power stack described in 5.6. The total output current of this current drivers would be 8 A which is not possible to be conducted through the PC-104 connectors. Therefore the TA variant current driver has a separate Dsub 3W3 power input connector supplied by the main battery. The power transistors of the TA variant current drivers are on a separate aluminum board that can be mounted on the back plane of a stack for a better thermal connection to the heatsink. According to the specifications of the lasers used in the laser system, the MO laser current drivers are set to a maximum current of 230 mA and the TA current driver to a limit of 1.7 A. Layout and schematics of the TA and MO variant current divers can be found in appendix A.8.

5.9.2 The chip and coil current drivers

The chip and coil current drivers are based on the MAIUS-A model described in [65]. The MAIUS-B variant is modified to work with the 2 cell and 6 cell power supply described in 5.5. The modifications needed for the new power supply lead to a new output stage that is capable of bipolar driving chip structures and coils with up to 10 A, while using an unipolar power supply.

While the analog control circuitry is identical to the MAIUS-A variant, the output DAC was replaced with an 18 bit variant instead of a 16 bit variant in the MAIUS-A version. This allows for compensation of thermal fluctuations that are in the order of magnitude of 40 µA [65]. The chip and coil current drivers power MOSFETS also are mounted on separate aluminum PCB that can be mounted on the back plane of the stack.
Schematic and layout of the chip and coil current driver can be found in appendix A.8. For the measurements presented in chapter 7, the MAIUS-A version of the current drivers is used.

5.9.3 The chip protection board

An additional layer of protection between the chip and coil current driver and the atom chip a chip protection board was created. It connects on the input side to the chip and coil current driver and on the output side to the atom chip. This board is capable of monitoring and switching of the currents that flow into the atom chip. This board also contains a melting fuse and a self resetting fuse per channel for the atom chip currents. For the flight campaign the melting fuse is replaced by a wire.
The status of the two fuses is measured measured over one optocouppler. This leads to a leakage current through the atom chip even if one of the fuses triggered but increases the usability of the component.
The measurement of the currents is done by the voltage over a resistor, read out by external 16 bit ADC present on the PBC. The board is based on a MAX10 FPGA. The current to the atom chip structures is also fused in software with a selectable limit. One of the chip safety boards can secure 4 chip and coil current driver ports. The chip protection board is TBus compatible with a slightly elongated form factor.

CHAPTER 6

The microwave evaporation system

The microwave evaporation systems is a central part of this thesis. It is, along with the chip and coil current drivers, the only component that has an almost direct interaction with the atomic ensemble. Furthermore it is a component that is not based on any earlier TBus components developed in the LASUS project for the QUANTUS missions, but specifically developed for the MAIUS 2 and BECCAL missions. Commercial components that both fit the volume constraints and operating parameters of the MAIUS mission are not available. Thus an extensive custom design of the microwave evaporation electronics was necessary and will be discussed in detail in the following sections. The next section will lay out the technical requirements for the design of the microwave evaporation system. The following sections will then describe the design of the microwave source and show its characterization. Afterwards, from the characterisation of the source, the configuration of the overall system, including additional RF-components and amplifiers, will be derived. The characterization of the overall microwave evaporation system will be the last section of this chapter. The performance in generating a BEC, of the system compared to the MAIUS-B ground evaporation system will be part of chapter 7.

6.1 Technical requirements of the microwave evaporation system

The microwave evaporation system consists of a signal source, a frequency reference and microwave components like frequency mixers and amplifiers. The technical design goals for the microwave evaporation system can be split into two classes: Design goals that arise from the operation within the electronic system of the sounding rocket and design goals that arise from experimental steps. On the side of the environment of operation, one major design goal for the microwave evaporation system was to be compatible with the TBus environment described in section 5.2. Additionally the transmission lines from the microwave system to the experimental chamber needed to be short to avoid signal losses. That also means that parts of the evaporation system inevitable has to operate close to the science chamber. This fact poses requirements on the electromagnetic compatibility. Without further investigation it was decided to fullfill this requirement by the restriction on the use of switching regulators on the front-end, filtering of supply lines and using a grounded aluminum casing. To satisfy the needs of the experiment the system needs to be able to address the atomic hyper-fine transitions of:

- $^{87}\mathrm{Rb}\ |5^2S_{1/2}, F=1\rangle \rightarrow {}^{87}\mathrm{Rb}\ |5^2S_{1/2}, F=2\rangle$ at 6.834 GHz
- $^{85}\mathrm{Rb}\ |5^2S_{1/2}, F=2\rangle \rightarrow {}^{85}\mathrm{Rb}\ |5^2S_{1/2}, F=3\rangle$ at 3.035 GHz
- $^{39}\mathrm{K}\ |^2S_{1/2}, F=1\rangle \rightarrow {}^{39}\mathrm{K}\ |^2S_{1/2}, F=2\rangle$ at 461.7 MHz

- $^{40}\mathrm{K}\,|^2S_{1/2}, F = 9/2\rangle \rightarrow {}^{40}\mathrm{K}|^2S_{1/2}, F = 7/2\rangle$ at 1285.8 MHz
- $^{41}\mathrm{K}\,|^2S_{1/2}, F = 1\rangle \rightarrow {}^{41}\mathrm{K}\,|^2S_{1/2}, F = 2\rangle$ at 254.0 MHz

For a microwave evaporation like described in section 3 and state preparation. The level diagrams of the relevant rubidium and potassium isotopes can be found in appendix A.10.
Even though only the $^{87}\mathrm{Rb}\,|5^2S_{1/2}, F = 1\rangle \rightarrow {}^{87}\mathrm{Rb}\,|5^2S_{1/2}, F = 2\rangle$-transition at 6834.7 MHz and the $^{41}\mathrm{K}\,|^2S_{1/2}, F = 1\rangle \rightarrow {}^{41}\mathrm{K}\,|^2S_{1/2}, F = 2\rangle$-transition at 254.0 MHz are relevant for the MAIUS-2 mission. The need for a wider range of addressable frequencies arises in the BECCAL mission. Ideally the system needs to be able to address all transitions listed above with the capability to perform frequency ramps of 50 MHz around each target frequency for the evaporation.
The resulting wide dynamic range between 200 MHz and 6.9 GHz challenges the electronic components available on the market today. The line-width of the evaporation signal needs to be in the 1 kHz regime to be able to perform pulses on a 1 ms time scale. For every evaporation target frequency the system needs to provide two separate output frequencies, to be able to re-excite atoms that got lost to off-resonant states during the evaporation, like described in section 3. Also the technique of a STIRAP transfer, described in 3, instead of the adiabatic rapid passage between the m_F-states will be tested within the MAIUS mission. This technique requires the capability of ramping the signal amplitude while maintaining a fixed frequency. The output power of the microwave source needs to match the requirements of two power amplifiers planned to be used as a final stage before coupling the system into the experiment. This power amplifiers are a Minicircuits ZVE-8G+ [57] for the rubidium system, and a AMPA-B-34 amplifier [59] for the potassium system. The ZVE-8G+ amplifier has an amplification of 35 dB nominal at an output frequency of 8 GHz. The AMPA-B-34 amplifier has 35 dB amplification at an output frequency of 235 MHz. The baseline power output of the microwave systems is the power output used in the MAIUS-B ground system. Behind the power amplifiers this power is 20 dBm for both systems [64].
That means that the output amplitude of the system created needs to be at least -15 dBm at the relevant frequencies. The technical requirements of the microwave evaporation system summarized are:

- Address target frequencies in the range between 0.2 GHz and 6.8 GHz
- Flat output power profile in this range with output power better than -15 dBm
- Low noise operation
- TBus compatible
- Possible operation close to the experimental chamber
- Two independent output channels per unit
- Linewidth under 1 kHz
- Frequency tuning ± 50 MHz around target frequency
- Amplitude tuning P_{max} - 20 dBm

6.2 Design of the microwave evaporation signal source

6.2.1 The microwave front-end board

To satisfy the first two technical design goals mentioned in section 6.1 of being to be TBus compatible and being capable of operating close to the physics package, the system consists of two separate boards.
A TBus compatible back-end board responsible for power supply and interfacing between a microwave front-end board and the TBus. The front-end board acts as a microwave signal source and contains the microwave electronics, it is created in a very small form factor of 53 mm × 53 mm, that can be mounted inside the physics package even with its back-end board being in another module. The front-end board is based on an "HMC834 fractional N-Pll with integrated VCO" chip by Analog Devices [5]. This combined PLL and VCO chip has a fundamental mode of 2800 MHz to 4200 MHz by a VCO-core of 32 VCO with overlapping bands. The output stage of this chip has a divider stage of up to 1/64 and is capable of multiplying the output of the divider stage by a factor of two 2. This leads to operational bands of:

- 45 MHz - 1050 MHz
- 1400 MHz - 2100 MHz
- 2800 MHz - 4200 MHz
- 5600 MHz - 8400 MHz

The HMC 834 covers all frequencies demanded in section 6.1 except for the $^{40}K\ |^2P_{1/2}, F = 9/2\rangle \rightarrow |^2P_{1/2}, F = 7/2\rangle$ frequency at 1285.8 MHz . This frequency can be addressed by mixing the sources output signal with another output from the tunable reference. The HMC 834 needs an external loop filter. The filter used on the front-end board is set to bandwidth of 130 kHz like recommended by the data sheet. The feedback path from the VCO core to the Phase Frequency Detector (PFD) has a build-in 18 bit integer and 24 bit fractional divider. The reference signal first passes a 14 bit divider. The maximum PFD frequency is 100 MHz.
Besides two of the HMC 834 pll chips, the front-end board contains one amplifier of type Minicircuits LEE-39+ [54] with an output power of 10.4 dBm and two attenuators of type HMC 540 [4] per channel to satisfy the need for amplitude ramping. The attenuators have a 8 bit parallel interface for 1 dB steps up to 15 dB attenuation. Both channels of one front-end are then combined by a power splitter combiner. The splitter combiner is selected to be a Minicircuits GP2X1+ [52] with a nominal frequency range between 2800 MHz and 7200 MHz for the rubidium variant of the front-end and a GP2S1+ [51] (500 MHz - 2500 MHz) for the potassium variant. To make the serial communication between the front-end boards HMC 834 chips and the back-end controller more flexible and store sequence values, a EPM240F100C5 CPLD is part of the front-end. The basic setup of the front-end board is illustrated in figure 6.1. The front-ends have two SMA connector inputs for the frequency reference, connected to the reference inputs of the two HMC 834.
A tunable reference is the preferred method to tune the output frequency of the front-end board. Even though the HMC 834 is capable of setting an output frequency over the serial interface and re-calibrating itself. The calibration time of the HMC 834 is given by equation 6.1 [5]

$$T_{cal} = k \cdot 100 \cdot T_{FSM} + 6 \cdot T_{PD} \cdot 2^n + 7 \cdot 20 \cdot T_{FSM} \tag{6.1}$$

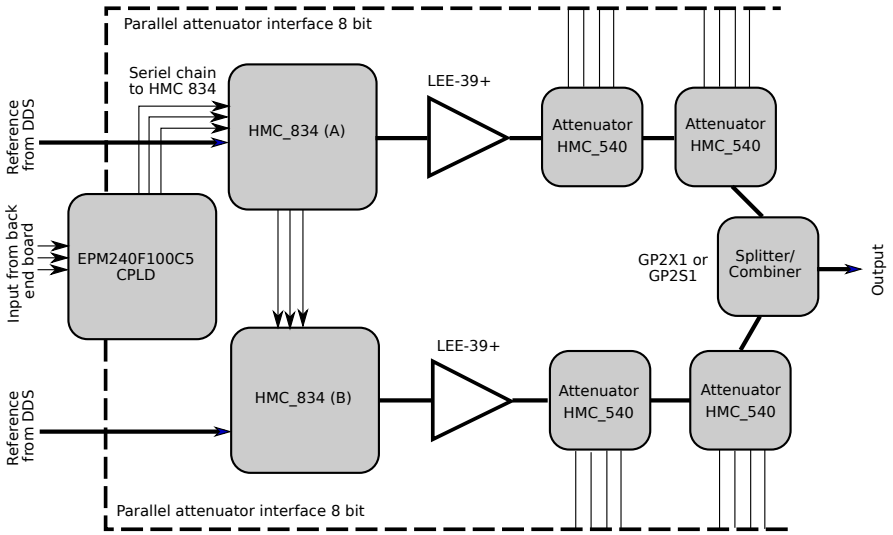

Figure 6.1: Illustration of the basic setup of the microwave front-end. The two HMC 834 ICs are connected to the CPLD by a serial chain (triple solid line), while the attenuators are connected by a parallel interface (dashed line). The splitter combiner at the output has two options depending on the atomic species.

were T_{FSM} is the time required for a cycle of the finite state machine running on a maximum clock speed of 50 MHZz, T_{PD} is the time required for a phase frequency detector cycle, n the number of measurement periods and k is a programmable number of wait cycles. With the maximum FSM clock speed of 50 MHz, and a minimum number of measurement and wait cycles of one, at 6.8 GHz output frequency. Equations 6.1 leads to a calibration time of 4.8 µs, during which the state of the PLL is not defined. This undefined state can be avoided by reaching the setpoint using a tunable external reference. Additionally the HMC 834 showed a recalibration time in the order of 1 ms after a change of the setpoint that required a jump to a new core VCO. Thus the reference inputs are planned to be used to form a frequency ramp over the TBus DDS cards in the electronics module, once the HMC 834 is seeded to a set point. The exact referencing configuration is discussed in more detail later in this chapter.
To reach the frequency of the $^{41}K\,|^2S_{1/2}, F = 1\rangle \rightarrow ^{41}K\,|^2S_{1/2}, F = 2\rangle$ transition at 254.0 MHz the internal VCO has to be divided by 14. This leads to a possible output frequency range between 200 MHz and 342 MHz. However the VCO core of the HMC 834 is made up by 32 sub oscillators that have overlapping frequency ranges. Once the reference frequency demands for a re-calibration of the VCO core the output frequency is discontinuous. This leaves only a free tuning range of 3.13 MHz operating at the divide by 14 output divider, to ensure no jump to a new core VCO occurs. This range is insufficient according to the design goals described in 6.1. To extend the possible tuning range the output channel of the microwave system can be frequency mixed with an additional output port of the DDS card, like illustrated in figure 6.2.
The schematic of the RF chain of the microwave front-end is shown in appendix B.0.17. From the schematic the expected output power can be derived using the device data sheets. The expected losses of a device are written in the schematic. With the nominal output power of the Minicircuits LEE 39+ amplifier of 10.5 dBm and a total power loss of 9.6 dBm due to the injection losses of the attenuators and the splitter-combiner the front-end is expected to provide an output power of -10.1 dBm. The HMC 834 pll is expected to supply an output power of -11 dBm. Additional losses are expected from other components on the PCB and injection losses into the transmission line. Additional external amplifiers are necessary to reach the power requirement. The exact

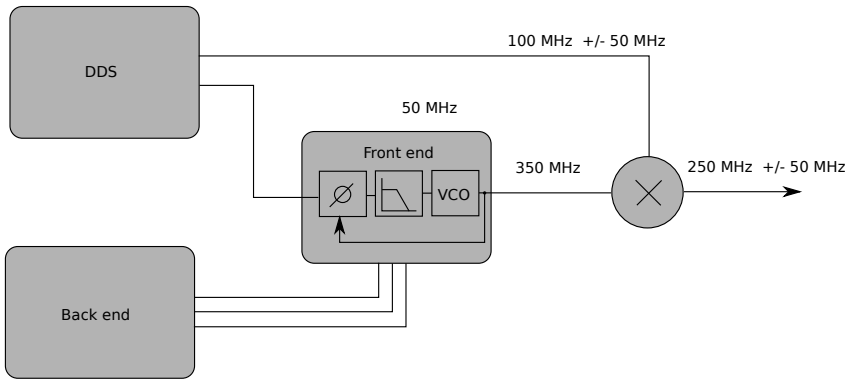

Figure 6.2: Illustration of the RF mixing setup used to increase the output frequency tuning range of the microwave front-end board at 250 MHZ. The Output signal of the microwave front-end is mixed with a 100 MHz signal from the DDS card. The front-ends output frequency is placed above the target frequency to avoid evaporation of lower energy states.

setup of the overall system will be shown in section 6.3. The measured output power of the front-end board over output frequency is shown in figure 6.4. In the figure the output power of the rubidium and potassium variant front-ends are shown over output frequency. For comparison the output power of the HMC 834 evaluation kit is also shown. The red marked zones are zones that are not within the operating range of the HMC 834. For the comparison of the front-end and the HMC 834 evaluation kit. One has to keep in mind that injection losses of additional microwave components and the mixer are not present on the evaluation kit. Also the additional amplifier is not present on the evaluation board.
The microwave front-end described here will act as the microwave source for the overall microwave system. It is characterized apart from the overall system in section. 6.3. The microwave front and has a weight of 150 g and a power consumption of 10 W. Even though the back-end board described in the next section is supposed to power the front-end, additional filtering is required on the 5 V power supply, which is connected directly to the charge pump and the VCO core of the HMC 834 chip. Filtering was not included on the front-end board itself to conserve available PCB space.

6.2.2 The microwave back-end board

The microwave back-end board powers and controls two microwave front-end boards. It is designed in the TBus standard described in section 5.2. The back-end is based on an Intel MAX10 10M08SCE144 FPGA [37]. This FPGA controls the back-end functions and is tasked with the serial communication with the connected front-ends. The created three wire serial protocol (CLK, CS, DATA) needs to transmit two different types of commands: The serial communication with the two HMC 834 chips (288 bit) and the setpoint signal for the output attenuators (16 bit). The attenuators are addressed on a CS low and the HMC chips on a high signal on CS. During the transfer of the attenuator setpoint, one additional bit is transferred, to set the target pll for the next HMC834 transfer. The serial communication was developed by the "Institut für Mikroelektronische Systeme" in Hannover. The connection is realized using Low Volt Differential Signal (LVDS) connections to allow for longer transmition lines at high bit rates. A description of the serial communication protocol can also be found in appendix A.9. The

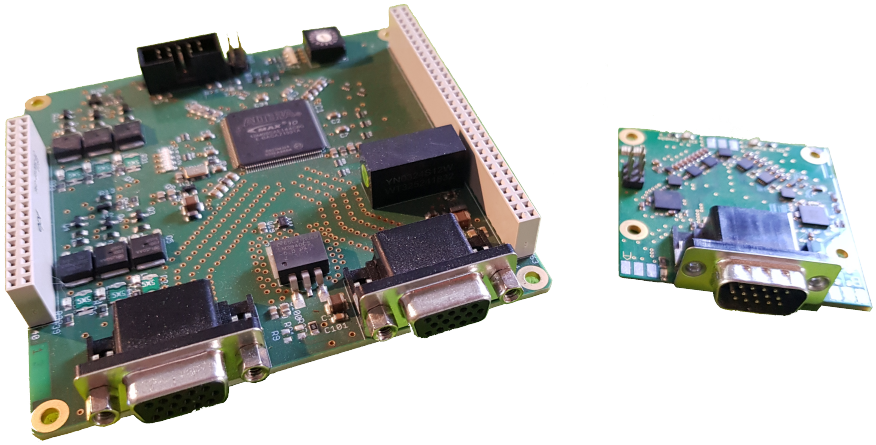

Figure 6.3: Foto of the microwave system. The back-end board is shown on the left next to the front-end board on the right.

back-end board provides output voltages of 3.3 V, 5 V and 12 V to the front-ends. The output voltages are switchable by the FPGA. Both the serial communication and the power supply lines for each front-end are connected via a DSUB HD15 connector. Its pin assignments can be found in appendix A.7. The back-end board is designed to supply two front-ends while build into the electronic system, that is supplied by the battery module described in 5.5. This means the board is not designed to have a good power supply suppression ratio, since the $LiFePO_4$ batteries are are one of the lowest noise power sources available [34]. If the back-end board is used for ground operation, for example with a laboratory power supply, additional filtering has to be applied to the 5 V supply line between front and back-end. This supply is directly connected to VCO and charge pump of both HMC 834 plls. This means that every disturbance on this line will show unsuppressed in the output signal of the front-end. The HMC 834 evaluation kit circumvents this effect by using highly specialized voltage regulators (HMC1060LP3E and HMC860LP3E) [5]. Layout and schematic of the back-end board can be found in appendix B.0.14. A picture of the microwave system including front-end and back-end board is shown in figure 6.3.

6.3 Characterization of the microwave evaporation signal source

6.3.1 Output power

The most important characteristics of a microwave source like the one described above are phase noise, spurious performance, and the output power. To start the characterization of the microwave signal source the output power of the potassium and the rubidium variant are measured against the output frequency.
The output frequency is chosen by the control software and the corresponding amplitude measured with a RIGOL DSA875 spectrum analyzer. This spectrum analyzer is able to measure up to 7.5 GHz. The device was calibrated for the SMA cable of 25 cm length. The results of this measurement are shown in figure 6.4. One should note that a measurement in the red marked zones is not possible. The front-end can not reach this frequency's due to the limitations of the HMC 834. The plot also shows the results from the HMC 834 Evaluation Kit. During the measurement the on board attenuators of each front-end have been turned off to avoid intermodulation in the output stage. The HMC 834 operated in integer mode with the output stage amplification turned off.

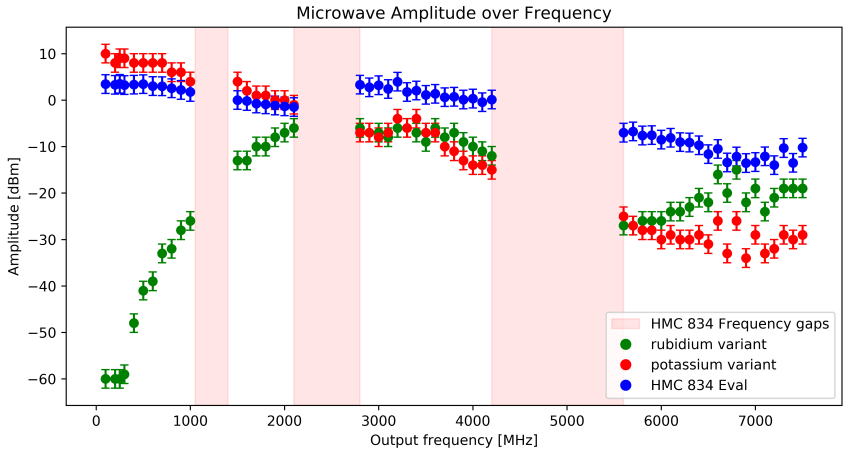

Figure 6.4: Output power of rubidium front-end, the potassium front-end and the HMC evaluation kit over output frequency, the red marked zones indicate gaps in the possible output frequency of the HMC 834. The blue curve shows the results for the evaluation kit as reference. the green line shows the results for the rubidium variant and the red line for the potassium variant.

It should be noted that the splitter combiner for the potassium variant (GP2S1+ [51]) is only specified for 500 MHz to 2500 MHz exceeds its design specifications for lower and higher frequencies. The splitter combiner for the rubidium variant (GP2X1+ [52]) is specified for operation between 2800 MHz and 7200 MHz and is not suitable at frequencies below 2800 MHz.
For comparison with the HMC 834 evaluation kit, it is vital to take into account that the injection losses for the attanuators on the front-end and the losses from the splitter combiner are not present on the evaluation kit and no additional amplifier is present on the evaluation kit. The measured output power of the front-end matches the expectation of -11 dBm derived in 6.2.1, inside the area of the fundamental mode, where the two different splitter combiners have the widest area of overlap.

6.3.2 Spurious performance

The second important factor in this characterization is the spurious performance of the signal source. Spurious in general are signal peaks outside the target frequency. They occure inherited from the reference signal source, and from intermodulation between carriers and side bands. To judge the criticality of spurious with regard to the goal of using the signal for evaporation one has to consider separate cases:

- Spurious with $f_{spur} > f_{carrier}$: This spurious are not resonant with atoms in the evaporated ensemble, since while decreasing the evaporation end frequency they only pass through regions already evaporated by the carrier.
- Spurious with $f_{tb} < f_{spur} < f_{carrier}$: These spurious are directly resonant with atoms of an energy below the cut off frequency of the evaporation. Depending on the amplitude they can decrease the atom number, or lead to a new unintended lower limit for the cut off.
- Spurious with $f_{spur} < f_{carrier}$: Can potentially be ignored if $f_{spur} < f_{tb}$ holds for every step in the evaporation

were f_{tb} is the frequency difference between the the $m_f = 0$ and the $m_f = 2$ state (in case of rubidium 87).

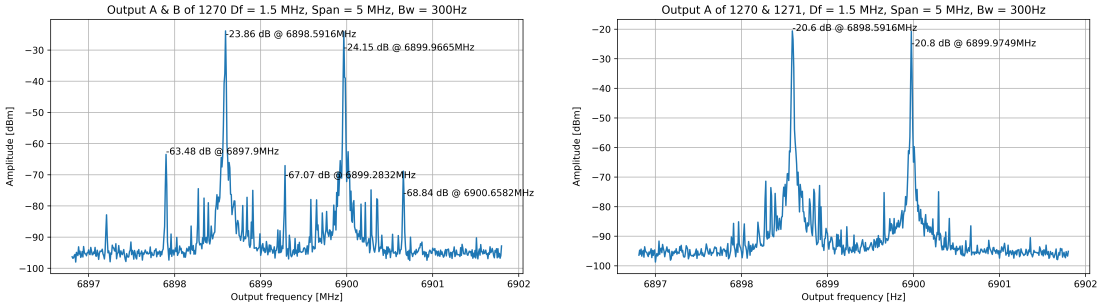

Figure 6.5: LHS: Output spectrum of front-end 1270 in dual channel mode of operation. Channel A is set to 6900 MHz and channel B is tuned 1.5 MHz below channel A via the reference. Side-band spurious can be observed at $f_{carrier} \pm (f_A - f_B)$ with amplitudes between -40 dBc and -44 dBc. Further side-bands can be observed at low frequency offsets from each carrier. RHS: Output spectrum of front-end 1270 and 1271 combined with an external splitter combiner of type GP2X1+. The output frequency of front-end A (Channel A) is 6900 MHz, the output of font end 1271 (Channel B) is set to 1.5 MHz below the output of front-end 1270. The third order harmonics of the fundamental mode of the HMC 834 observed in 6.5 (LHS) can not be observed.

Characterization of spurious of the evaporation signal source

To quantify the spurious performance of the source, the front-end with the series number 1270 is set to an output configuration with channel A on an output frequency of 6900 MHz and channel B of the same front-end set to 1.5 MHz below channel A, to see possible interference between both output channels, as well as side bands from the carrier. The result of this measurement is illustrated on the left hand side of figure 6.5. The measurements shows spuries with $f_{spur} = f_{carrier} \pm 500$ kHz with amplitudes below -50 dBc and strong spuries at $f_{carrier} \pm (f_A - f_B)/2$ at -40 dBc. Further measurements showed the $f_{carrier} \pm (f_A - f_B)/2$ spurs at matching positions for different separation frequencies. This indicates this spurs to be third order harmonics of the fundamental mode of the HMC 834. For typical cut off frequencies used for the rubidium evaporation in MAIUS-B the separation of the re-excitation- and evaporation signal is usually around 3 MHz. With this separation, the spuries at $f_{spur1} = f_A + (f_A - f_B)/2$ and $f_{spur2} = f_B - (f_A - f_B)/2$ are at frequencies of: $f_{spur1} = f_A + 1.5$ MHz and $f_B - 1.5$ MHz are outside the resonant areas. The third spuries at $f_{spur3} = f_A - 1.5$ MHz lies inside the resonant zone. However the remaining spuries are also inside the problematic area.
A test with the same configuration but with a single channel from the front-ends 1270 and 1271 set to matching frequencies of the later measurement, combined with an external splitter combiner of type GP2X1+, on front-end 1271 the serial communication was silenced during the test. These tests results are illustrated on the right hand side of figure 6.5. In this measurement, the third order harmonics of the fundamental mode of the HMC 834 can not be observed. The intermodulation thus only happens on a single board. The signal from front-end 1271 only showed two spurious at 240 kHz in this configuration. The missing spurious are caused by the serial communication and can be avoided by silencing the communication during experiments. The spurs at $f_{carrier} \pm 240$ kHz are inherited from the DDS card as a reference. From the measurement it is clear that the signal source can not be used in dual channel mode with the requirements for the MAIUS-B experiment.
However the system can be used in single channel mode with a fixed reference and mixing with a DDS-card signal. The resulting setup is described in section 6.4.
To characterize the behavior of intermodulation on a single front-end with both output channels active, the amplitude of the f_3 spur was measured for different separation frequencies. The results of this measurement can be found in appendix: A.5. The performance of the system in the dual channel mode with the described disturbance

present will be tested by creating a rubidium 87 BEC, in the measurement chapter.
Even though the system is not fit for the operation of MAIUS-B in its current state, the data presented in chapter 7 suggest that the creation of a cold atomic ensemble with a small BEC fraction of 36%, is possible using the system in dual channel mode, see chapter 7.
The source in its current state can already be used for miniaturized satellite missions for experiments with cold atomic ensembles but not in the BEC state. Since the data suggests that the intermodulation between the output channels is field coupled the next design step is to build the microwave front-end on a ceramic filled PTFE composites laminate to prevent the radiation of parts of the signal. To also suppress wire bound coupling the fundamental mode of the HMC 834 can be filtered between the PLL and the onboard amplifier in case of the rubidium variant. Besides the avoidance of intermodulation between the channel, a loop filter with a smaller band width can be tested to suppress spurious from a tunable source. These upgrades and the design of an RF compliant casing specifically made for the front-end can lead to a disturbance free variant of the front-end.

6.3.3 Phase noise

The third important parameter for this characterization is the phase noise performance of the microwave source. Phase noise is a representation for random fluctuations of the source in the frequency domain. It is often referred to as jitter. Jitter is the noise representation in the time domain.
For this characterization the single side band phase noise of a rubidium variant front-end is measured with a phase noise analyzer of type: "Rohde und Schwarz FSWP Phase Noise Analyzer 1 MHz - 8 GHz" [87]. The Phase noise measured with the 5 V supply of the front-end is connected to a $LiFePO_4$ 2-cell battery to avoid influence from the power supply and achieve conditions similar to the flight configuration. With respect to the results shown in the last section, the measurement is taken with only one output channel active. The measurement is shown in figure 6.6. The measured phase noise is -41.64 dBc between 1 Hz and 10 MHz. The point phase noise at a carrier offset frequency of 100 kHz is -95 dBC/Hz. The HMC 834 evaluation kit states a similar value at a carrier frequency of 5.6 GHz of -107 dBC/Hz. The phase noise will be discussed further in section 6.5. The phasenoise of the overall system that consists of signal source, reference oscillator and amplifiers, will be shown in section 6.5 after this system is derived in 6.4.

6.4 Design of the overall microwave system

The microwave system is the overall system used to provide the signal for the microwave evaporation. It includes the reference oscillator, the front-end acting as signal source, a mixer and a number of amplifiers.
The signal source presented in section 6.2 is designed to provide two independent output signals through one SMA output connector and uses the DDS card presented in section 5.2 as a tunable frequency reference. The output signal containing two carrier frequencies is than lead into one additional pre amplifier before being transmitted into the power amplifiers of the output stage. The overall microwave system planned with the signal source is illustrated in figure 6.7.
Considering the spurious performance measurements regarding the signal source, for the MAIUS-B experiment the front-end must be used in single channel mode with

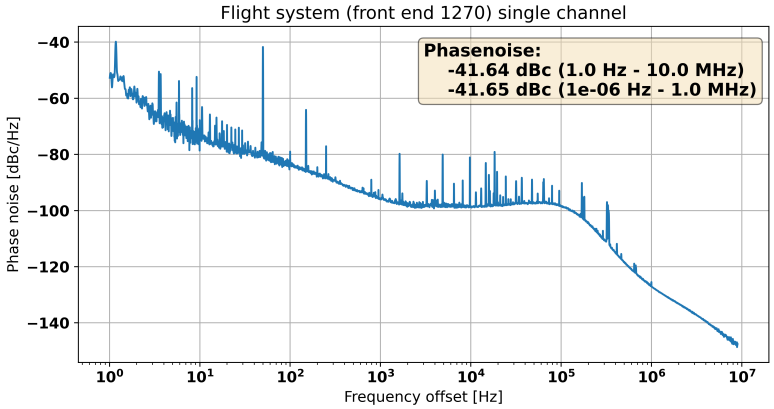

Figure 6.6: Single side band phase noise performance of front-end 1270 at an output frequency of 6900 MHz. VCO and Charge pump of the PLL has been supplied by a $LiFePO_4$ battery. The Phase noise is measured to be -41.64 dBc between 1 Hz and 10 MHz a strong spur is visible at 50 Hz due to the AC supply.

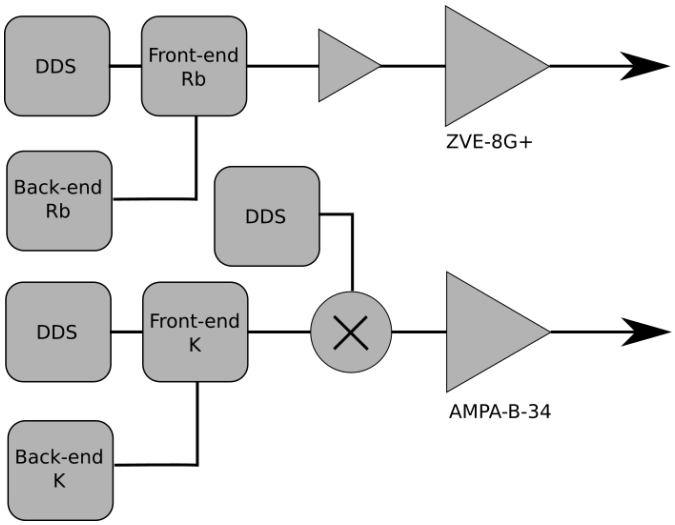

Figure 6.7: Schematic picture of the planned microwave evaporation system. One frontend per atomic species is used as a signal source, with the DDS card used as tunable reference.

an fixed reference. To ensure the criterium of tunability around the target frequency, mixing of the resulting microwave signal with an DDS signal is necessary.
Even tough this only shifts the injection point of the DDS side bands from the reference to a frequency mixer later in the signal chain, this mixed in DDS signal is not contributing to the overall noise in the same harmful way as it would when used as a reference. This is because the DDS side bands do not intermodulate with the carrier in the output stage amplifiers of the HMC 834. The mixing is realized with a Minicircuits ZMX-7GR frequency mixer for the rubidium frequencies and a Minicircuits ZX05-5-S+ frequency mixer for the potassium frequencies. However the phase noise of the DDS has a strong contribution to the overall phase noise. The phase noise of the DDS is shown appendix A.8. The need for the mixing of the output frequency increases the demand for power from the microwave source. Due to that demand two additional RF amplifiers are put in front of the frequency mixer. Two additional amplifier need to follow the mixer to fulfill the power criterium for the input power of the power amplifiers. For both variants amplifier of type Minicircuits ZX-60-183A-S+ [56] are used. Since the evaporation of potassium will be sympathetically, only one output frequency is necessary for potassium. A schematic picture of the MAIUS-B flight microwave system is shown on the right hand side of figure 6.8. The shown system is mounted within the physics package and electronic system sections of the payload like shown in section 5. The potassium signal source along with its amplifier and mixer chain is set up on the electronic system module to conserve space in the physics package section. The potassium system is the better candidate for a location further away from the physics package due to its lower operating frequency.
The characterization of the overall system in the following section will compare the microwave system described here to the MAIUS-B ground evaporation system. This system consists of HMC 834 evaluation kits (one kit per frequency) and a little microcontroller evaluation board of type Raspberry Pi. To set the target set points of the HMC 334 PLLs. The signal is then frequency mixed with a signal from a DDS card and amplified in the same way like in the flight system. A 20 MHz reference from an oven stabelized crystal oscillator is used as a reference for the ground system. A schematic picture of the ground system is illustrated on the left hand side in figure 6.8.

6.5 Characterisation of the overall evaporation system

In the flight configuration shown on the right hand side of figure 6.8, the phase noise of the microwave system is measured and compared to the phase noise of the MAIUS-B ground system shown on the left hand side of the same figure. The single side band phase noise of both system is measured by the "Rohde und Schwarz FSWP Phase Noise Analyzer 1 MHz - 8 GHz" [87], with both systems set to an output frequency of 6800 MHz. The results of this measurement with the ground system is shown in figure 6.9. The phase noise of the MAIUS-B ground evaporation system is used as a design goal for the flight evaporation system. The single side band phase noise of the flight evaporation system like described in this section is shown in figure 6.10. For the characterisation a Rohde und Schwarz SMC100A signal generator [71] was used as a frequency reference. During the flight an oven-stabilized crystal oscillator from the POF-switch will be used as frequency reference like described in section 5.4. A direct comparison of the single side band phase noise of the three different systems is shown in figure 6.11 in a combined plot. In this plot the ground system phase noise is shown in blue, the flight system in green and the DDS-card in red. This comparison shows that the phasenoise of the flight evaporation system fulfills the requirement. One can notice

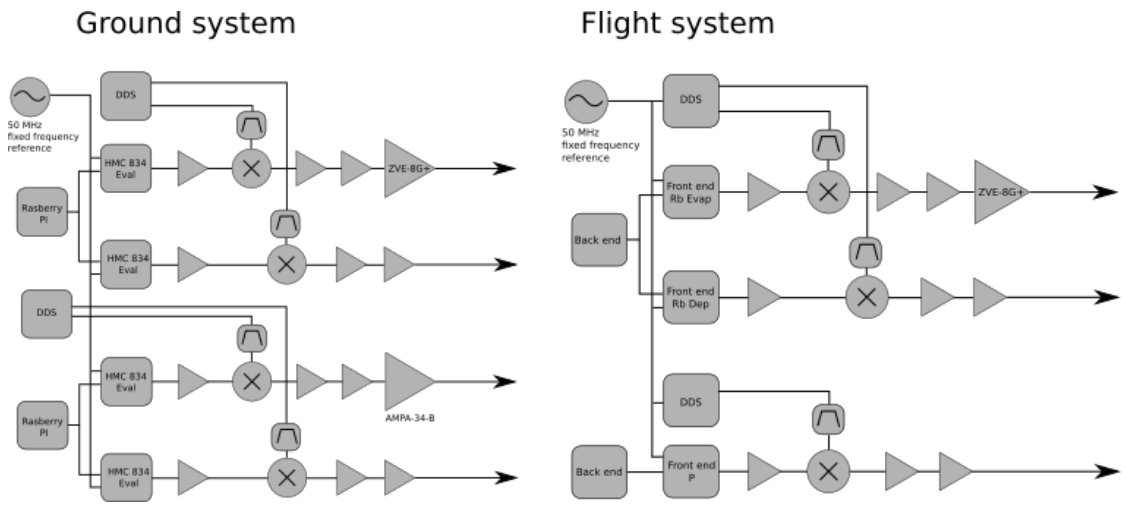

Figure 6.8: LHS: Schematic picture of the MAIUS-B ground microwave system. 4 HMC 834 evaluation kits are used to generate the evaporation signals. The setpoints are set by a raspberry pi micro controller evaluation board. The signals from the evaluation board are amplified by ZX-60-183A-S+ amplifiers and frequency mixed with band passed filtered signals from DDS cards. After the mixing the re-excitation signals pass two additional ZX-60-183A-S+ amplifiers while the evaporation signals also pass power amplifiers of type ZVE-8G+ for rubidium and AMPA-32-B for potassium. RHS:Schematic picture of the MAIUS-B flight microwave system. Two rubidium type front-ends are used in single channel mode to generate the evaporation signals needed for rubidium 87. A fixed frequency reference is used for optimal phase noise performance. The front-ends outputs are amplified with a ZX05-5-S+ amplifier and than mixed with a band pass filtered signal from a DDS card to create the necessary tuning range. Due to losses in the frequency mixer additional amplifiers are necessary. The evaporation signal additionally passes a power amplifier of type ZVE-8G+. The potassium evaporation signal is generated by the third front-end and processed in a similar way.

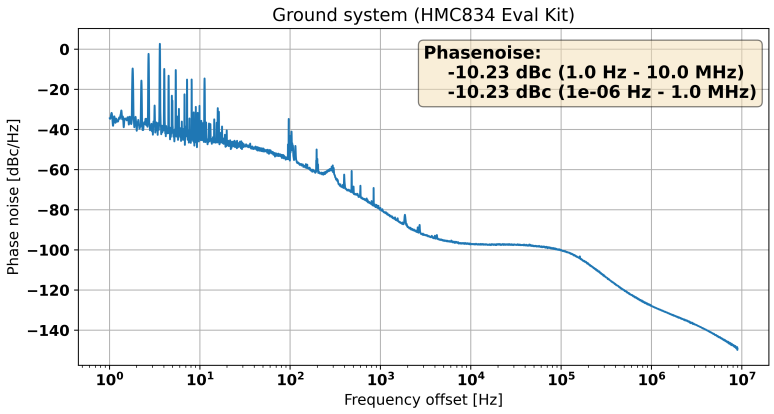

Figure 6.9: Single side band phase noise of the MAIUS-B ground evaporation system at an output frequency of 6900 MHz. The phasenoise is measured to be -10 dBc between 1 Hz and 10 MHz. This phase noise is used as a design goal for the MAIUS-B flight evaporation system.

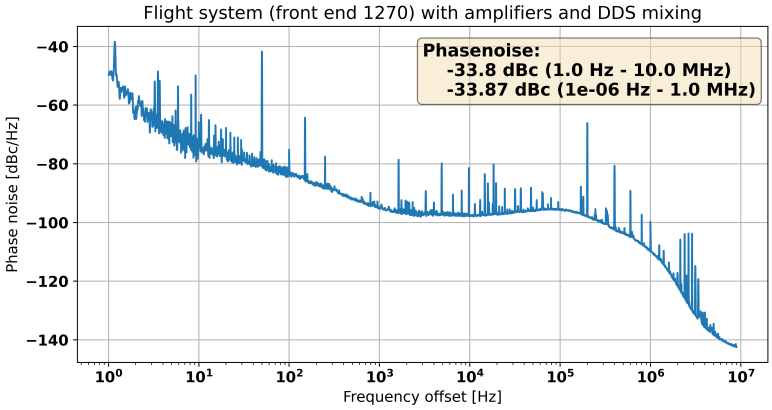

Figure 6.10: Single side band phase noise of the MAIUS-B flight evaporation system at an output frequency of 6900 MHz. The phasenoise is measured to be -33.8 dBc between 1 Hz and 10 MHz.

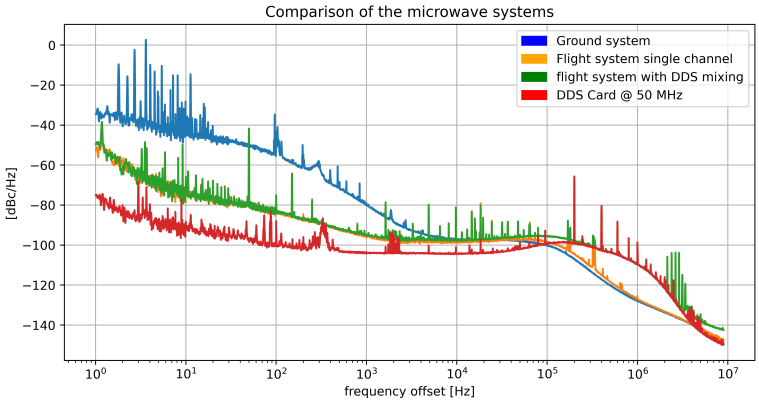

Figure 6.11: Single side band phase noise comparison of the MAIUS-B ground and flight system, the DDS-card and the phase noise of a single front-end.

strong inheritance of phasenoise from the DDS card in the higher frequencies of the flight system.

CHAPTER 7

Measurements and discussion of results

This chapter will present measurements with the MAIUS-B experiment. The first section shows measurements regarding the chip and coil current drivers. These measurements include test of the loss and heating rates from a trapped ultra cold atomic ensembles, described in chapter 4.1. Using these measurements a requirement catalog for the noise performance of future developments can be created.
The second section shows phase transitions of a rubidium-87 BEC, created using the three different microwave evaporation systems described in chapter 6.5.
While the characterization phase noise and spurious performance shown in chapter 6.5 is a good way compare the systems, a test of the performance in BEC creation is necessary.
This is because the design goal for the flight microwave system is to reach the same performance as the ground microwave system. This design goal is tested by the direct comparison of the phase transitions using the ground and the flight microwave system. A discussion of the results will follow each section in this chapter.

7.1 Chip and coil current drivers

In this section the experimental results regarding the chip and coil current driver are shown. Following the discussion in section 4 the sensitivity of the atomic ensemble against noise around the Lamor frequency and the trap frequency is investigated. This investigation contains the measurement of loss rates from the trap for a fixed disturbance amplitude and for a fixed disturbance frequency.
Additionally heating rates at the trap frequency for different noise amplitudes will be characterized and compared to the literature. The effect of a fixed amplitude disturbance for a variable offset frequency from the trap frequency will also be measured.
To investigate loss and heating rates the science chip Z-structure of the MAIUS-B experiment was connected to the current driver via the cable shown in appendix B.55. This cable can couple in a disturbance into the current supply to the atom chip over a 510 Ohm resistor. A RIGOL DG 1022 signal generator [70] was used to create a controlled disturbance, for all of the following measurements. The current offset caused by this signal generator over the 510 Ohm can be calculated using Ohms law. Due to the low frequencies necessary for investigations around the trap frequency, an AC-couppling of the disturbance is not practical.
The current driver used for this measurements is well characterized (including its noise spectrum) in [65]. The current driver used in the MAIUS-B flight system is based on this model, but modified in output current resolution and setup of the output stage. The changes of the new current driver version are summarized in section 5.9. Both versions

of the current driver have identical analog control loops.
For the following measurements the experimental setup described in chapter 3 was set up in the ground test bed environment. The three layers of magnetic shielding have been disassembled to improve accessibility. The experiment is tilted by 90 degrees leading to a configuration with gravity pointing alongside the atom chip surface.

7.1.1 Heating at the trap frequency

To investigate the sensitivity of the experiment against disturbances around the trap frequency, two measurements are performed.
For both measurements a disturbance is coupled into the scientific Z-structures supply current using the cable shown in B.55. The amplitude of the disturbance is set to 1 V peak to peak and the disturbance frequency is incrementally ramped up in steps of 0.25 Hz. For every step a cloud of could atoms is prepared with the MAIUS-B experiment. The evaporation of the cold atomic cloud is stopped after the eighth evaporation ramp with a cut of frequency of 6840.39 MHz. After the evaporation the ensemble is transported further away from the atom chip surface by increasing the Y-Coil current in 500 ms from initially -0.9 A to -2 A, leading to a distance of the trap minimum to the atom chip of 566 μm. The transport away from the atom chip surface is necessary to minimize the rate of three body collisions in the less steep trap at the position of the new trap minimum. After the transport, the initial state of the magnetic trap for the following experiment is reached and the ensemble has a temperature of 1.3 μK with $4{\cdot}10^6$ atoms in the trap.
In the first measurement the effect of the disturbance is tested by taking 5 time of flight measurements with the prepared ensemble between 10 ms and 30 ms to obtain the expansion rate of the ensemble. This measurement is than repeated for holding times of the ensemble in the trap of 500 ms and no holding time in the trap. Disturbances of the trap current in the region of the trap frequency can only effect the atomic ensemble while it is interacting with the trap. Thus the measurement without a holding time will function as a reference for the expansion rate without a disturbance. From the expansion rate measured in the measurement for 500 ms holding time the heating rate for every individual disturbance frequency can be calculated. Since the heating is measured for two different holding times, the heating rate can be calculated with a linear approximation.
The trap frequencies of the MAIUS-B experiment and the current parameters are simulated before hand to be 24 Hz, 136 Hz and 133.8 Hz using a simulation tool. An investigation around 24 Hz is not possible for the RIGOL DG 1022 signal generator. Thus the scan of the disturbance frequency is started at 120 Hz. One should note that in order to simulate current driver noise as realistic as possible the disturbance is also present during the evaporation phase.
The results of this measurement are shown in figure 7.1. The data shows a resonance with a heating rate of 1.4 μK/s at a disturbance frequency of 126 Hz. The frequency of this resonance differs from the trap frequency predicted by the simulation tool. This difference is due to influence of the magnetic field of the earth on the experiment in the absence of the magnetic shielding. Resonances are visible at 126 Hz and 127 Hz. The blue data points represent the temperature in x-direction and the orange points in y-direction.
In the second measurement the resonance found in figure 7.1 is now investigated for different amplitudes of the disturbance. With the same experimental setup and the same initial trap configuration, the disturbance frequency is now set to fixed frequency

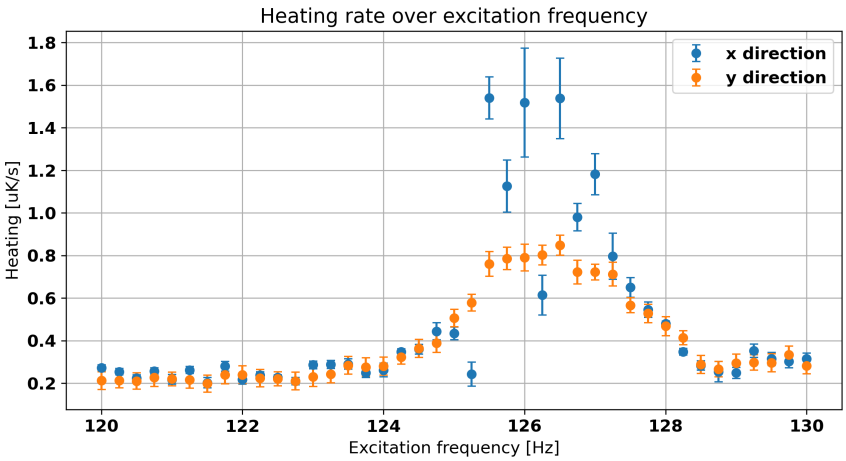

Figure 7.1: Measurement of the heating rate of the atomic ensemble against the disturbance frequency. The disturbance was coupled in with an amplitude of 1 Vpp with the cable described in B.55. The heating rate was measured by taking 5 time of flight measurements with the prepared ensemble between 10 ms and 30 ms. This measurement is than repeated for holding times of the ensemble in the trap of 500 ms and no holding time in the trap, to calculate a heating rate per second. The disturbance is also present during the evaporation. The deformations of the signal visible at 126 Hz and 127 Hz match the calculated trap frequencies. The blue data points represent the temperature in x-direction and the orange points in y-direction.

of 126 Hz. With this frequency the temperature is measured again with a five point time of flight measurement (10 ms-30 ms) for a holding time of 500 ms and no holding time in the magnetic trap. The amplitude of the disturbance is increased from 0 Vpp to 2 Vpp in 11 steps. The results are shown in 7.2.
The plot shows the measured heating rate in x direction (blue) and in y direction (orange). The green line indicates the theoretical values generated with equation 4.15 multiplied by the transferred energy per excitation and converted to temperature by equation 3.14.

7.1.2 Off-resonant excitation of heating

To create a design reference for the noise of new current driver developments the heating is also tested for several off resonant frequencies. The measurement was taken for 100 kHz, 500 kHz, 1000 kHz, 1500 kHz and 5000 kHz. For each frequency a disturbance was coupled in with 5 Vpp and 10 Vpp. The temperature was measured again with a time of flight measurement (10 ms-30 ms) for a holding times of 0 ms and 500 ms. From the raw data the heating rate per Vpp was calculated by a linear fit through the heating rates for different excitation amplitudes. The data is shown in 7.3. During the measurement the disturbance was triggered by the experimental timing system to be present only during the holding time in the trap. This is necessary because for frequencies above 1.4 MHz the disturbance would excite transitions between the $m_f = 0$ and $m_f = 2$ states. This leads to radio evaporation. The effect of atom losses due to radio evaporation and losses due to excitation at the Lamor frequency can not be separated in this case.
The loss rate corresponding to the radio evaporation was measured intentionally with a scan of the disturbance frequency from 1 MHz to 2 MHz in 21 steps with a disturbance amplitude of 2 Vpp. An additional measurement of the radio evaporation due to noise in the chip wire was taken for disturbance frequencies between 1 MHz to 20 MHz

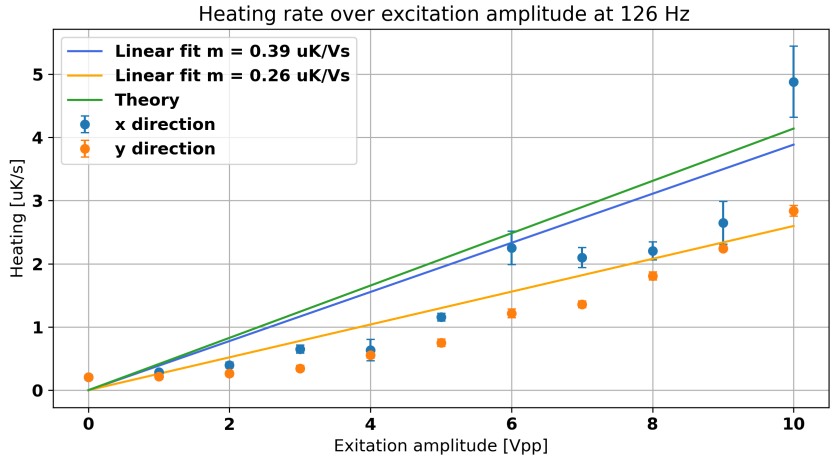

Figure 7.2: Measurement of the temperature of the atomic ensemble at the trap frequency of 126 Hz for an amplitude ramp from 0 Vpp to 2 Vpp in 11 steps. The heating rate was measured by taking 5 time of flight measurements with the prepared ensemble between 10 ms and 30 ms. This measurement is than repeated for holding times of the ensemble in the trap of 500 ms and no holding time in the trap, to calculate a heating rate per second. The blue data points represent the temperature in x-direction and the orange points in y-direction. The green line represents equation 4.15.

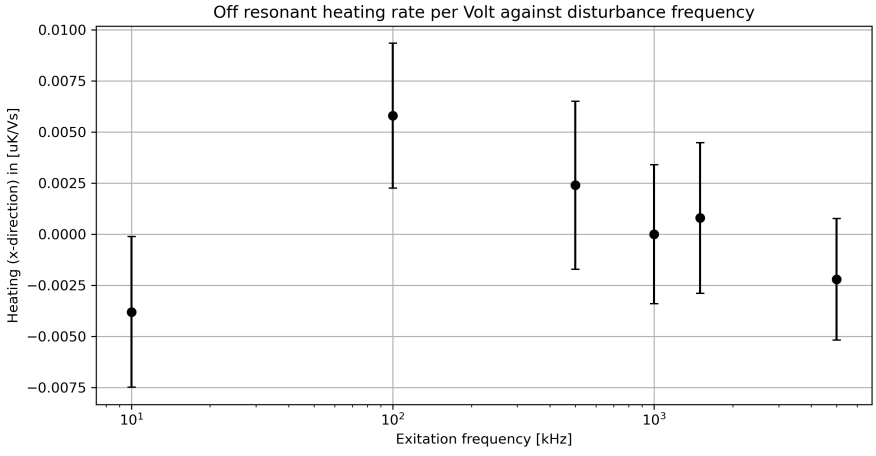

Figure 7.3: Attempted excitation of heating for off-resonant frequencies. The rates in $\mu K/Vs$ are calculated by a linear fit through the data of every set of raw data. The raw data is the attempted excitation of heating for 3 different disturbance amplitudes per frequency. During the measurement the disturbance was triggered to be present only after the last evaporation step, to avoid radio-evaporation at disturbance frequencies over 1.4 MHz

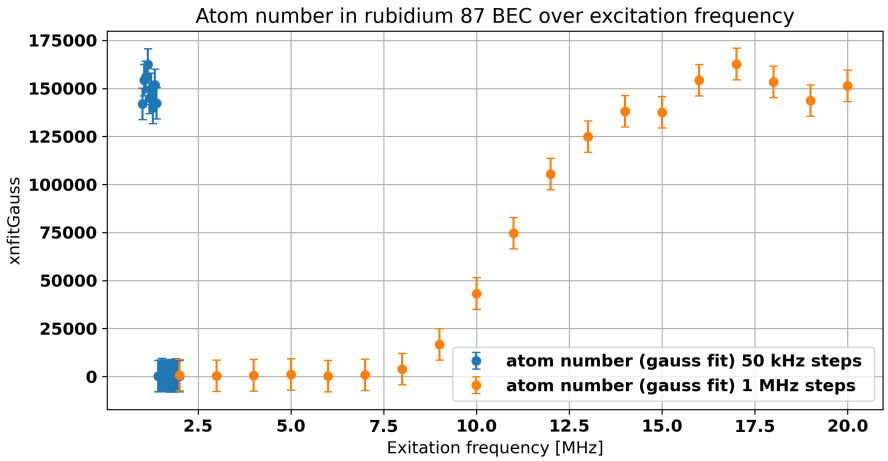

Figure 7.4: Atom losses over disturbance frequency above 1.4 MHz. For disturbance frequencies over 1.4 MHz all the atoms in the BEC are lost due to radio evaporation. For disturbance frequencies over 7.5 MHz the atom number in the BEC increases again in a softer slope due to the Boltzmann distribution of the atoms in the trap. The lower limit of 1.4 MHz is the energy difference between the $m_f = 0$ and the $m_f = 2$ state in the magnetic field of the trap.

in 21 steps. The measurements were taken with the same experimental setup and trap configuration like the previous measurement. The combined results are shown in figure 7.4. For disturbance frequencies over 1.4 MHz all atoms are evaporated from the trap. The lower limit of 1.4 MHz is the energy difference between the $m_f = 0$ and the $m_f = 2$ state in the magnetic field of the trap. For disturbance frequencies above 7.5 MHz the atom number in the BEC increases again. The slope of the atom number increase over disturbance frequency is due to the Bolzmann distribution of the atoms in the trap.

7.1.3 Atom losses around the Lamor frequency

To investigate the sensitivity of the experiment against disturbances close to the Larmor frequency an ensemble of cold rubidium 87 atoms, created with the MAIUS-B experiment was disturbed in the trap. The disturbance was triggered to be present only after the last evaporation step, to avoid radio-evaporation at disturbance frequencies over 1.4 MHz. Again the evaporation of the ensemble was stopped after the eighth evaporation ramp and the atoms transported to a position 566 μm away from the atom chips surface. The resulting ensemble of cold rubidium atoms reached a temperature of of 1.3 μK with $4{\cdot}10^6$ atoms in the trap.
With these starting conditions, a disturbance created with a RIGOL DG 1022 signal generator was coupled into the science chip Z-structure with the cable described in B.55. The atom number in the cold atomic ensemble was measured for 21 disturbance frequencies between 2.1 MHz and 2.5 MHz with a disturbance amplitude of 5 Vpp. The results of this measurement are shown in figure 7.5. A minimum in the number of remaining atoms in the trap is visible for a disturbance frequency of 2.24 MHz.
Again the sensitivity is tested with a disturbance frequency on the resonance for 21 different disturbance amplitudes between 0 Vpp and 1 Vpp. For every excitation frequency the atom number in the cold atomic ensemble was measured for a holding time in the trap of 0 ms and 100 ms to calculate a loss rate. The experimental setup and trap configuration remained the same as in the previous measurement. The results are shown in figure 7.6.

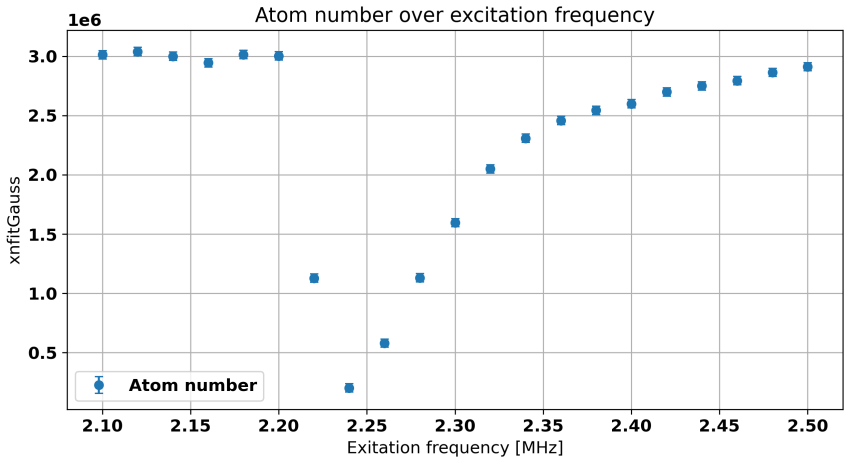

Figure 7.5: Atom losses from an ensemble of cold rubidium atoms over disturbance frequency with a fixed disturbance amplitude of 5 Vpp. The disturbance was triggered to be present only after the last evaporation step, to avoid radio-evaporation at disturbance frequencies over 1.4 MHz A minimum is visible at the Lamor frequency at 2.24 MHz

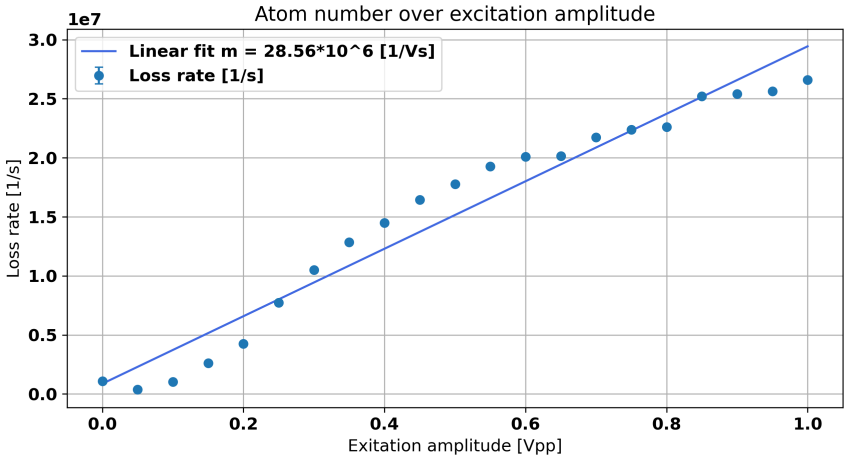

Figure 7.6: Atom losses for a fixed disturbance frequency of 2.24 MHz for different disturbance amplitudes. The atom number in the cloud of cold rubidium atoms was measured for 0 ms and 100 ms of holding time in the trap to calculate a loss rate.

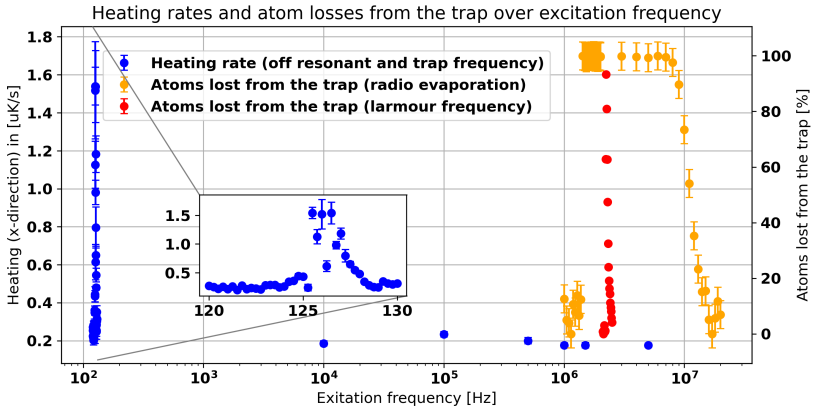

Figure 7.7: zones of heating and atom losses over disturbance frequency. The losses due to the radio evaporation are only present for disturbances that are present during the holding time in the trap. The inset shows a zoom around the trap frequency.

7.1.4 Discussion of results regarding the chip and coil current driver

The measurement of the heating rate at the trap frequency (figure 7.1) showed a maximum heating rate of 1.5 μK/s at an excitation frequency of 125.5 Hz and an excitation amplitude of 1 Vpp in x direction. Heating was also observed in y direction but with a lesser rate of 0.8 μK/s. The weak y direction is also heated by excitation of the x direction since the field in this direction is a mixture from the strong and weak axis. The effect of heating was observable between 124 Hz and 127 Hz. For common mode disturbances in the chip wires heating is also expected at twice the trap frequency like explained in chapter 4.
The heating rate on the trap frequency for a variable disturbance amplitude was measured to be 0.39 μK/Vs in the stronger x-direction.
At the off resonant frequencies of 100 kHz, 500 kHz, 1000 kHz, 1500 kHz and 5000 kHz no significant heating or losses cold be observed for excitation amplitudes up to 10 Vpp.
For disturbances at the Lamor frequency the loss rate was measured to be 28.56×10^6 1/Vs. This effect is only measurable for disturbances that are not present during the evaporation phase. Disturbances present during the evaporation phase showed radio evaporation over 1.4 MHz.
The data collected from the measurements represents a design guideline for the development of future electronic components for experiments with ultra-cold atoms. The data is illustrated in a combined plot that shows the zones of heating and atom losses over disturbance frequency in figure 7.7. In the figure the atom losses are normalized to the maximum number of atoms at the beginning of the measurement.
The losses due to the radio evaporation are only present for disturbances that are present during the holding time in the trap. One can see that electric noise between the trap frequency and the beginning of the radio evaporation has no harmful effect on the atomic ensemble. The effect of evaporation due to disturbance in the current drivers output can potentially be exploited for future current driver developments.
A current driver with a tunable RF-source on the same PCB can be used for radio evaporation. The results also show that external antennas are not needed in the MAIUS-B experiment.

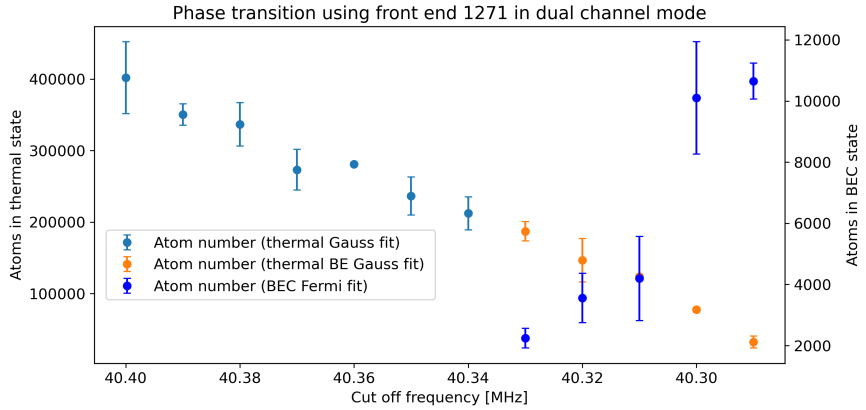

Figure 7.8: Phase transition of a rubidium 87 BEC using front-end 1271 in dual channel mode, with channel A fix at 6800 MHz and channel B used for the evaporation. The plot shows the thermal part calculated by a Gauss fit before the phase transition (light blue points), the thermal part after the phase transition calculated by a BE Gauss (orange points) and the BEC part calculated using a Thomas Fermi fit (blue points). The BEC fraction reached with this system is 84.9% with a total number of 12.5 $\cdot 10^3$ atoms in the trap.

7.2 The microwave evaporation system

The phase noise and spurious performance of the dual channel, the flight and the ground microwave system have been characterized in chapter 6.5. To translate these values to performance with the experiment further measurements with the experimental apparatus are necessary.
To quantify the performance of the microwave systems regarding the fitness for application in the experiment a rubidium BEC has been created with every system and the phase transition to the BEC state was investigated. For the performance test with the dual channel setup described in section 6.5 front-end with the series number 1271 has been used with channel A fixed on 6800 MHz and channel B used to evaporate down from 6900 MHz. After the eighth evaporation cycle the phase transition occurred in the final evaporation ramp down from 6840.4 MHz at a cut-of frequency of 6840.33 MHz. Absorption images are taken during this ramp in 21 steps to calculate the number of atoms in the thermal and the BEC state. The atom number in the thermal state before the phase transition (images 1-7) has been calculated using a Gauss fit. The atom numbers in BEC and thermal state after image 7 have been calculated using a BE Gauss fit for the thermal part and Thomas Fermi fit for the BEC part. The data is illustrated in figure 7.8. The dual channel operation of front reaches a BEC fraction of 84.9% with a total number of 12.5 $\cdot 10^3$ atoms in the trap. The evaporation started with initially $0.376 \cdot 10^6$ atoms in the magnetic trap.
The same measurement is performed with the ground microwave system. The results are illustrated in figure 7.9. With the ground system a BEC fraction of 99.1% was reached with a total number of 252.9 $\cdot 10^3$ atoms in the trap. The evaporation started with $2.6 \cdot 10^6$ atoms in the magnetic trap.
To translate the phase noise and spurious performance of the dual channel, the flight and the ground microwave system into performance with the experiment, the phase transitions of a rubidium 87 BEC has been investigated.
The performance of the ground system is the acceptance criteria for the flight system. By comparing the results of the ground system and the dual channel operation of front-end 1270 it becomes clear that even though a BEC was created with the dual channel operation, the performance of the dual channel operation does not fit the needs of the

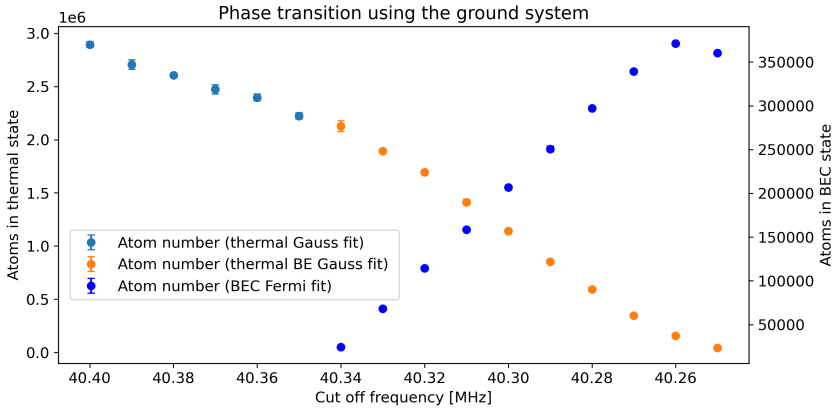

Figure 7.9: Phase transition of a rubidium 87 BEC using the MAIUS-B ground system described in section 6.5. The plot shows the thermal part calculated by a Gauss fit before the phase transition (light blue points), the thermal part after the phase transition calculated by a Bose enhanced Gauss (orange points) and the BEC part calculated using a Thomas Fermi fit (blue points). The BEC fraction reached with this system is 99.1% with a total number of $252.9 \cdot 10^3$ atoms in the trap.

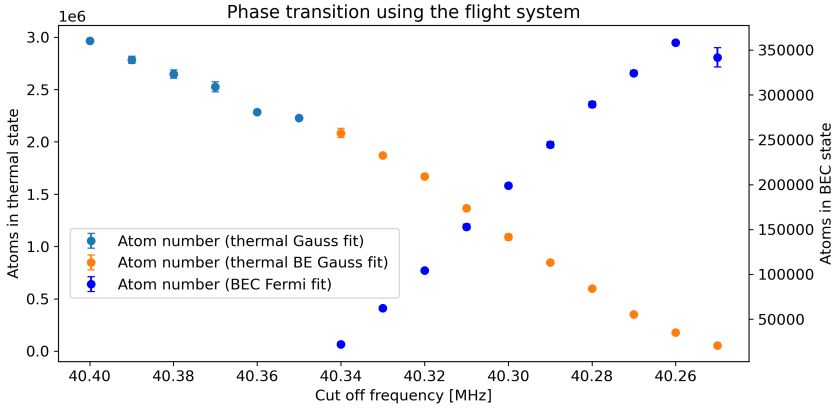

Figure 7.10: Phase transition of a rubidium 87 BEC using the MAIUS-B flight system described in section 6.5. The plot shows the thermal part calculated by a Gauss fit before the phase transition (light blue points), the thermal part after the phase transition calculated by a BE Gauss (orange points) and the BEC part calculated using a Thomas Fermi fit (blue points). The BEC fraction reached with this system is 99.8% with a total number of $252.6 \cdot 10^3$ atoms in the trap.

experiment.
One has to consider that the phasenoise of the dual channel system with −40.64 dBc between 1 Hz and 10 MHz is lower than the measured phase noise of the ground system with −10.23 dBc between 1 Hz and 10 MHz. This result shows that spurious of the microwave source are the major factor to consider regarding the evaporation performance. Further investigations of this topic are proposed in section 8.
To compare the ground microwave system with the flight configuration derived in 6.5, the measurement was repeated using the flight system. The results are illustrated in figure 7.10. With the flight system a BEC fraction of 99.8% was reached with a total number of $252.6 \cdot 10^3$ atoms in the trap. The evaporation started with $2.62 \cdot 10^6$ atoms in the magnetic trap.

7.2.1 Discussion of results regarding the microwave system

The design goal for the the flight microwave evaporation system is the performance of the ground microwave system. With the ground microwave system a BEC with a BEC fractionof 99.1% with a total number of $252.9 \cdot 10^3$ atoms in the trap is reached. The flight system presented in chapter 6.5 reached a BEC fraction of 99.8% with a total number of $252.6 \cdot 10^3$ atoms in the trap. This performance matches the design goal and the system can be used for the flight operation.
The BEC created with the dual channel operation mode of the microwave front-end reached a BEC fraction of 84.9% with a total number of $12.5 \cdot 10^3$ atoms in the trap. Even though this performance does not match the requirement for the flight operation, the system is able to evaporate to the BEC state while being half the size of the flight system. This measurement shows the general feasibility of the dual channel mode of operation.
The low performance of the dual channel mode of operation is caused by spurious between the two output carriers. The source of these harmful spurious is the intermodulation between the two output channels. In a future development the design can be improved by using a Roger PCB, a specialized casing and a careful separation of grounds on the PCB.

CHAPTER 8

Outlook

This work presented the electronic system of the MAIUS-B experiment. This electronic system is able to autonomously control a dual species atom interferometer in space while being of roughly the same size and mass as its predecessor in the MAIUS-A experiment, even though electronics for a second atomic species had to fit in.

To achieve this miniaturized electronics for the power supply, the microwave evaporation system and the current driver had to be created, that are described in detail in this thesis.
The overall electronic system is structured in 3 modules: The battery module with a mass of 18.1 kg and a total hight of only 170 mm, the laser electronic module with a mass of 34.6 kg and a total length of 531 mm and the electronic module with a mass of 31.2 kg and a total hight of 400 mm.
The electronics modules have an average power consumption of 753 W. The power is supplied by a main battery module complemented by two extra batteries for galvanically isolated components like the current drivers and the microwave system. The whole system can operate for 40 min.

Key parameters for the design of electronic systems for future missions with atom interferometers in space have been derived from the underlying theory, the challenges of operation in space and by tests of the experiment. One of these tests was the measurement of the sensivity of the experimental setup against electric disturbances, by the controlled coupling of disturbing signals into the atom chip wire that forms the trap. This way the sensivity has been investigated for different amplitudes and disturbance frequencies around the trap and the Lamor frequency. By adding measurements of heating rates in off resonant zones, a catalog of design parameters for the maximum allowed noise spectrum for future components has been created.
These upper limits not only apply for future current driver developments but for all kind of future developments, since a disturbance can have its origin anywhere in the system. The current driver was only chosen to carry out this investigation since it allows the most direct access to the trapped atomic ensemble.
The data also showed that a future design of a chip and coil current driver can be build to exploit generated disturbances to radio evaporate rubidium 87. This new feature could lead to the next step in miniaturization by the future development of a current driver that can also replace the evaporation system.
The results also show that the use of switching regulators for the chip and coil current drivers is possible if the selected switching regulator produces noise only in the non-resonant zones found in the measurements. The use of switching regulators can potentially lead to a further miniaturization of future apparatuses, due to the potential saving of power compared to linear regulators. This saving of power can also decrease

the overall size of an apparatus since power is always associated with thermal mass and heavy batteries.
Besides the sensitivity for electric noise, the spurious and phase noise performance of the microwave evaporation system, that was developed in this work was characterized. Furthermore the effect of spurious noise in the microwave evaporation system was investigated by comparing the BEC-fraction of a BEC created with a noisy source with a BEC created with a quiet source. Even though this measurement showed that a miniaturized microwave source with a ultra wide frequency range between 250 MHz and 7 GHz poses more challenges than expected when it is supposed to have two output channels on the same board, it also layed the foundation for future improvements of this system. By identifying the source of harmful spurious noises and tracking them down to a field coupled disturbance between the two channels, it was shown that the general concept of the dual channel application works and the system can be modified to be used in future missions.
This is of great importance since already planned future missions like the BECCAL experiment on the International Space Station have an even higher demand for miniaturization, low noise and power conservative designs.
Some work has to be done on the electromagnetic compatibility of the microwave front-end board to reach a disturbance free operation of both channels. A first step in this direction would be to apply additional filtering to the design and build the front-end on a Roger PCB. A characterization of this new version can reveal a component fit for the requirements of the BECCAL mission.
For applications on the ISS a supercap based power supply module would be favorable due to its high reliability, its chemical free working principle, its inherent low noise and its highly dynamic capability of very fast charging and discharging for burst operation during one experimental cycle.

An ISS experiment with ultra cold atomic ensembles like BECCAL leads to a very complex apparatus. This complexity arises from the mission goal to be a multi user facility with very high atom numbers and long interferometer sequences with short cycle times.
With relaxed requirements on atom number and cycle time of such an experiment simpler methods for the generation of the light and electromagnetic fields become possible, significantly reducing also the amount of necessary electronics.
A miniaturized electronic systems similar to the one shown in this thesis could be used to realize an alternative kind of experiment on a very small free flying laboratory like a CubeSat satellite.
On a CubeSat a one cell $LiFePO_4$ supply would be favored, due to its intrinsic capability to drive 3.3 V systems without voltage regulators and with no need for complex battery management systems and its high energy density that can allow a long operation time after a charging phase over the solar panels.
For the use on a CubeSat the presented electronic system would have to be redesigned again to a different form factor and to work with only such a 3.3 V power supply. But the step presented in this work from 7 down to 2 supply voltages is already a big step in this direction, with the bulk of the TBus electronics already being 3.3 V supplied.
A miniaturized electronic system based on concepts shown in this thesis could be used to realize a CubeSat experiment. Possible scientific goals for CubeSat missions in the described regime of complexity vary with the number of CubeSat units used (from one to six).
A one unit CubeSat could demonstrate the possibility of a miniaturized grating MOT

on an orbital platform using the concept of the shown current drivers and an ultra high vacuum generated by the wake shield principle [18]. For such a demonstration the laser system needs to be simplified to the use of only one DFB-laser generating a grating MOT.
Adding the concept of the microwave system shown in chapter 6.5 and the coil current driver shown in chapter 5.9 a magnetic trap and evaporation could be achieved in a two unit CubeSat.
By adding an additional dedicated interferometry laser, a single species atom interferometer could be realized in a three unit CubeSat. The dedicated laser would be necessary for the higher demands to frequency stabilization of the interferometry laser compared to the MOT beams.
The next standard CubeSat size after the three unit is the six unit satellite (2×3). With the additional three units, a dual species atom interferometer could be realized by doubling the three unit system.

Building up on the design parameter catalog created in this work additional measurements can be proposed after the experiences in this work. Once the microwave system provides a clean dual channel mode, the exact influence of disturbing microwave frequencies with a known offset from the evaporation or re-excitation signal can be measured. This way the exact limit for spurious noise performance and phase noise of a microwave source for evaporation could be investigated with the MAIUS-B experiment.
Also measurements of the power supply suppression ratio of the microwave source and the current drivers can lead to new design parameters. Knowing these values exactly can complement the work done in this thesis by simply using the ratio to calculate the effect of a noisy power supply on the output of for example the current driver and thus the effect on the atomic ensemble.

The electronic system presented in this work is a milestone in the miniaturisation of electronic systems for atom interferometers on space born platforms. It enables the use of such a device on the international space station and is a leap towards the application of an atom interferometer on a free flying platform. It also is the foundation of possible Cube Sat experiments with cold atoms in space.

APPENDIX A

Supplementary data and graphs

A.1 Overview of electronic module specifications

Module	Power	Length	Mass
BAT	1 W	170 mm	18.1 kg
LE	379 W	531 mm	34.6 kg
EL	174 W	400 mm	31.2 kg
Total	753 W	1101 mm	83.9 kg

Table A.1: Overview of module specifications. The power is estimated in rms. The mass is calculated by the design software

A.2 Connection pattern of the atom chip

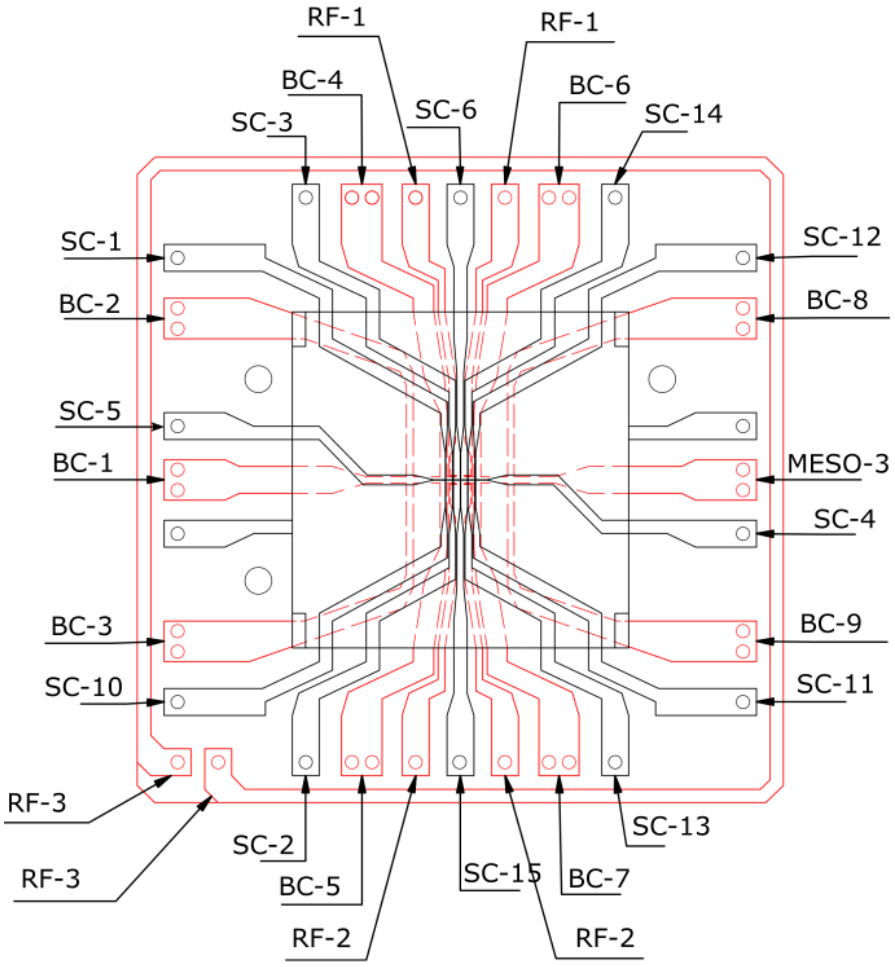

Figure A.1: Connection pattern of the MAIUS-B atom chip

A.3 Vibrational loads

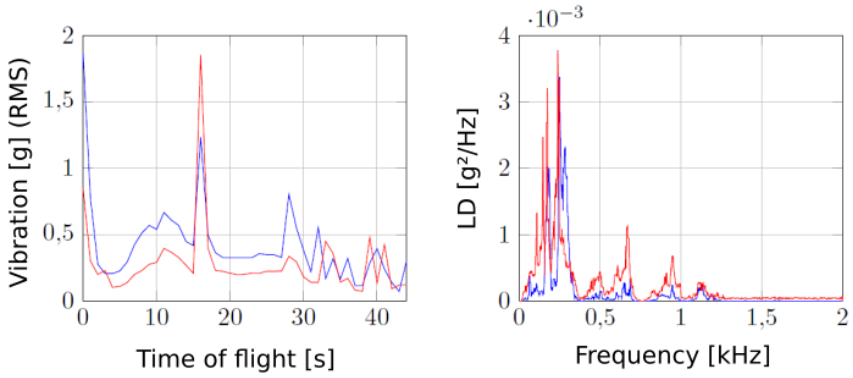

Figure A.2: Left hand side: RMS of the vibrations during flight in 1 s increments. The blue curve is showing the longitudinal accelerations, the red curve is showing the lateral accelerations. Right hand side: Power density in longitudinal direction. The blue curve is showing the power density at T = 12 s, the red curve at T=28 s. Both graphs unchanged from [79]

A.4 Shaker test results

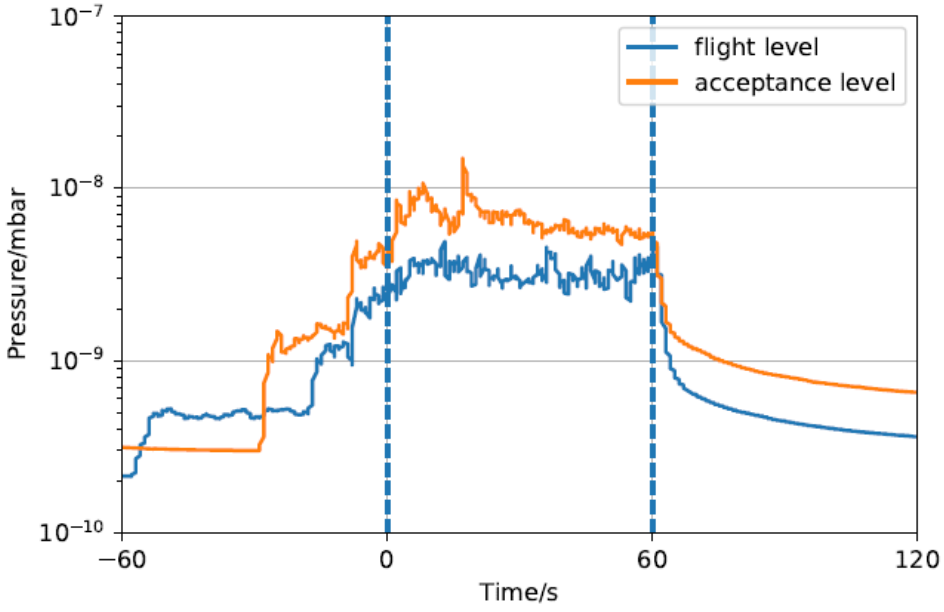

Figure A.3: Exemplary results of the vibrational test of the vacuum chamber in z direction. Shown is the pressure measured in the pumping system during and after the vibrational test. The RMS value of the acceleration is at 2 g (flight level) and 5.4 g (acceptance level). The vibrational tests of the other directions surpass the performance of the z direction. The signal before 0 s is due to a multistage increase of the vibration intensity until the target value is reached. Picture taken unchanged from: [8].

A.5 Charging of the two cell extra battery

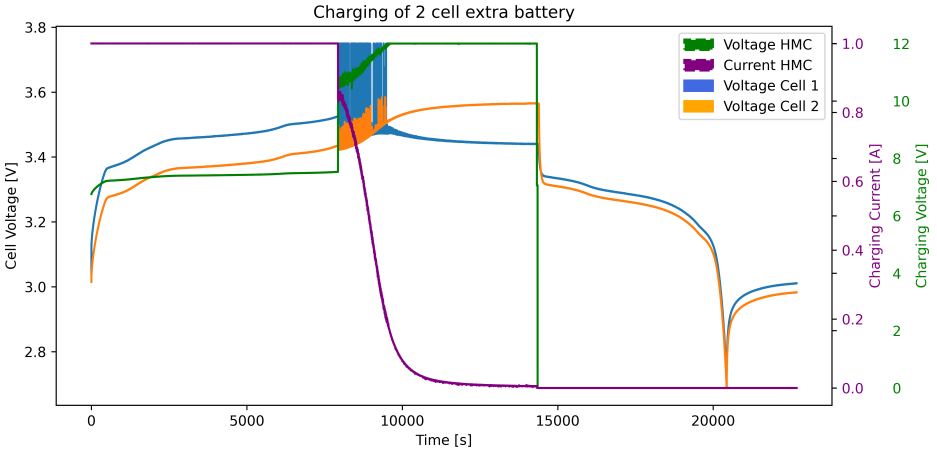

Figure A.4: Charging of the 2 cell extra batteries.

A.6 Additional measurements

A.6.1 Plot of the f_3 spurious behavior

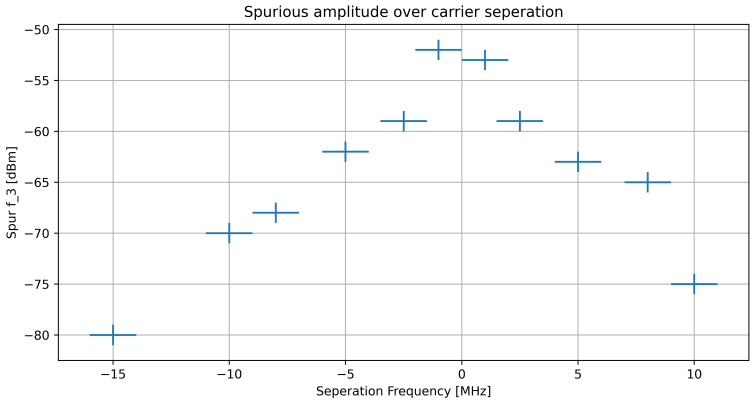

Figure A.5: Spurious amplitude over carrier separation. The measurement taken with both channels from front-end 1270 fits the theory of a third order harmonic.

A.7 Design specifications of the TBus

A.7.1 mechanical specifications

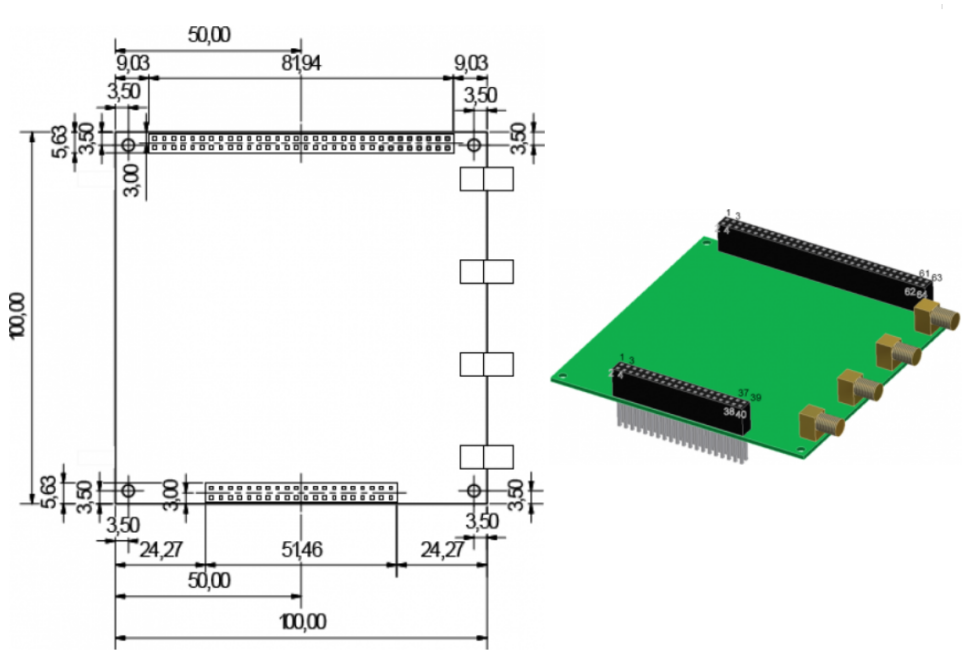

Figure A.6: Mechanical design of TBus cards. The Picture shows the mechanical drawing (left) and an Illustration from the design software [84].

A.7.2 Pin configuration of the Analog TBus PC104 connectors

Analog Connector:

Pin	Direction	Function	Pin	Power	Function
1	Power	Ground	2	Power	Ground
3	Power		4	Power	
5	Power		6	Power	
7	Power		8	Power	
9	Power		10	Power	
11	Power	Ground	12	Power	Ground
13	Power		14	Power	
15	Power		16	Power	
17	Power		18	Power	
19	Power		20	Power	
21	Power		22	Power	
23	Power		24	Power	
25	Power		26	Power	
27	Power		28	Power	
29	Power	Ground	30	Power	Ground
31	Power	NTC 0	32	Power	NTC 1
33	Power	NTC 2	34	Power	NTC 3
35	Power	NTC 4	36	Power	NTC 5
37	Power	NTC 6	38	Power	NTC 7
39	Power	Ground	40	Power	Ground

Table A.2: Pin configuration of the analog TBus connector. The pins without assignment can be used for internal functions.

A.7.3 Pin configuration of the Digital TBus PC104 connectors

Digital Connector:

Pin	Direction	Function	Pin	Power	Function
1	Power	Ground	2	Power	Ground
3	W	Addr 0 lsb	4	W	Addr 1
5	W	Addr 2	6	W	Addr 3
7	W	Addr 4	8	W	Addr 5
9	W	Addr 6	10	W	Addr 7
11	W	Read	12	W	Write
13	R/W	D 0 lsb	14	R/W	data 1
15	R/W	data 2	16	R/W	data 3
17	R/W	data 4	18	R/W	data 5
19	R/W	data 6	20	R/W	data 7
21	Power		22	Power	Ground
23	Power	+3.3 V	24	Power	+15 V
25	Power	Ground	26	Power	-15 V
27	R/W	Trigger 0	28	R/W	T 1
29	R/W	T 2	30	R/W	T 3
31	R/W	T 4	32	R/W	T 5
33	R/W	T 6	34	R/W	T 7
35	R/W	T 8	36	R/W	T 9
37	R/W	T 10	38	R/W	T 11
39	R/W	T 12	40	R/W	Ext. clock
41	Power	Ground	42	Power	Ground
43	Power	+1 Cell	44	Power	+1 Cell
45	Power	Ground	46	Power	Ground
47	Power	+2 Cell	48	Power	+2 Cell
49	Power	-2 Cell	50	Power	-2 Cell
51	Power	Ground	52	Power	Ground
53	Power	+4 Cell	54	Power	+4 Cell
55	Power	-4 Cell	56	Power	-4 Cell
57	Power	Ground	58	Power	Ground
59	Power	+6 Cell	60	Power	+6 Cell
61	Power	-6 Cell	62	Power	-6 Cell
63	Power	Ground	64	Power	Ground

Table A.3: Pin configuration of the digital TBus connector. Cell means the voltage of a $LiFePO_4$ cell.

A.7.4 List of TBus cards used

Name	Funktion	Ref.	Location	Additional information	total amount
TBus POF and Power card	Combined card of POF interface and stack power supply		Every stack	Seperated power board	7
Laser Current Driver MO	Current driver for master laseres, output of up to 500 mA		Rubidium and Potassium laser controll stacks in the laser electronic module		5
Laser Current Driver TA	Current driver for Power laseres, output of up to 2000 mA		Rubidium and Potassium laser power stacks in the laser electronic module	Seperated power board	5
Laser frequency controller	Card that processes spectroscopy and laser beat signals and provides the lock signal for the laser current drivers		Rubidium and Potassium laser controll stacks in the laser electronic module		3
DDS card	Card for direct digital synthesis. It can provide output frequencys from 50 MHz to 250 MHz		Rubidium and Potassium laser power stacks and rubidium laser control stack in the laser electronic module		7
Shutter card	Step engine control card. Used to control shutters in the laser module		Rubidium Laser Control and Potassium Laser Power stack and AUX stack		3
Chip and coil current driver	Current driver for chip structures and MOT coils.	[65]	Chip and coil currentdriver stack in the electronics module	galvanically isolated, seperated battery. Seperated power board	4
Fan card	simple fan control card		Rubidium laser control stack and Auxillary stack		2
Vibration card	Monitoring card for the vibration sensors in the physics package		Pump stack		1
Photodiode input card	Input card for fast photodiode signals		Auxillary stack and pump stack		2
UHV card	Driver card for the vacuum pump		Pump stack		1
UHV sensor	Sensor input for the vacuum sensor		Pump stack		1
2C6C adapter card	Card that converts 2C voltage to 6C voltage		Auxillary stack		1

Table A.4: Pin configuration of the analog TBus connector. The pins without assignment can be used for internal functions.

A.8 Appendix for the electronic module

A.8.1 Pin assignment of the back-end board output port

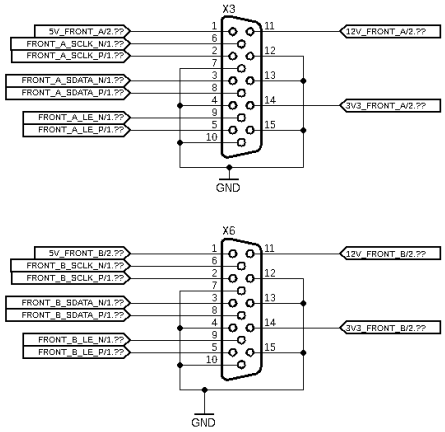

Figure A.7: Schematic of the back-ends output ports pin assignment. The serial connections are shown with P and N ending, illustrating the differential transmission.

A.8.2 Phase noise of the DDS card

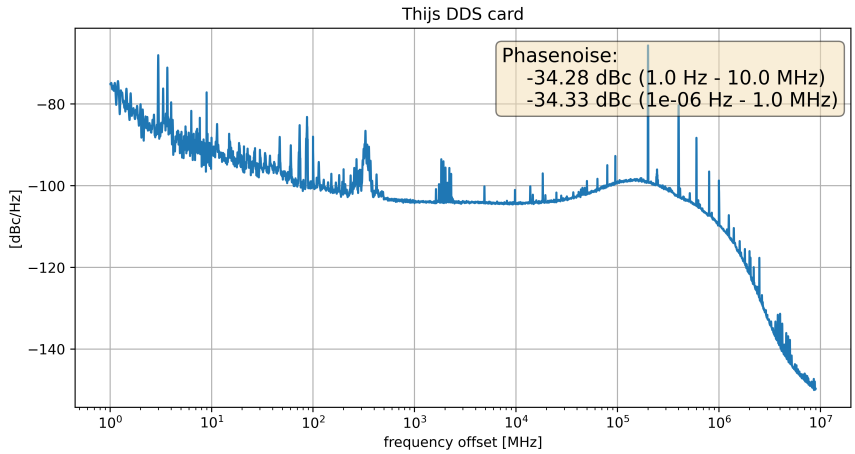

Figure A.8: Single side band phase noise performance of the DDS card described in 5.2. The phasenoise is measured to be -34.28 dBc between 1 Hz and 10 MHz with the DDS providing an output frequency of 50 MHz

A.9 Communication protocol between front-end and back-end board

A.9.1 Timing diagram of an attenuator transfer

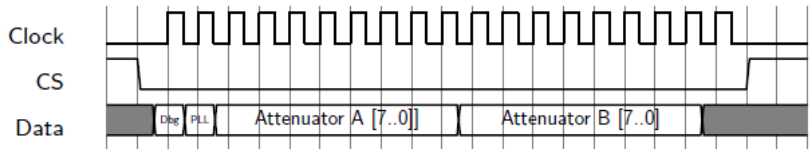

Figure A.9: Timing diagram of an attenuator transfer from back-end board to front-end. The transfer is initiated by a falling edge of CS. After one debug bit a PLL-select bit is transmitted that sets the target PLL for the next transfer to a HMC 834. This bit is followed by 16 data bits for the attenuator settings.

A.9.2 Timing diagram of a PLL transfer

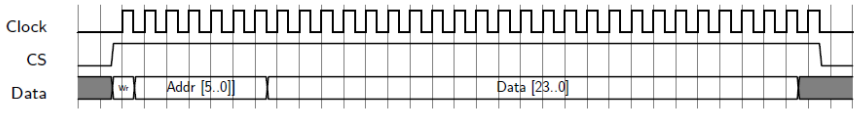

Figure A.10: Timing diagram of an HMC 834 data transfer from back-end board to front-end. The transfer is initiated by a rising edge of CS. The target PLL is set by the previous transfer of attenuator settings. The first bit commands a read or write operation. This bit is followed by 6 address bits and 24 data bits, corresponding directly to address and data of the interface registers of the HMC 834.

A.10 Level diagrams

A.10.1 Level diagram of rubidium 87

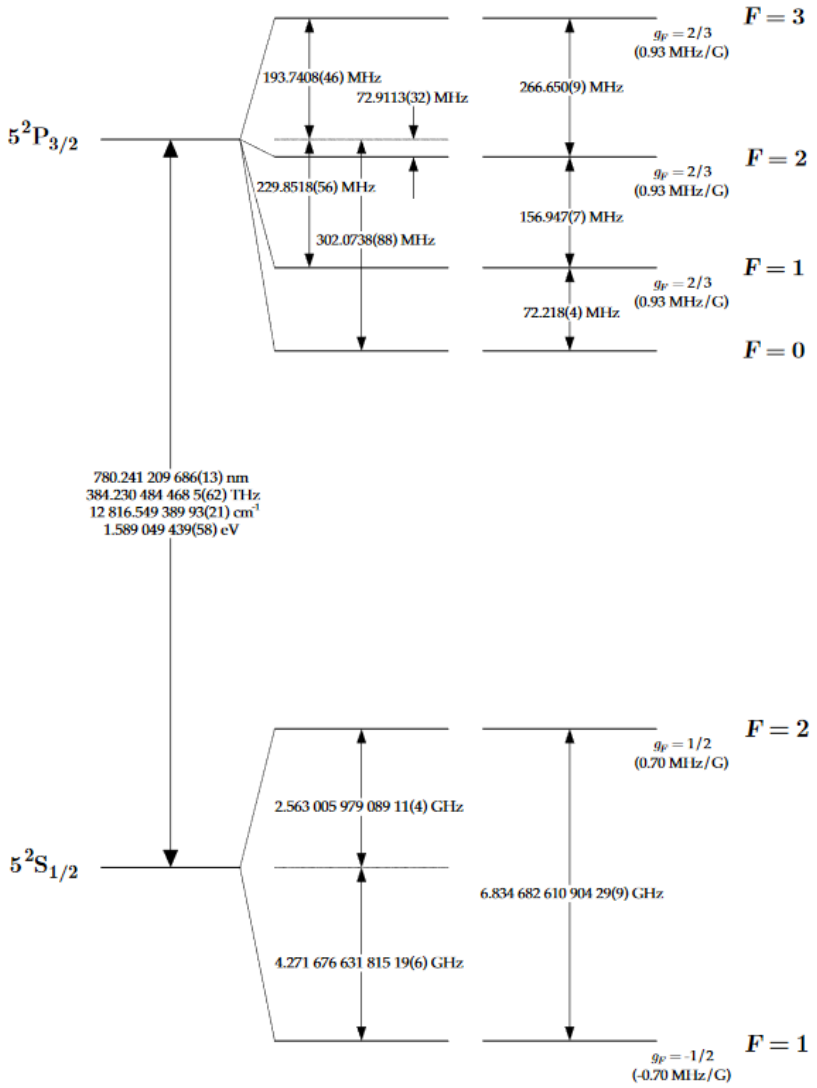

Figure A.11: Level diagram of rubidium 87. Picture remained unchanged from [82].

A.10.2 Level diagram of potassium 39, 40 and 41

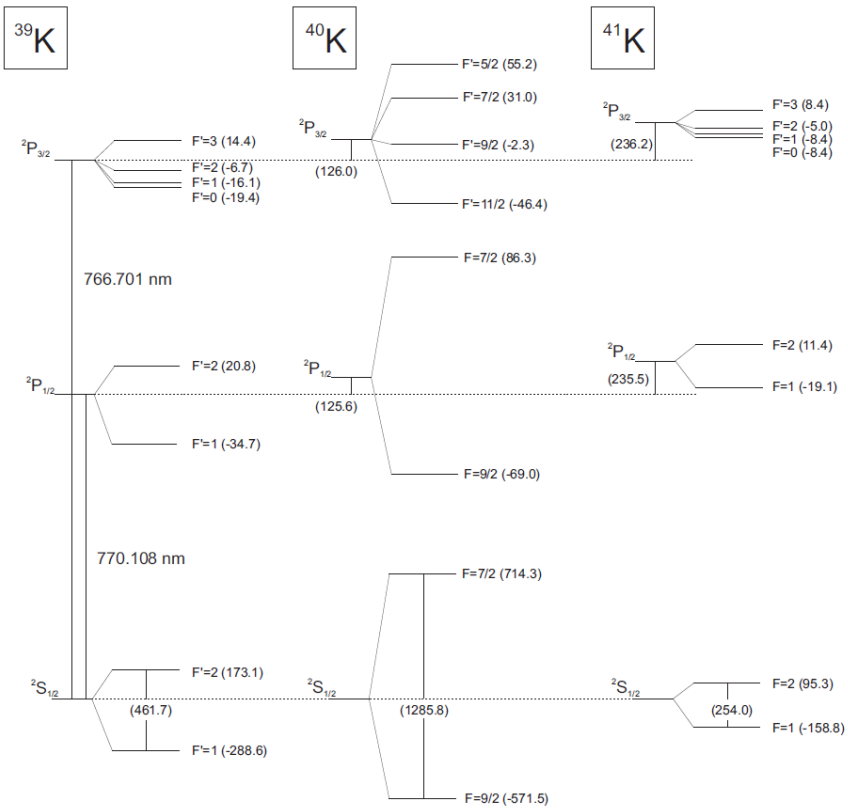

Figure A.12: Level diagram of potassium 39, 40 and 41. Picture remained unchanged from [85].

APPENDIX B

CAD-models, layouts and schematics

B.0.1 Top level schematics

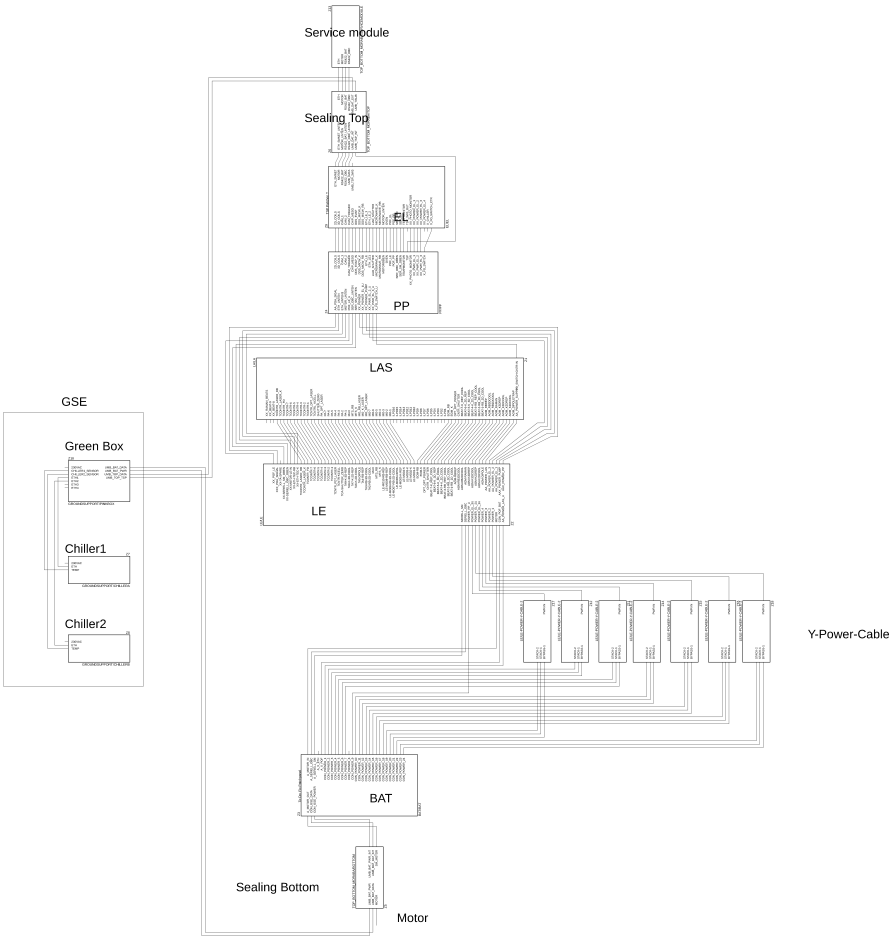

Figure B.1: Top-level schematic of the scientific payload. The connections between the electronic modules and the physics package and laser module are shown as well as the connections to the ground support. The module symbols are generated by the make script mentioned in 5.

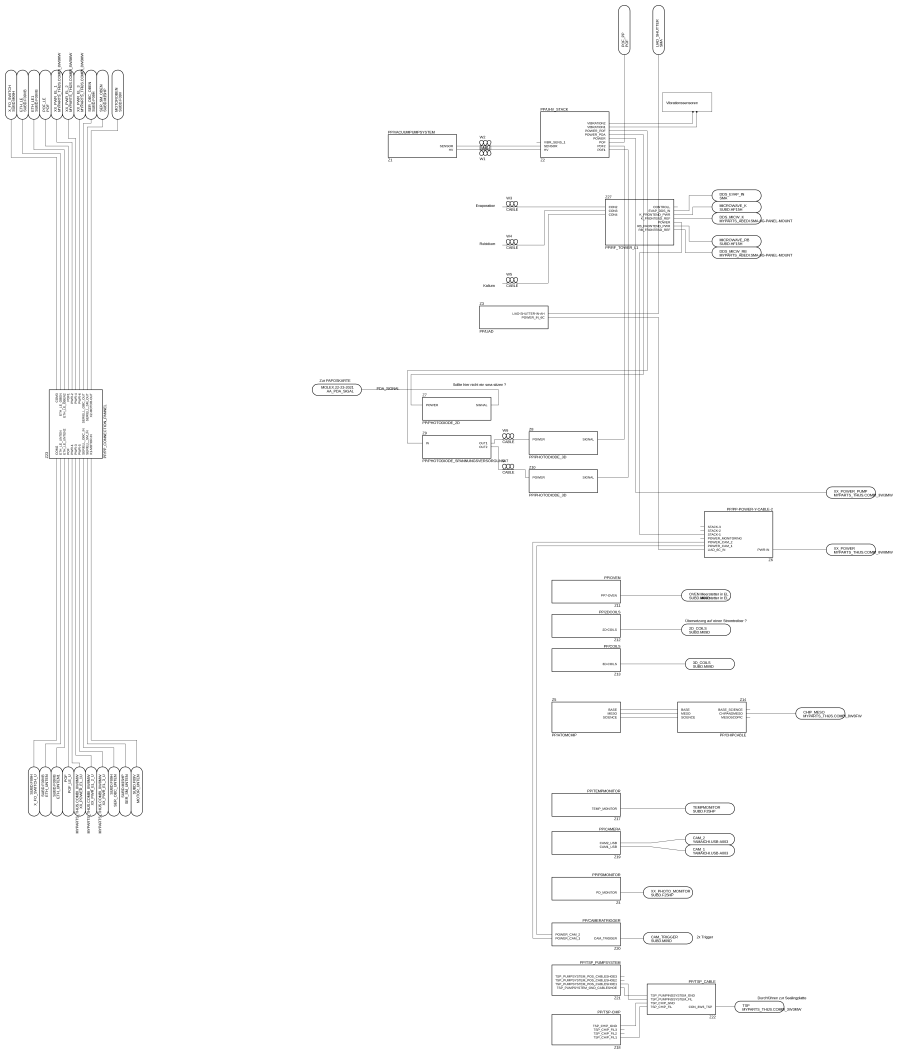

Figure B.2: Top-level schematic of the physics package. The connections between the sub modules are shown. The sub-module symbols are generated by the make script mentioned in 5.

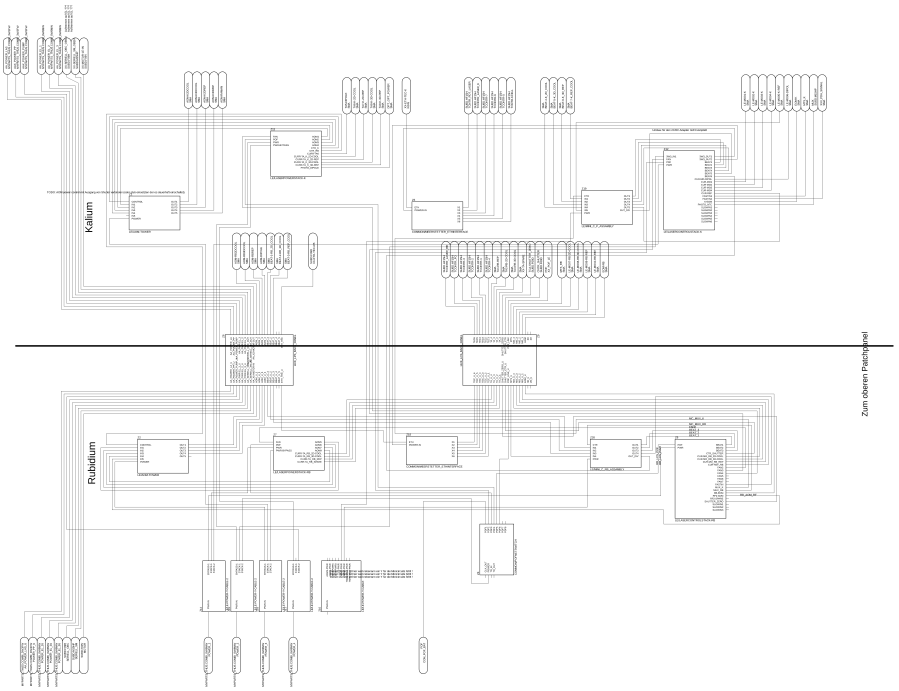

Figure B.3: Top-level schematic of the laser electronic module. The connections between the sub-modules are shown. The sub-module symbols are generated by the make script mentioned in 5.

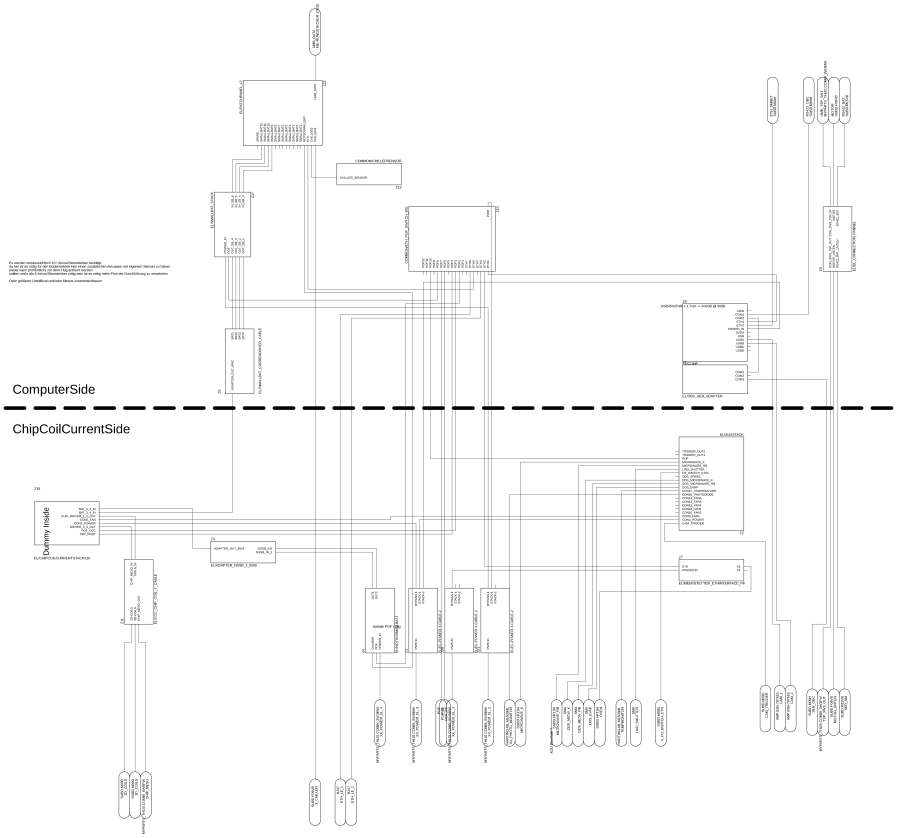

Figure B.4: Top-level schematic of the electronic module. The connections between the sub-modules are shown. The sub-module symbols are generated by the make script mentioned in 5.

B.0.2 Layout of the mother-board

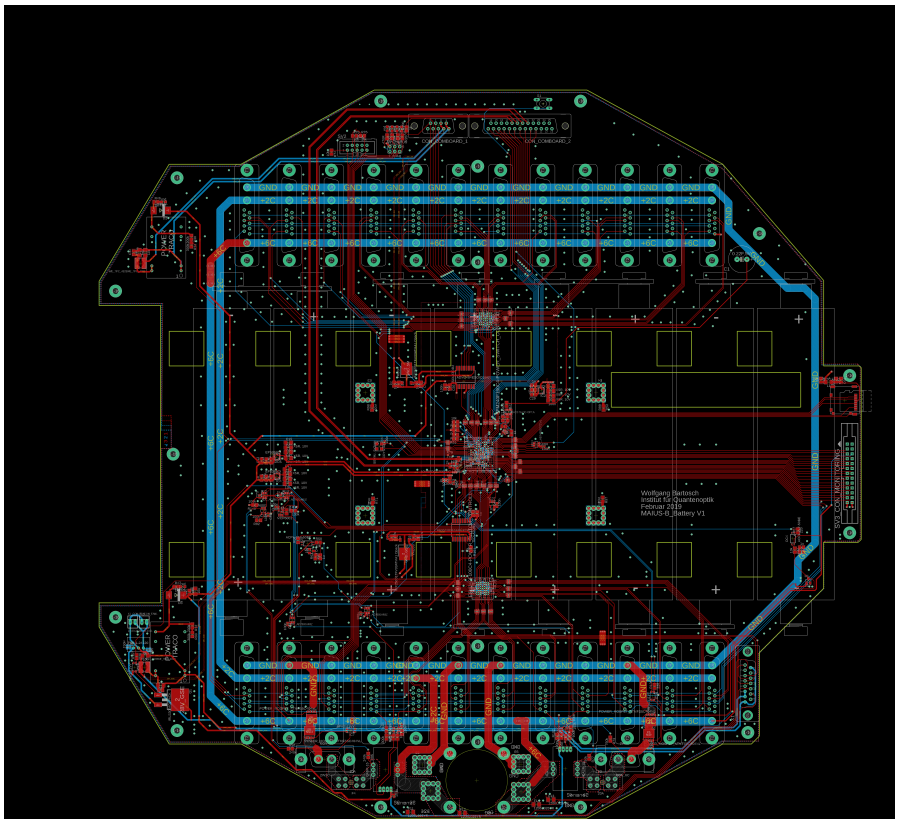

Figure B.5: Layout of the battery modules motherboard. The main FPGA in the center is input output extended by two slave CPLDs to manage the connections to the plug-in boards. Fuses and the backup charging system are present on this board. The motherboards ground also represents the common ground of the electronic system. Two feed-throughs are connected two the board to connect the payload to the lower umbillicals.

B.0.3 Schematic of the mother-board

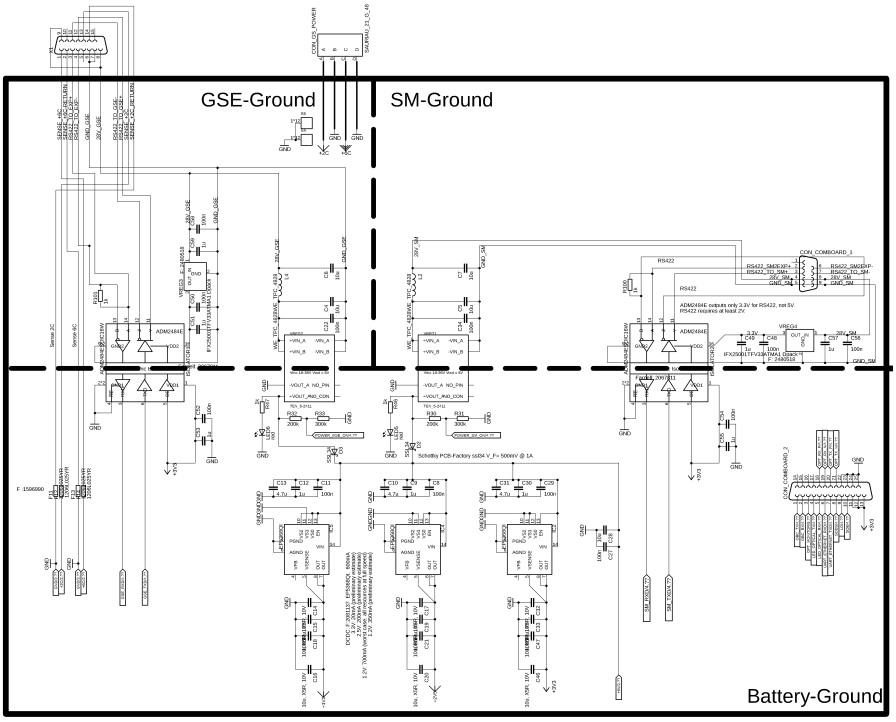

Figure B.6: Schematic of the battery modules motherboard. This sheet of the schematic contains the power supply and communication isolation of the motherboard. The connection to service module and ground support electronics are visible in the top left. The plug-in board connections to the communication board is visible on the right. The dashed lines represent the different system grounds.

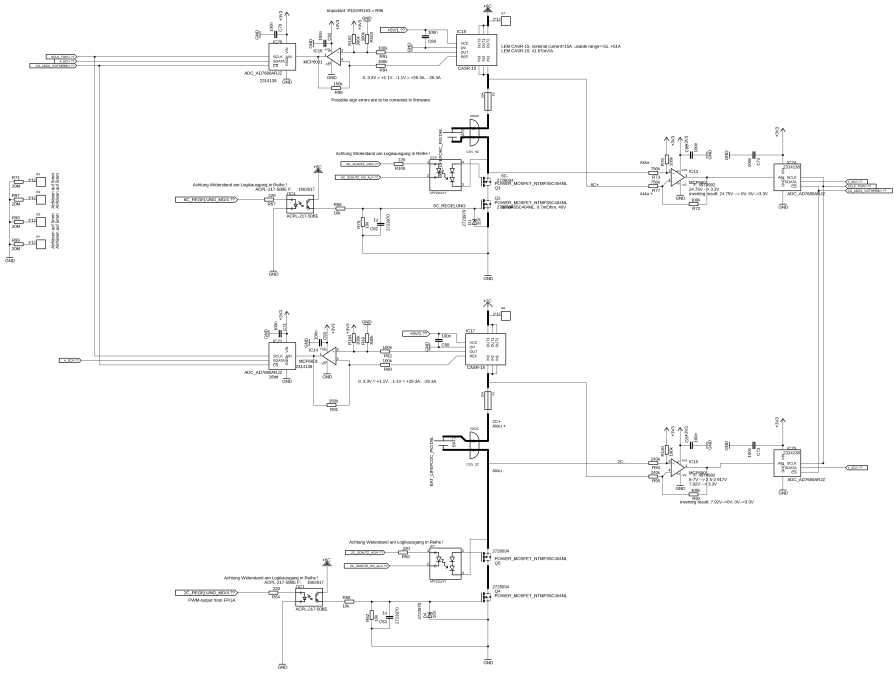

Figure B.7: Schematic of the battery modules motherboard. This sheet of the schematic contains the main fuses, current sensors, voltage sensors, the main power switches and the backup charging systems for the two cell and the six cell extra battery pack.

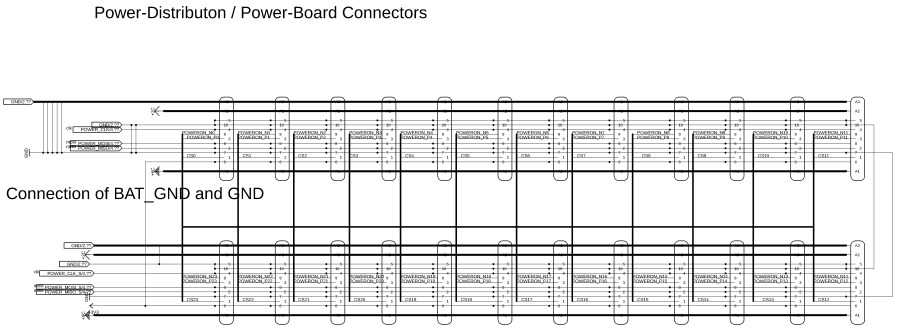

Figure B.8: Schematic of the battery modules motherboard. This sheet of the schematic contains the connections to the plug-in output channel boards

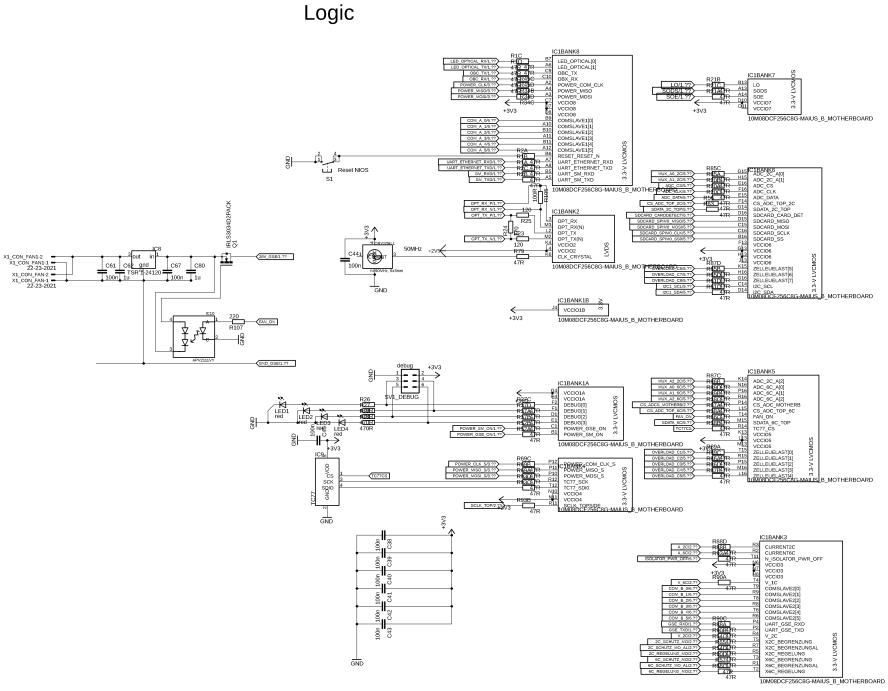

Figure B.9: Schematic of the battery modules motherboard. This sheet of the schematic contains the logic circuits of the motherboard.

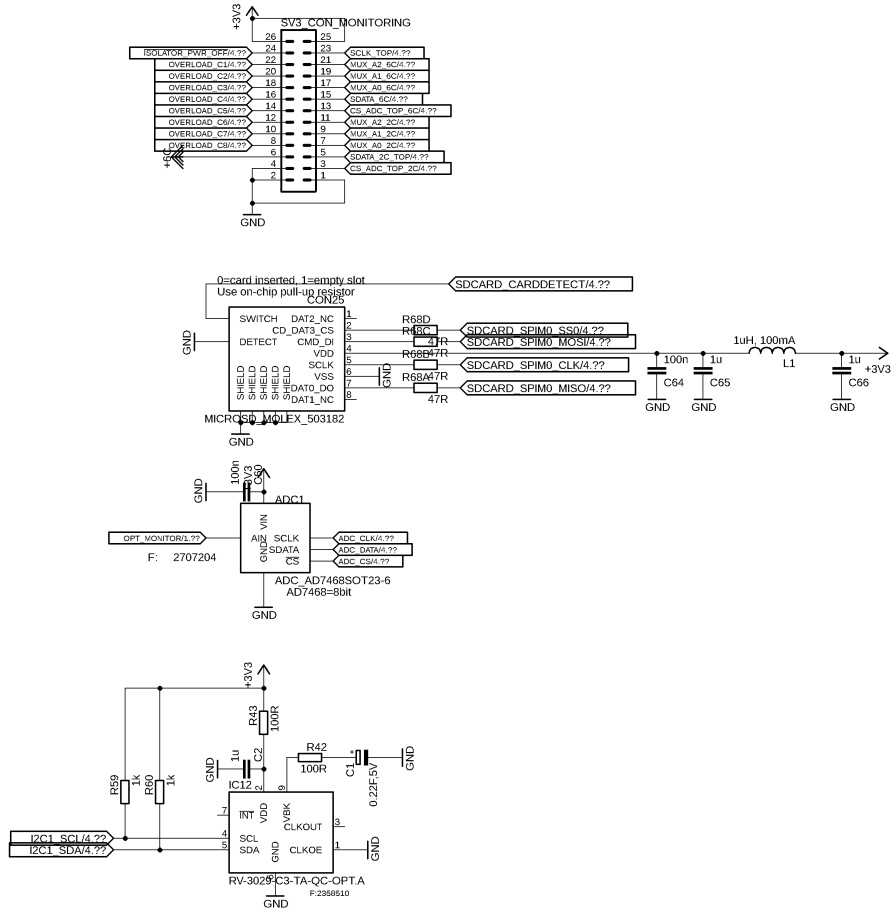

Figure B.10: Schematic of the battery modules motherboard. This sheet of the schematic contains the second part of logic circuits of the motherboard.

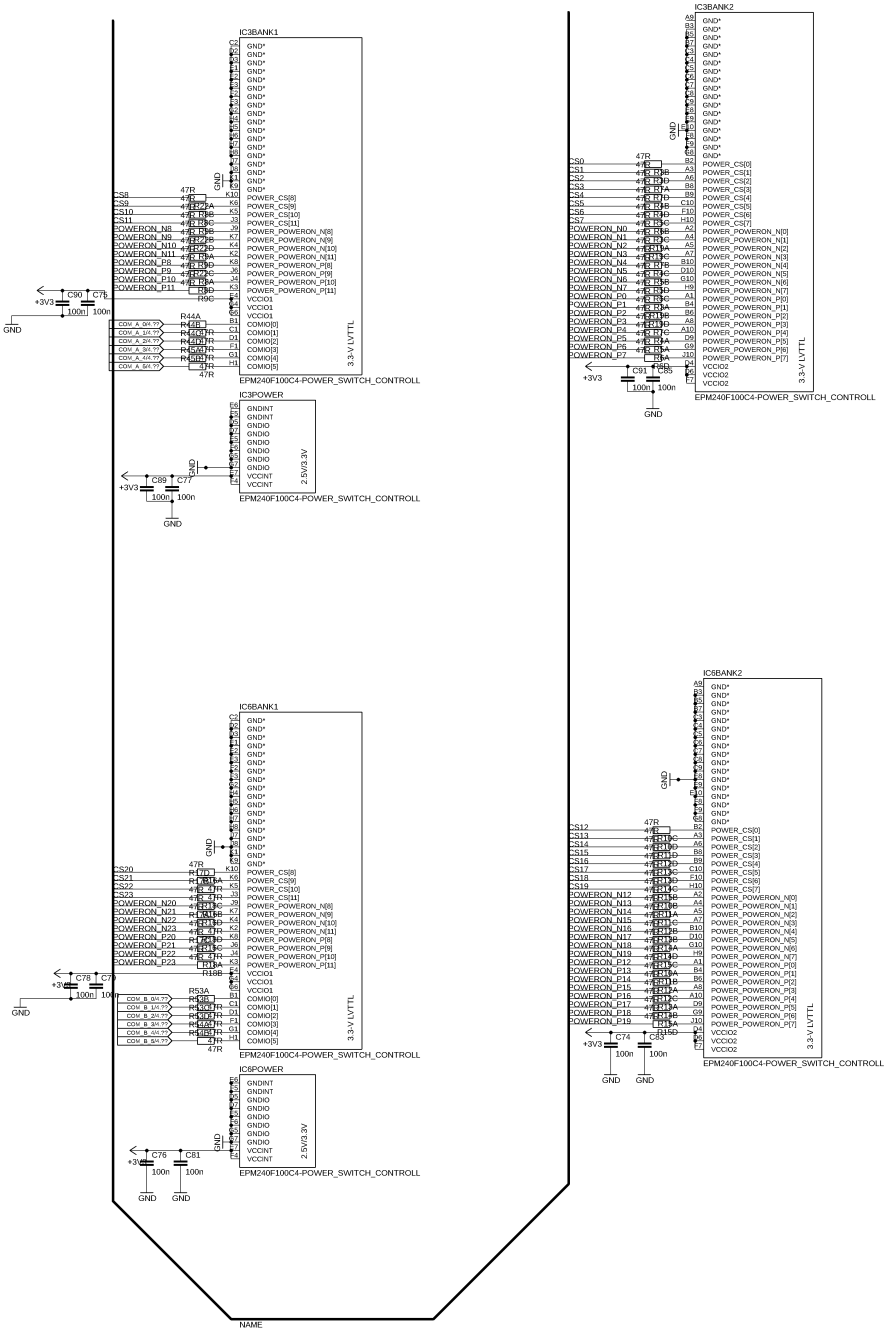

Figure B.11: Schematic of the battery modules motherboard. This sheet of the schematic contains the third part of logic circuits of the motherboard.

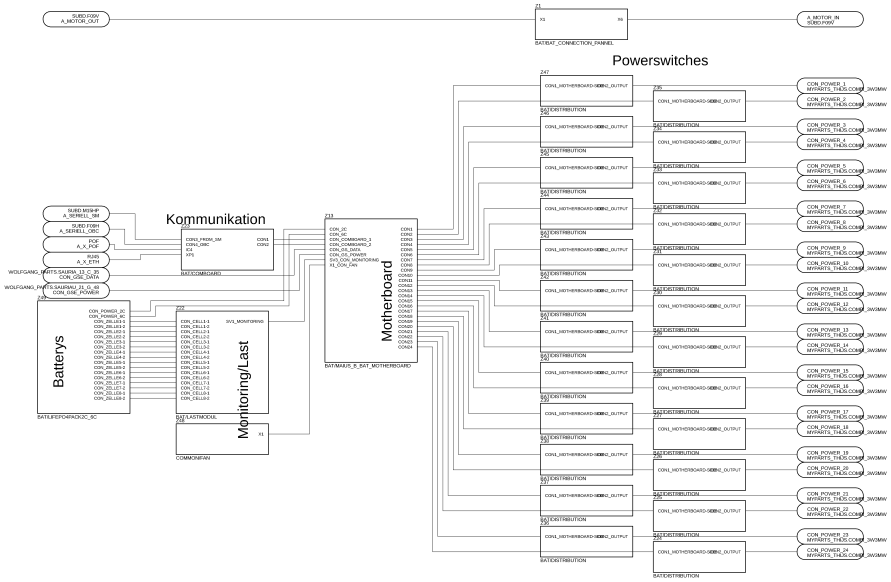

Figure B.12: Top level schematic of the battery module. The connections between the individual components are shown.

B.0.4 Layout of the output channel plug-in boards

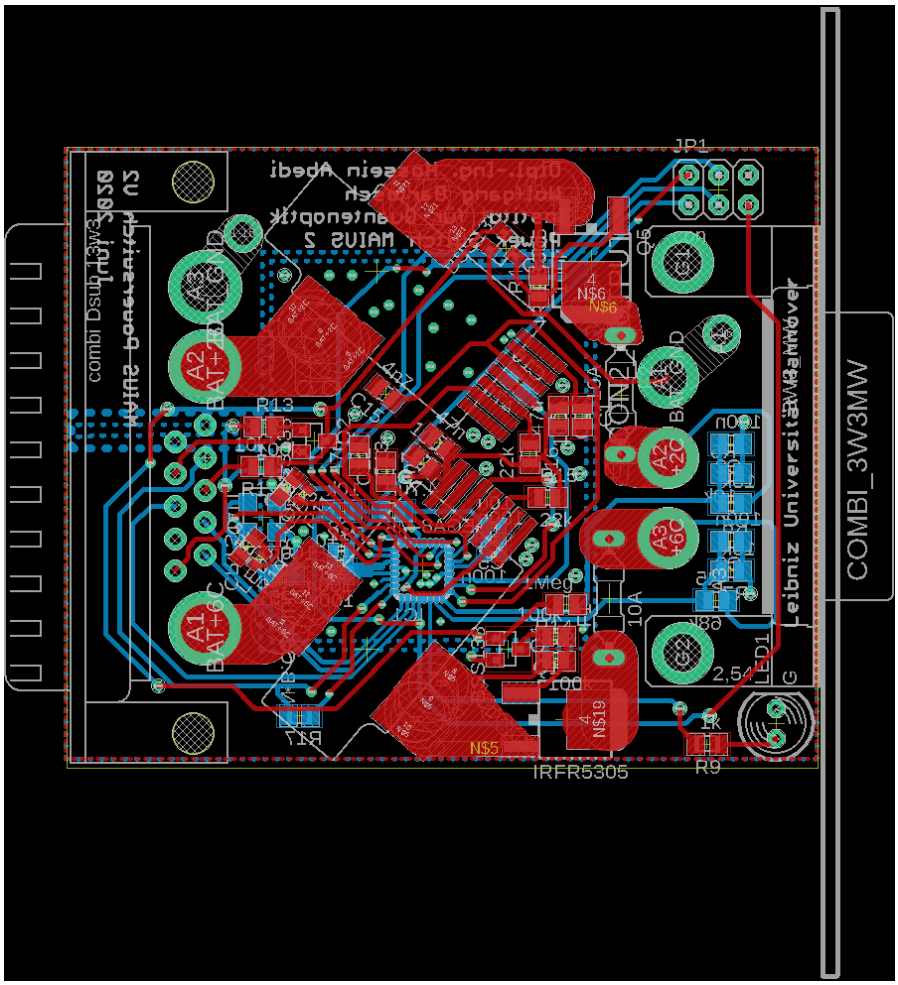

Figure B.13: Layout of the output channel plug-in board.

B.0.5 Schematic of the output channel plug-in boards

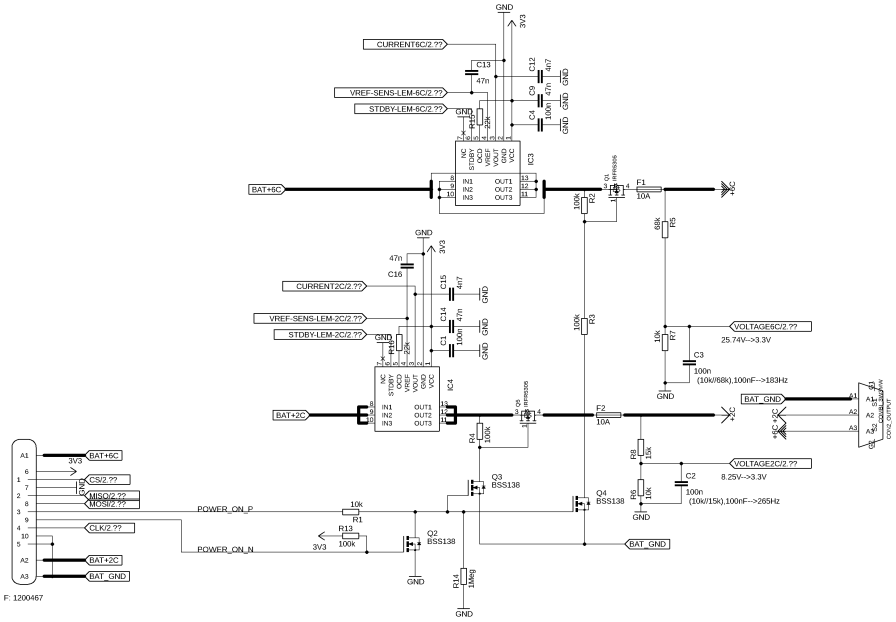

Figure B.14: Schematic of the output channel plug-in boards, this sheet shows the input and output connector of the board as well as the current sensors for the two cell and the six cell output current. The six cell voltage is measured with the voltage divider R7 and R5. The two cell voltage is measured over the voltage divider formed by R6 and R8. The signals POWER_ON_P and POWER_ON_P are used for the safe start of the board.

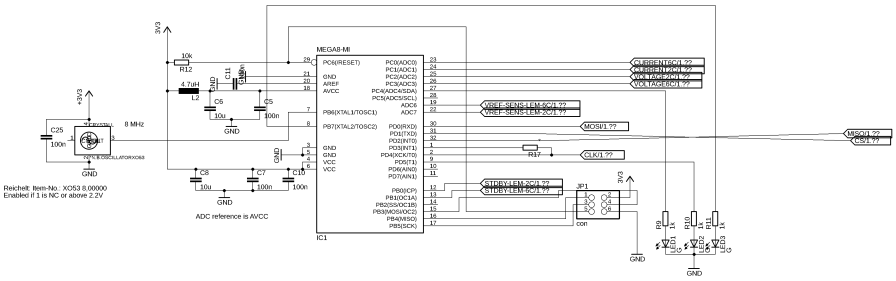

Figure B.15: Schematic of the output channel plug-in boards. This sheet shows the logic circuits of the board.

B.0.6 Layout of the battery communication board

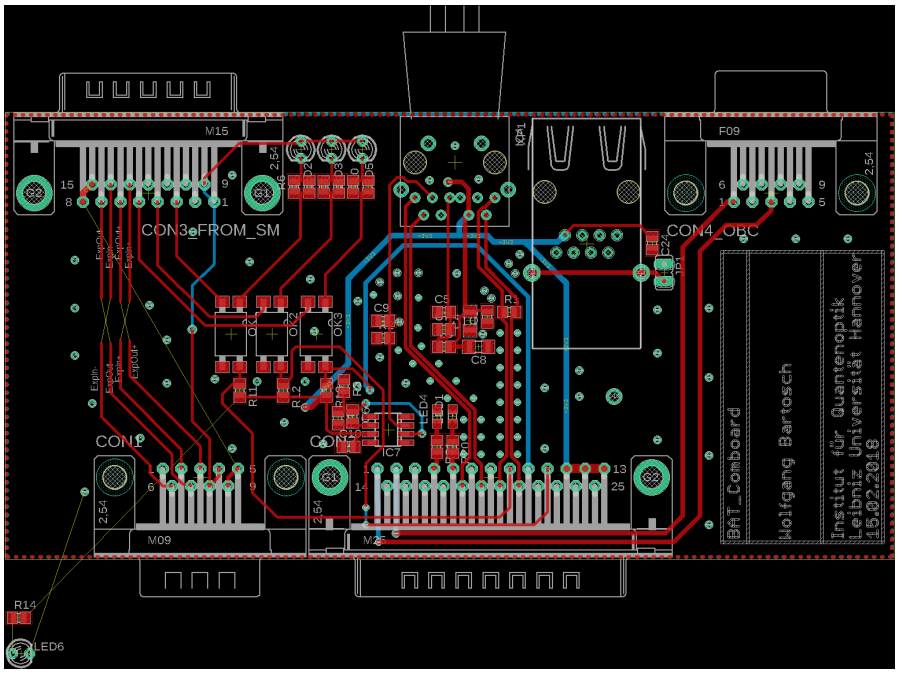

Figure B.16: Layout of the battery communication board.

B.0.7 Schematic of the battery communication board

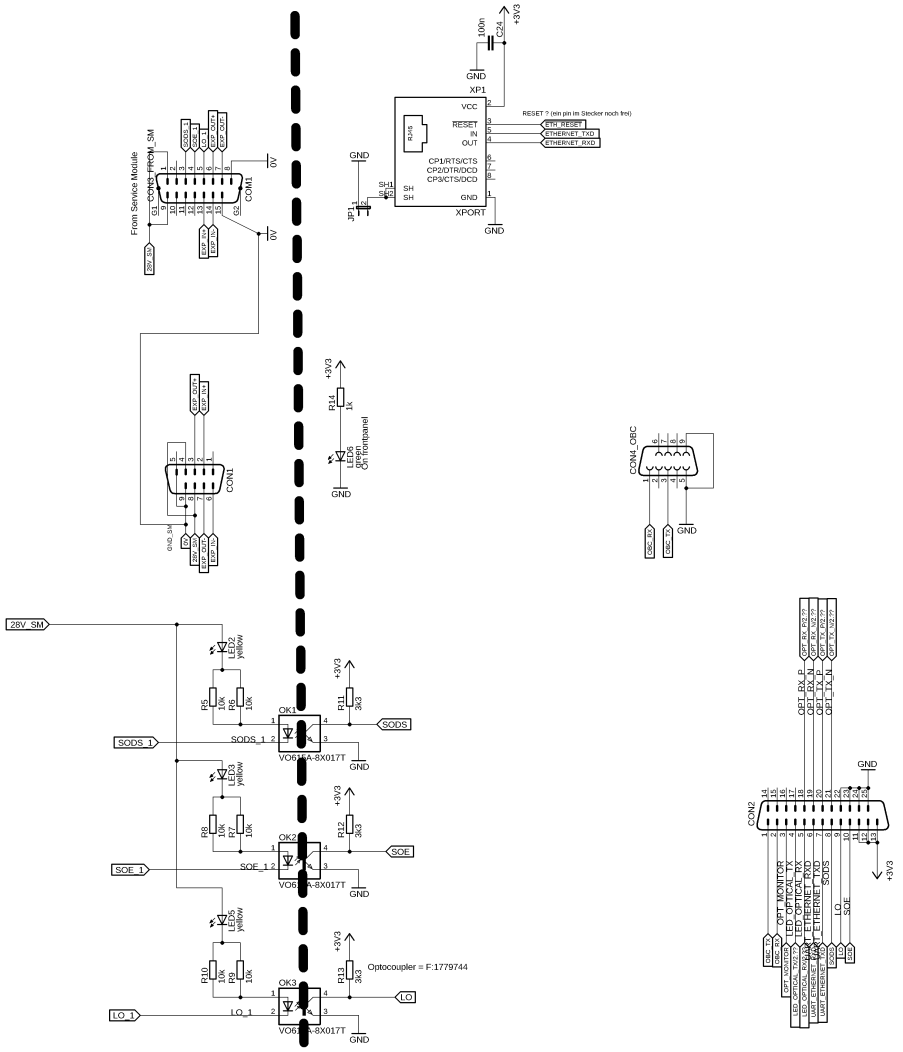

Figure B.17: Schematic of the battery communication board, this sheet shows the in- and outputs of the board. The grounds of service module and battery module are separated by the dashed line.

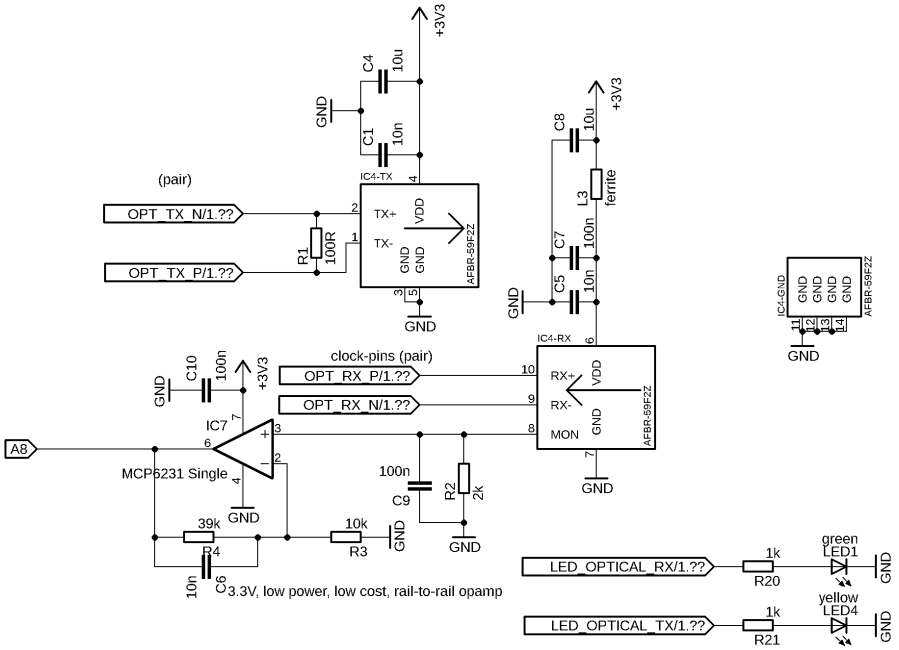

Figure B.18: Schematic of the battery communication board, this sheet shows the POF connector

B.0.8 Layout of the battery overcharge protection board

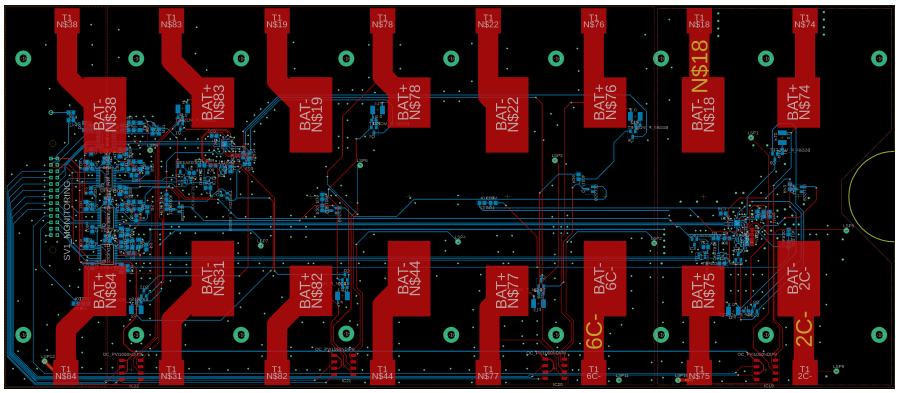

Figure B.19: Layout of the battery overcharge protection board, the commercial overcharge protection modules are shown as print on the PCB. Motherboard and overcharge protection board are connected over a ribbon cable (SV1).

B.0.9 Schematic of the battery overcharge protection board

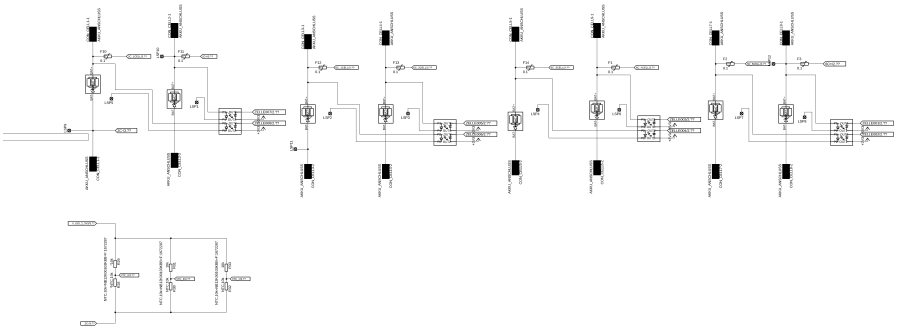

Figure B.20: Schematic of the battery overcharge protection board. This sheet shows the connections of the overcharge protection elements. The status LEDs of these elements are read by the four shown optocoupplers.

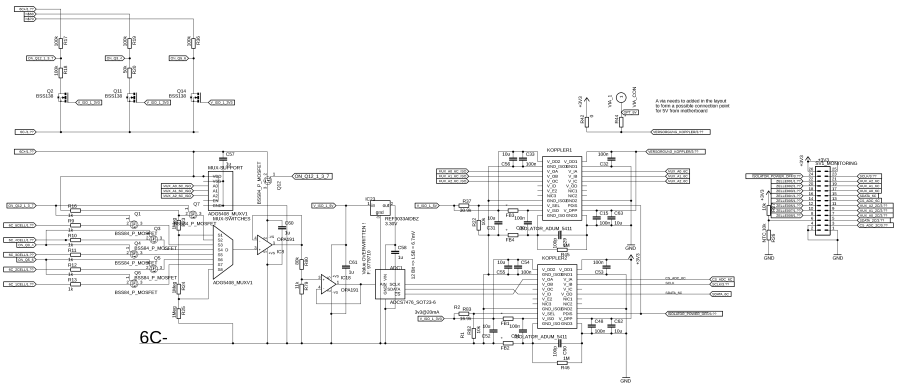

Figure B.21: Schematic of the battery overcharge protection board. This sheet shows the monitoring circuits of the six cell battery pack. The battery voltages shown on the left side are connected to a multiplexer (MUXV1). The output of the multiplexer is analog digital converted by ADC1. The serial interface of the multiplexer, the ADC output and the digital signals for the main FPGA are isolated by the magnetic coupplers KOPPLER_1 and KOPPLER_2. The isolators of type ADUM 5411 also provide the isolated power supply for the monitoring system.

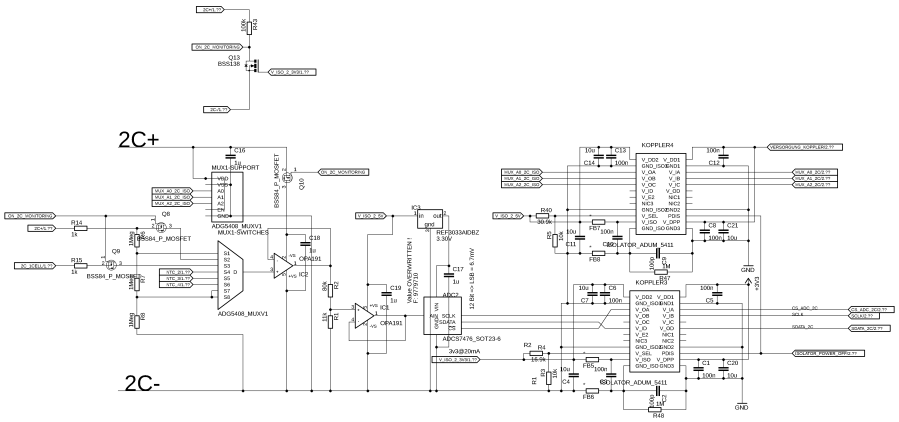

Figure B.22: Schematic of the battery overcharge protection board. This sheet shows the monitoring circuits of the two cell battery pack. The battery voltages shown on the left side are connected to a multiplexer (MUX1). The output of the multiplexer is analog digital converted by ADC2. The serial interface of the multiplexer, the ADC output and the digital signals for the main FPGA are isolated by the magnetic couplers KOPPLER_3 and KOPPLER_4. The isolators of type ADUM also provide the isolated power supply for the monitoring system.

B.0.10 Layout of the two cell extra battery

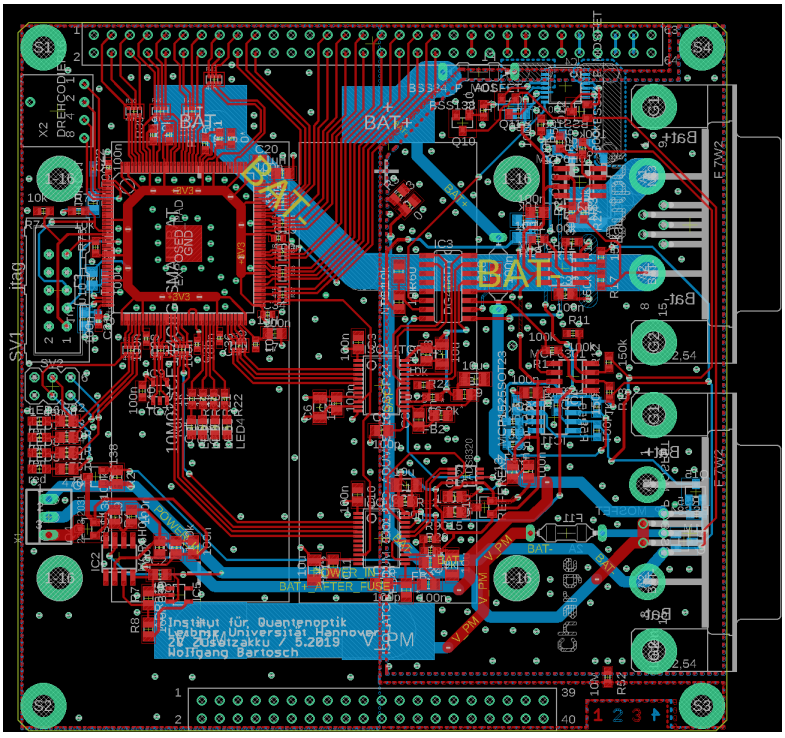

Figure B.23: Layout of the two cell extra battery. The battery are mounted on the backside of the BCB and not shown in the layout. The pin header X1 at the left side of the board is the connection to the power electronics board

B.0.11 Schematic of the two cell extra battery

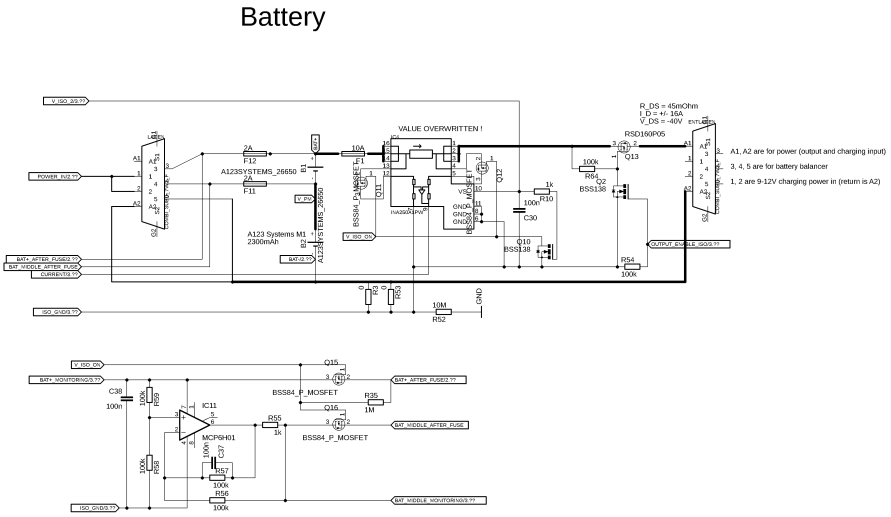

Figure B.24: Schematic of the two cell extra battery. This sheet of the schematic contains the Power output and charging path of the PCB. The transistors Q2, Q10, Q11, Q12, Q15 and Q16 are responsible for the separation of the monitoring electronics and the battery in case of not use.

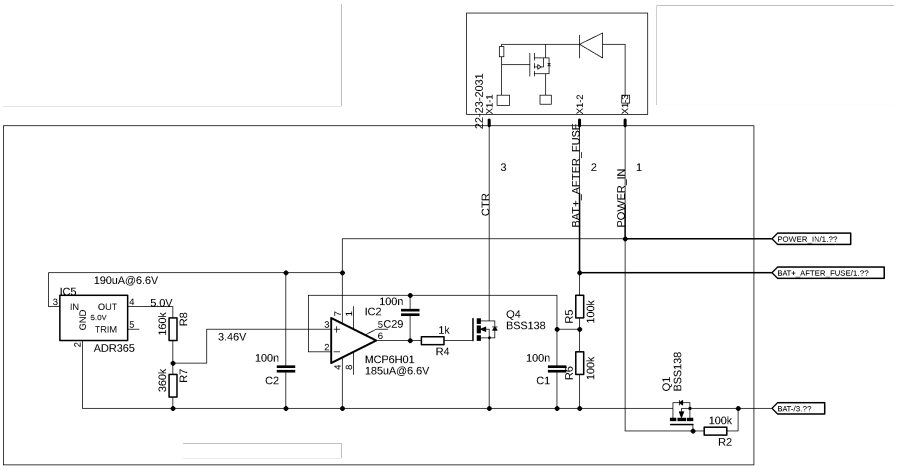

Figure B.25: Schematic of the two cell extra battery. This sheet of the schematic contains the charging regulation of the battery. IC5 acts as reference for the charging end voltage and Q5 switches the charging current. The separate power board is shown as a drawing.

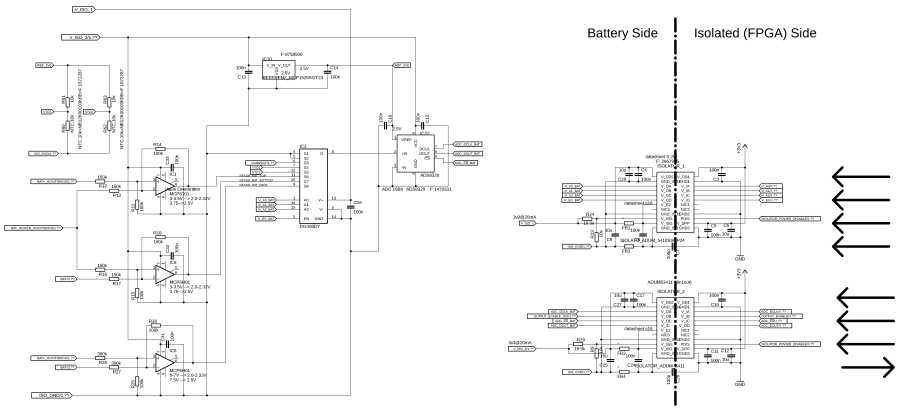

Figure B.26: Schematic of the two cell extra battery. This sheet of the schematic contains the monitoring system. The voltages and signals of the current sensors are collected on the left side and multiplexed by IC3. The serial interface of the multiplexer and the digital signals for the main FPGA are isolated by the magnetic coupplers ISOLATOR_1 and ISOLATOR_2. The isolators of type ADUM 5411 also provide the isolated power supply for the monitoring system.

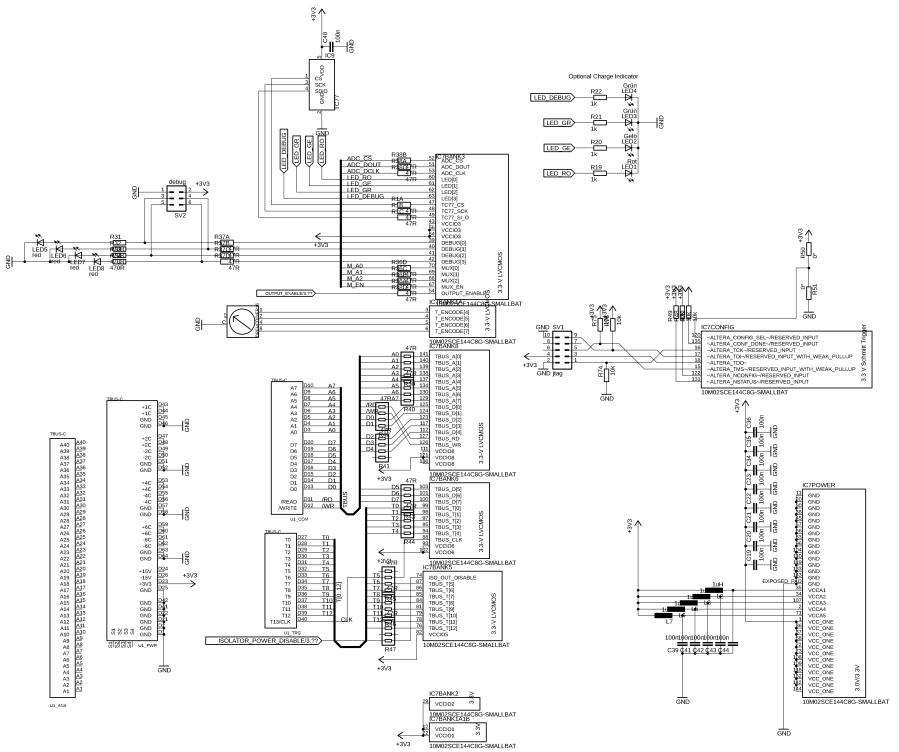

Figure B.27: Schematic of the two cell extra battery. This sheet of the schematic contains the logic circuits.

B.0.12 Layout of the six cell extra battery

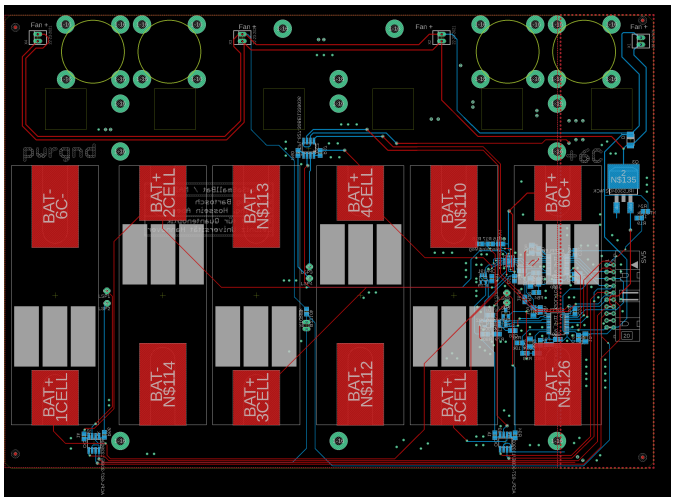

Figure B.28: Layout of the six cell extra battery. This part of the layout shows the monitoring and overcharge protection PCB. The commercial overcharge protection modules are shown as print on the PCB.

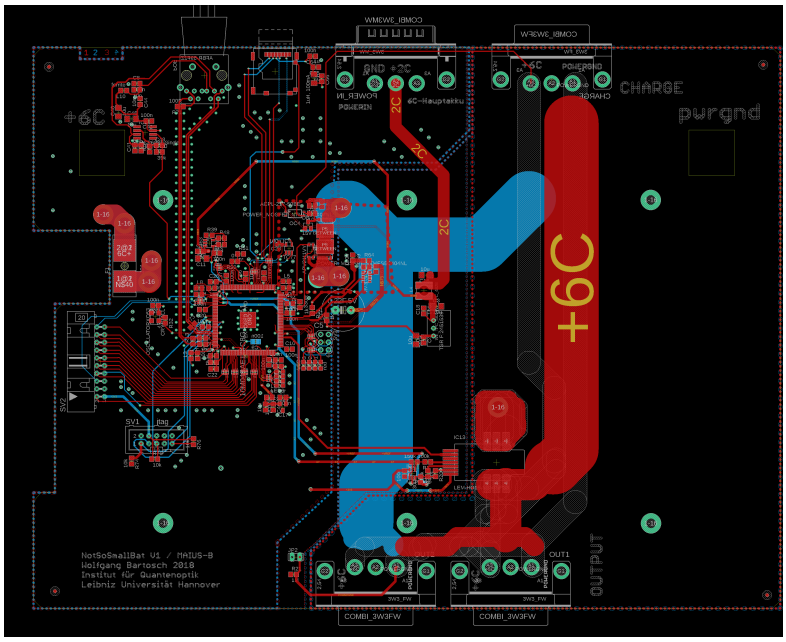

Figure B.29: Layout of the six cell extra battery. This part of the layout shows the logic and charging regulation PCB. Both PCBs of the six cell extra battery are connected by a ribbon cable connected to SV2. The wide tracks on the PCB are not coated and can later be reinforced with wire for higher currents.

B.0.13 Schematic of the six cell extra battery

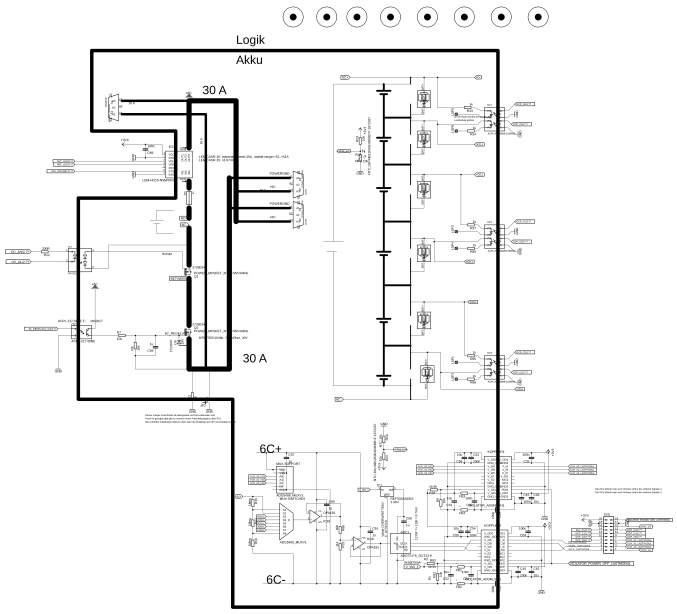

Figure B.30: Schematic of the sx cell extra battery. This sheet of the schematic contains the charging system as well as the monitoring system. Both system are copies of the six cell circuit of the main battery motherboard shown in B.6. This part of the schematic also shows the opto-coupplers used to read the status of the commercial overcharge protection modules (OC1-3).

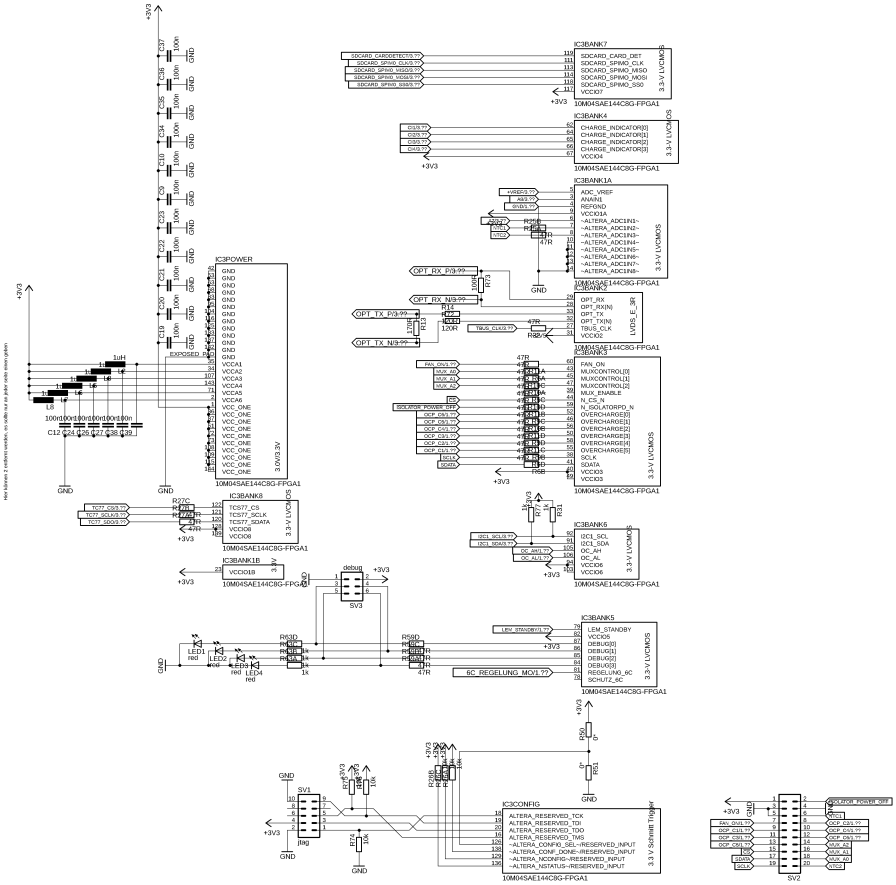

Figure B.31: Schematic of the six cell extra battery. This sheet of the schematic contains the logic circuits.

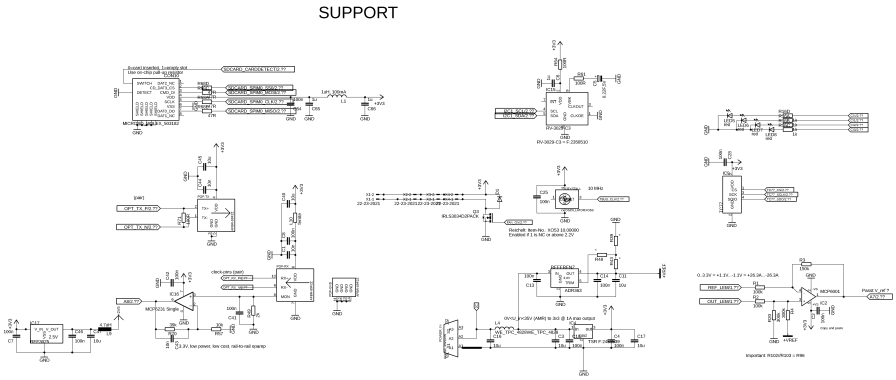

Figure B.32: Schematic of the six cell extra battery. This sheet of the schematic contains a number of support components like a real time clock (IC15), a crystal oscillator and the POF connector.

B.0.14 Layout of the microwave back-end

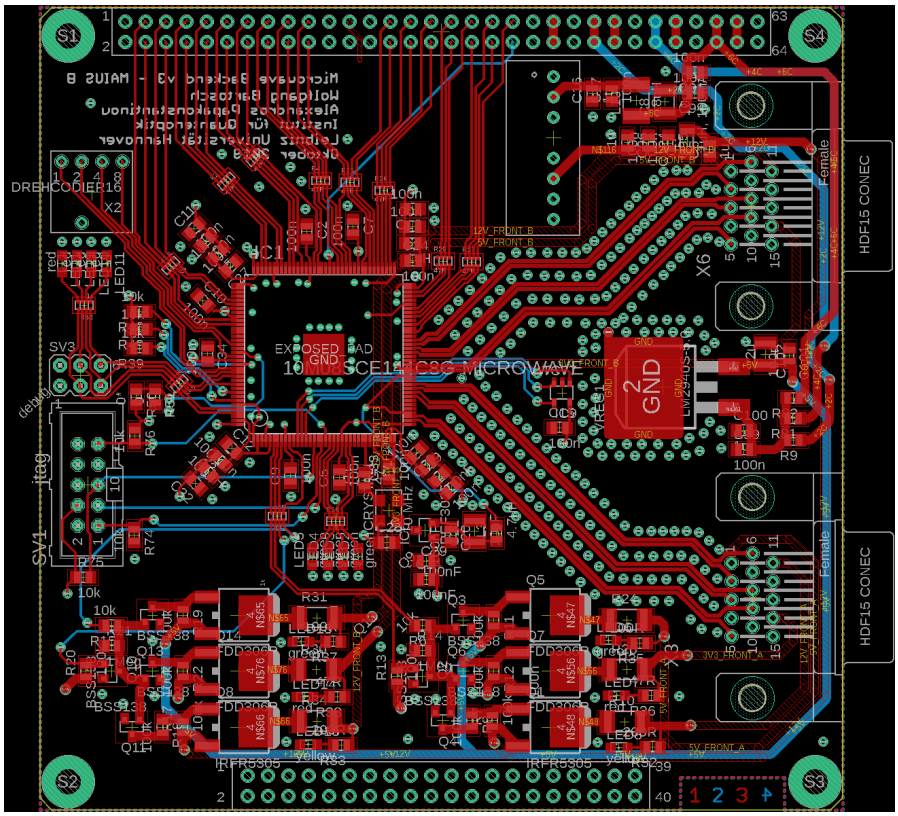

Figure B.33: Layout of the microwave back-end board

B.0.15 Schematic of the microwave back-end

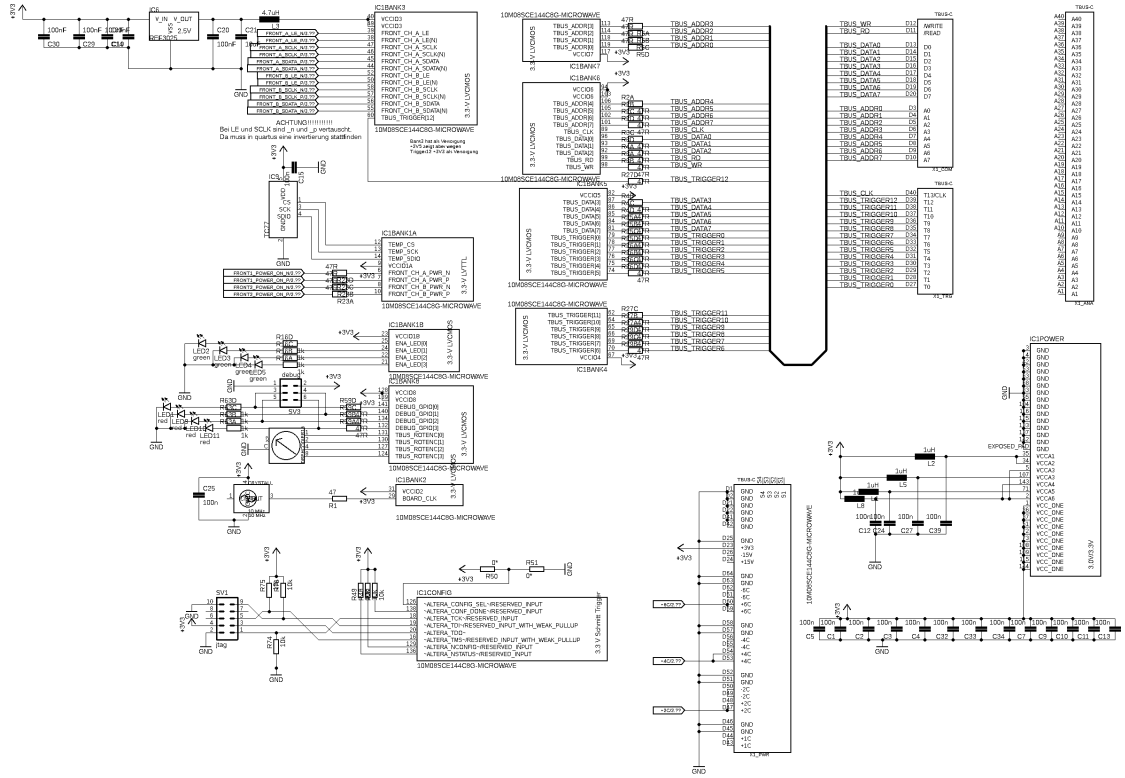

Figure B.34: Schematic of the microwave back-end side 1. This sheet contains the logic circuit.

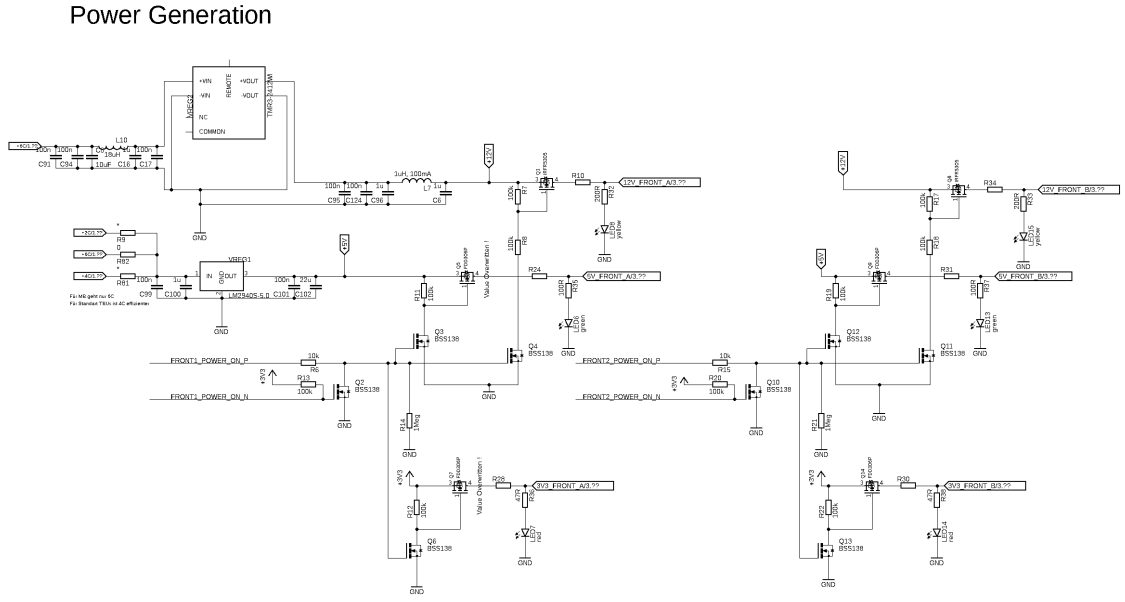

Figure B.35: Schematic of the microwave back-end side 2. This sheet contains the power supply output stage for the front-ends.

B.0.16 Layout of the microwave front-end

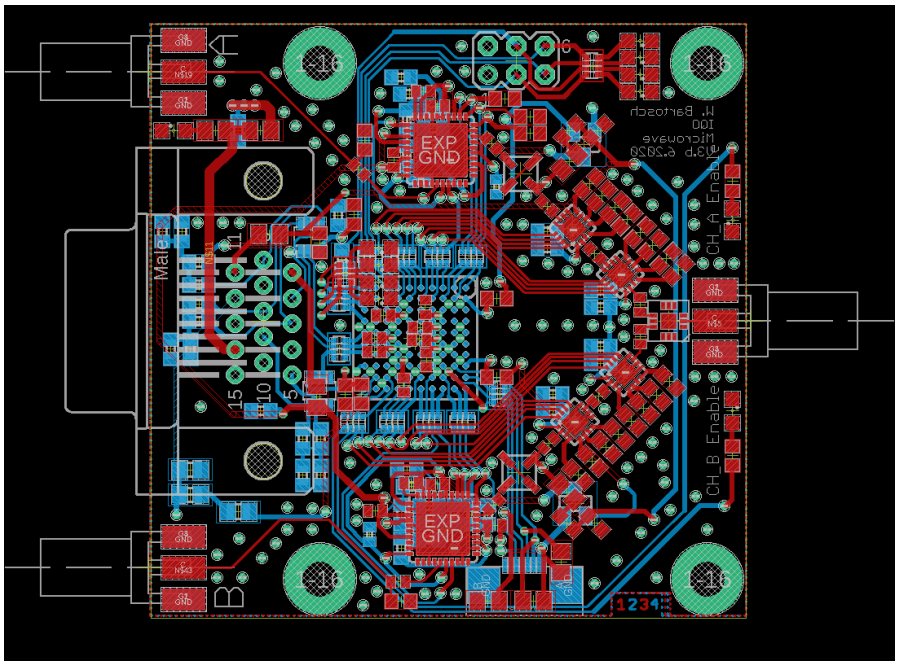

Figure B.36: Layout of the microwave front-end board.

B.0.17 Schematic of the microwave front-end board

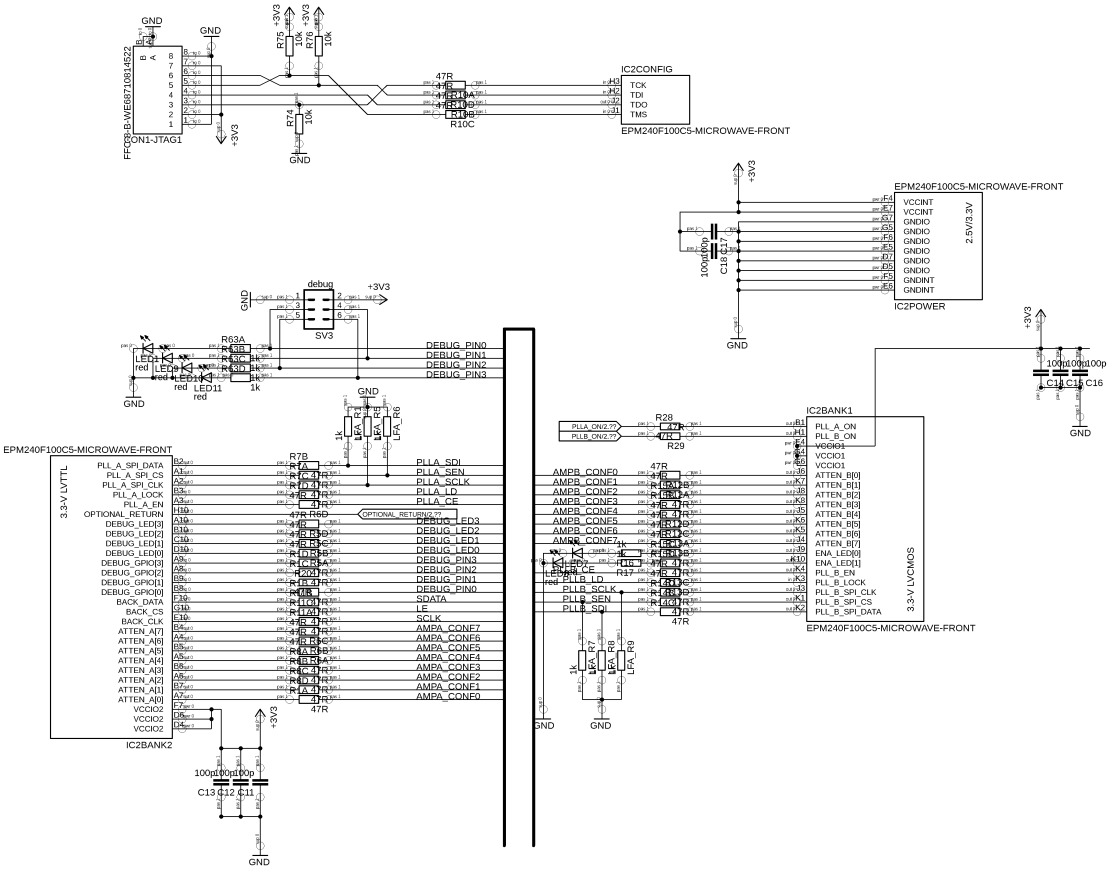

Figure B.37: Schematic of the microwave front-end. This sheet contains the logic circuits.

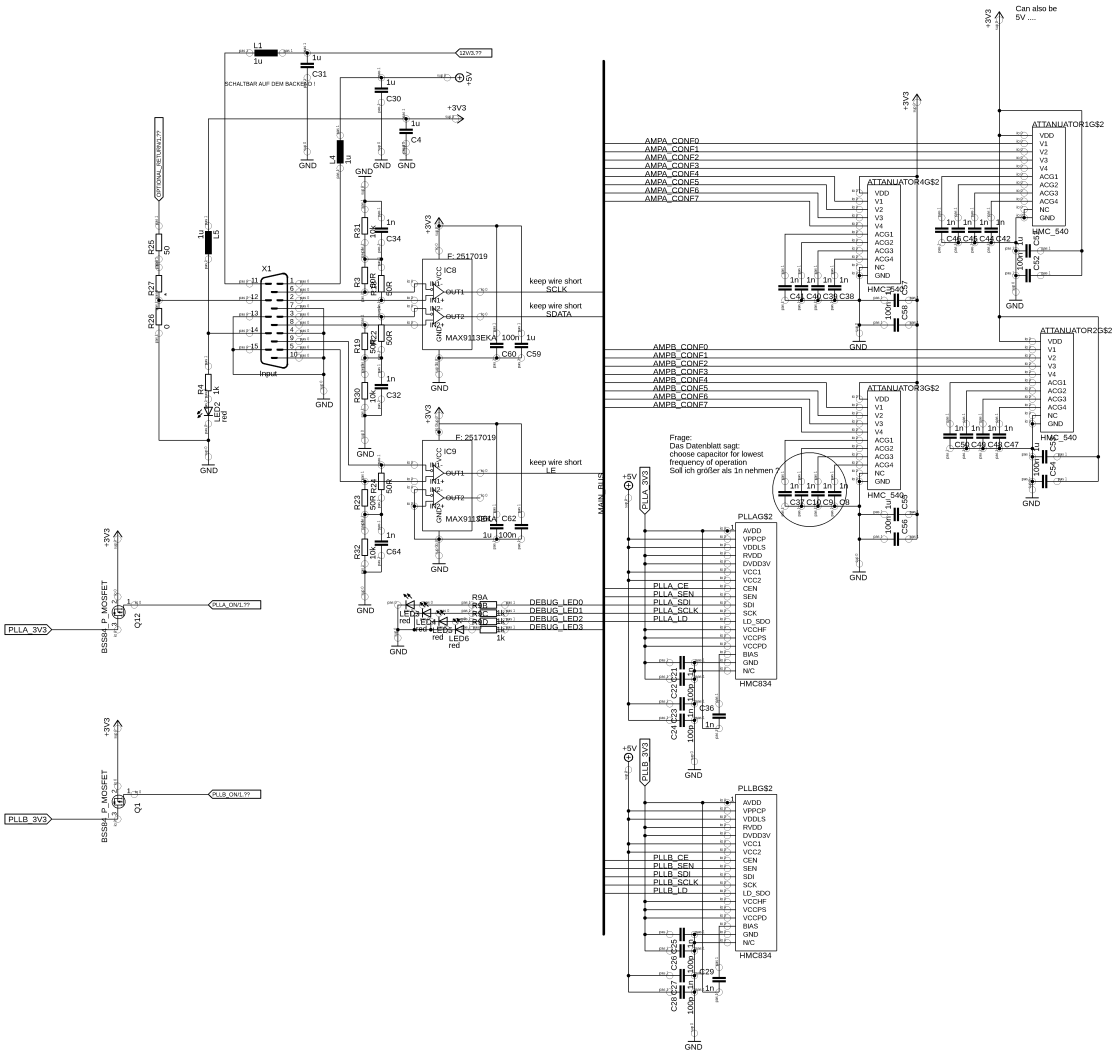

Figure B.38: Schematic of the microwave front-end. This sheet contains the input stage.

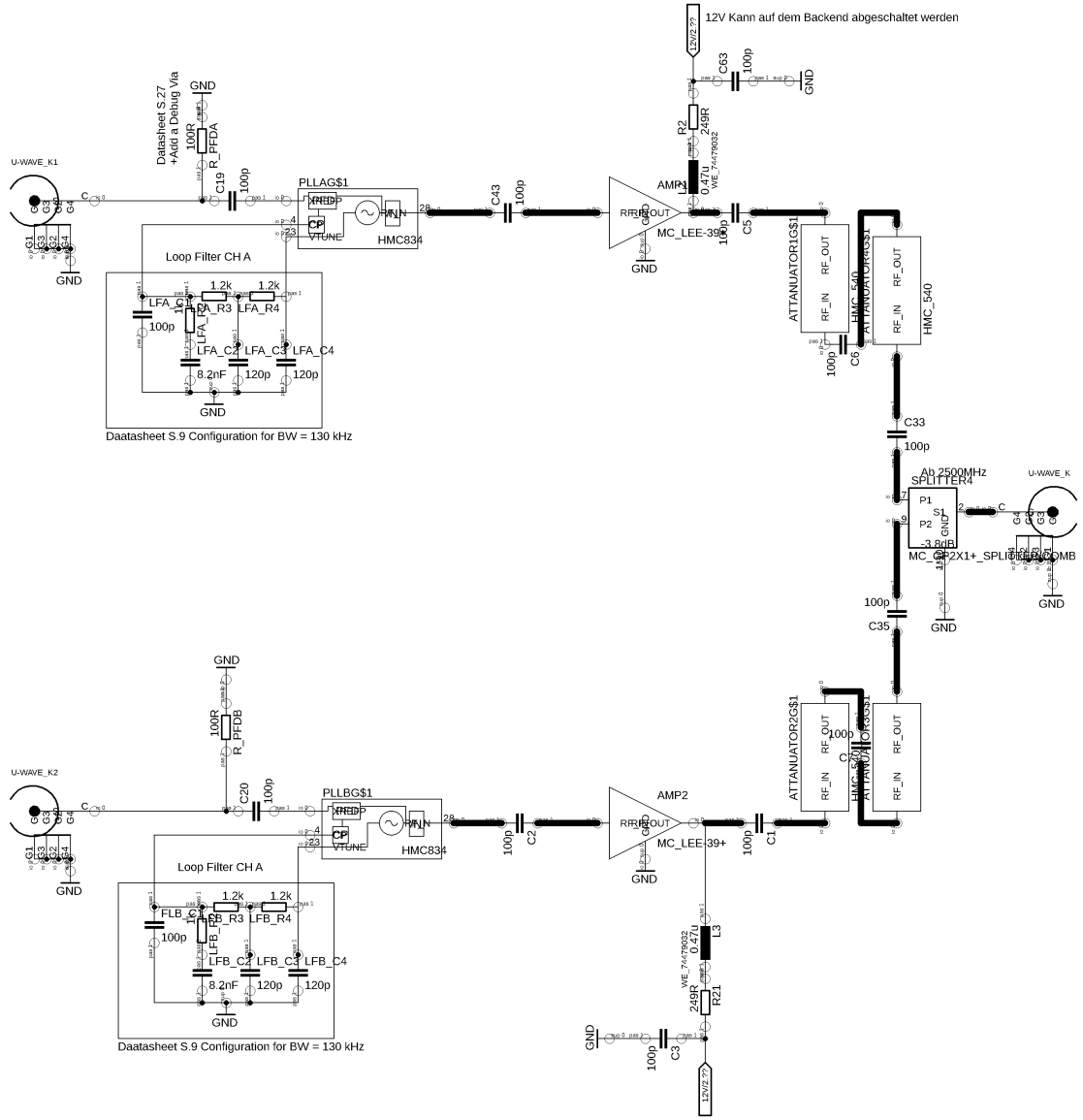

Figure B.39: Schematic of the microwave front-end side 2. This sheet contains the microwave output stage. The signal from the two HMC 834 PLLs (PLLA and PLLB) is amplified by the two amplifiers of type Minicircuits LEE-39+ (AMP1 and AMP2), passes two attenuators per channel (ATTENUATOR1-4). The two channels are combined in the splitter combiner SPLITTER4. SPLITTER 4 differs for the rubidium and the potassium variant between a Minicircuits GP2-X1+ (rubidium) and a Minicircuits GP2-S1+ (potassium).

B.0.18 Layout of the chip and coil current driver

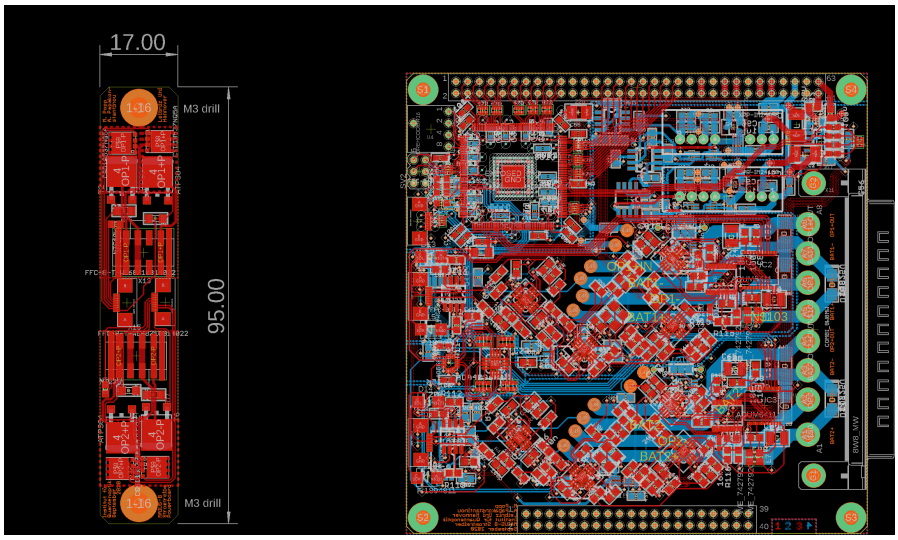

Figure B.40: Layout of the chip and coil current driver. The layout shows the main board and the power electronics aluminum board (left). The power board can be mounted on the back heat sink of a stack.

B.0.19 Schematic of the chip and coil current driver

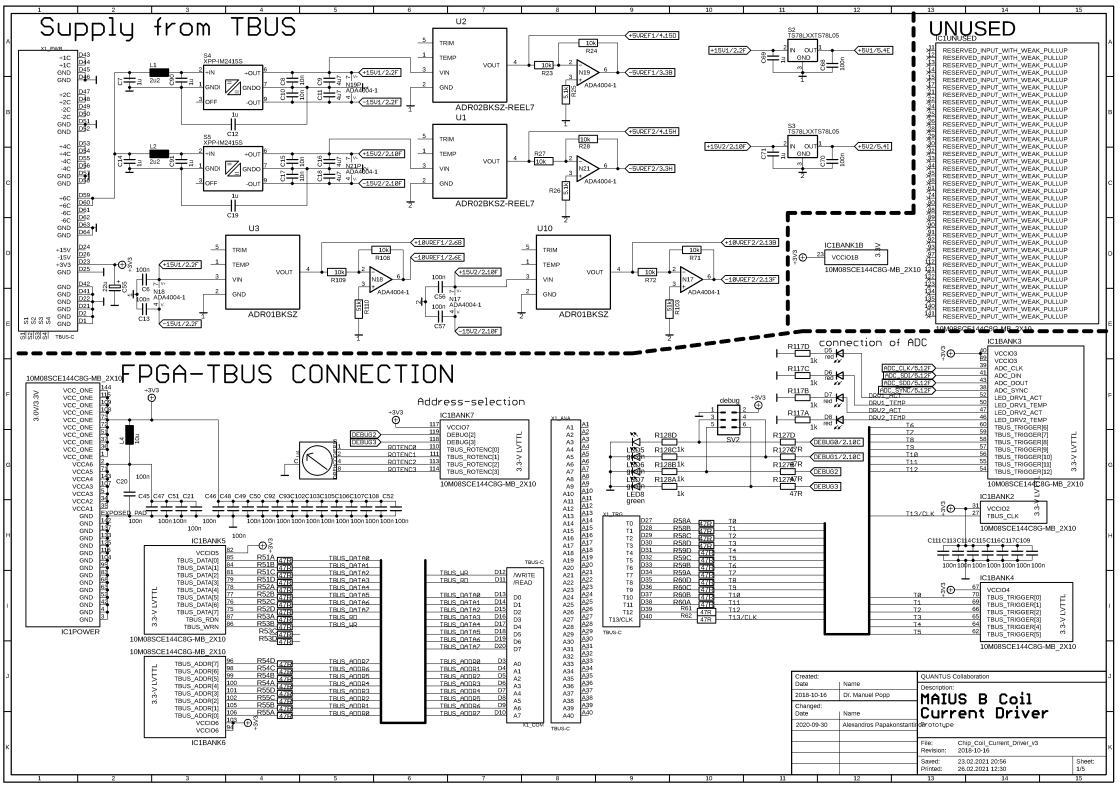

Figure B.41: Schematic of the chip and coil current driver. This sheet shows connections to the TBus connectors.

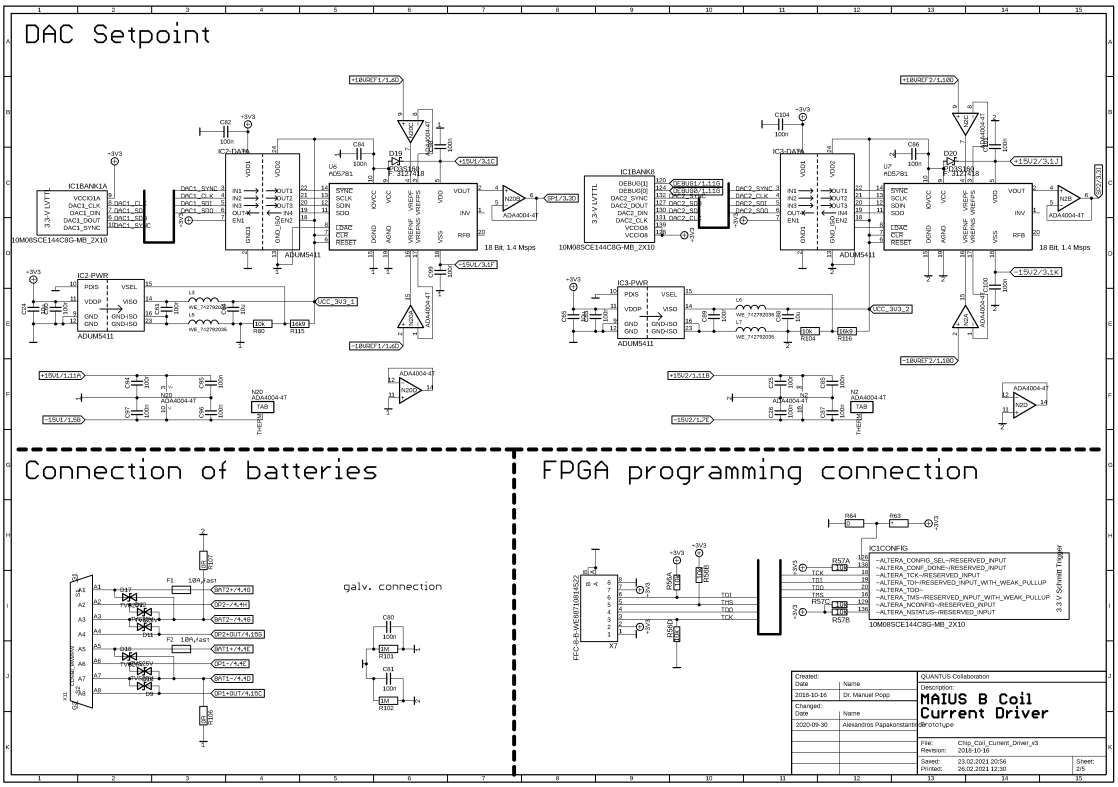

Figure B.42: Schematic of the chip and coil current driver. This sheet shows the connection to the batteries and the DAC for the setpoint control.

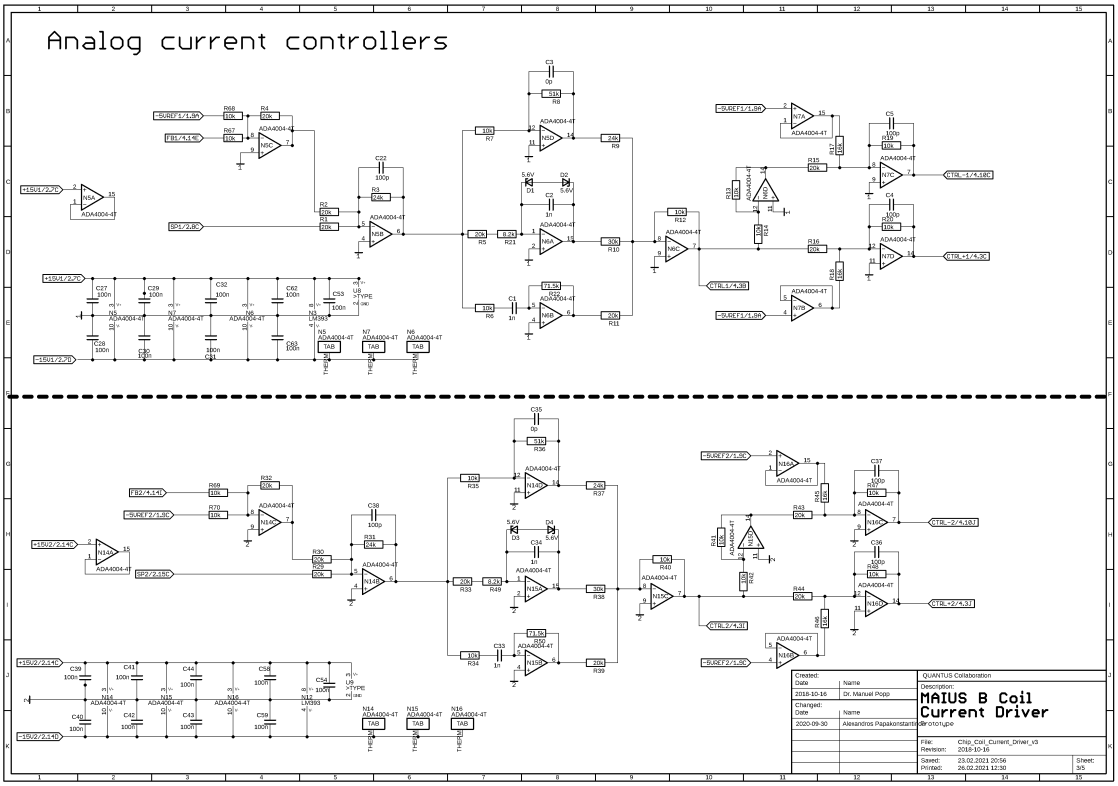

Figure B.43: Schematic of the chip and coil current driver. This sheet shows the analog control PID of the current driver.

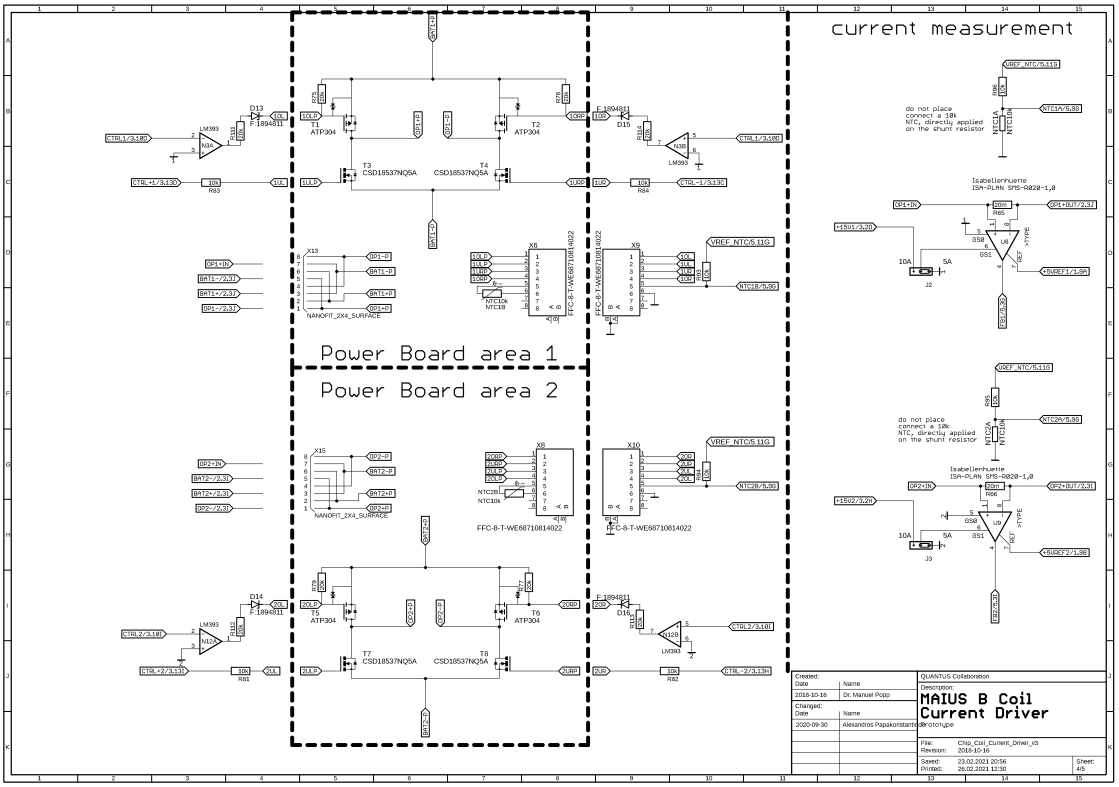

Figure B.44: Schematic of the chip and coil current driver. This sheet shows the power boards circuit

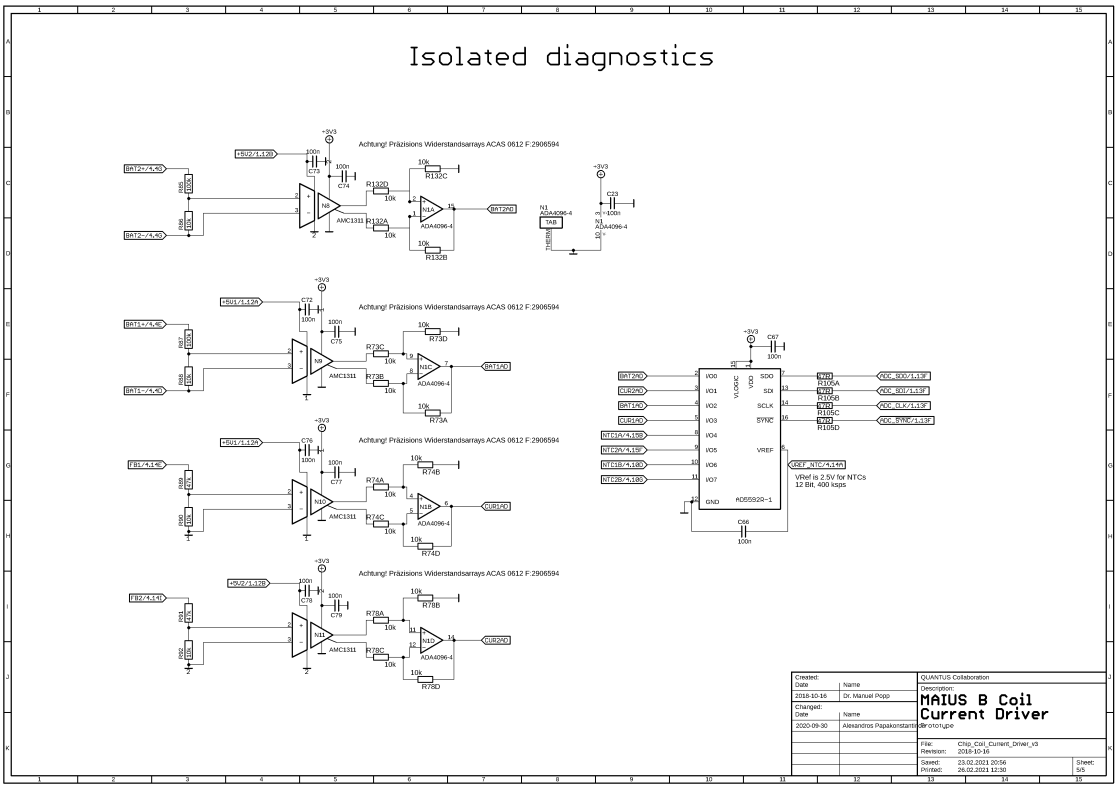

Figure B.45: Schematic of the chip and coil current driver. This sheet the monitoring circuits.

B.1 Battery module

B.1.1 List of consumers inside the scientific payload

Component	Power 2C	Power 6C	Power 2C extra	Power 6C extra
BAT	0.5 W	0.5 W	0	0
LE	129 W	129 W	0	0
PP	8 W	49 W	0	0
EL	35 W	143 W	17 W	96 W
Total	156 W	354 W	17 W	96 W
Operating time:	34 min	39 min	60 min	186 min

Table B.1: List of consumers inside the scientific payload and operating time estimation of the battery module. The battery module also consumes power from the ground support or the service module. The power is given in rms.

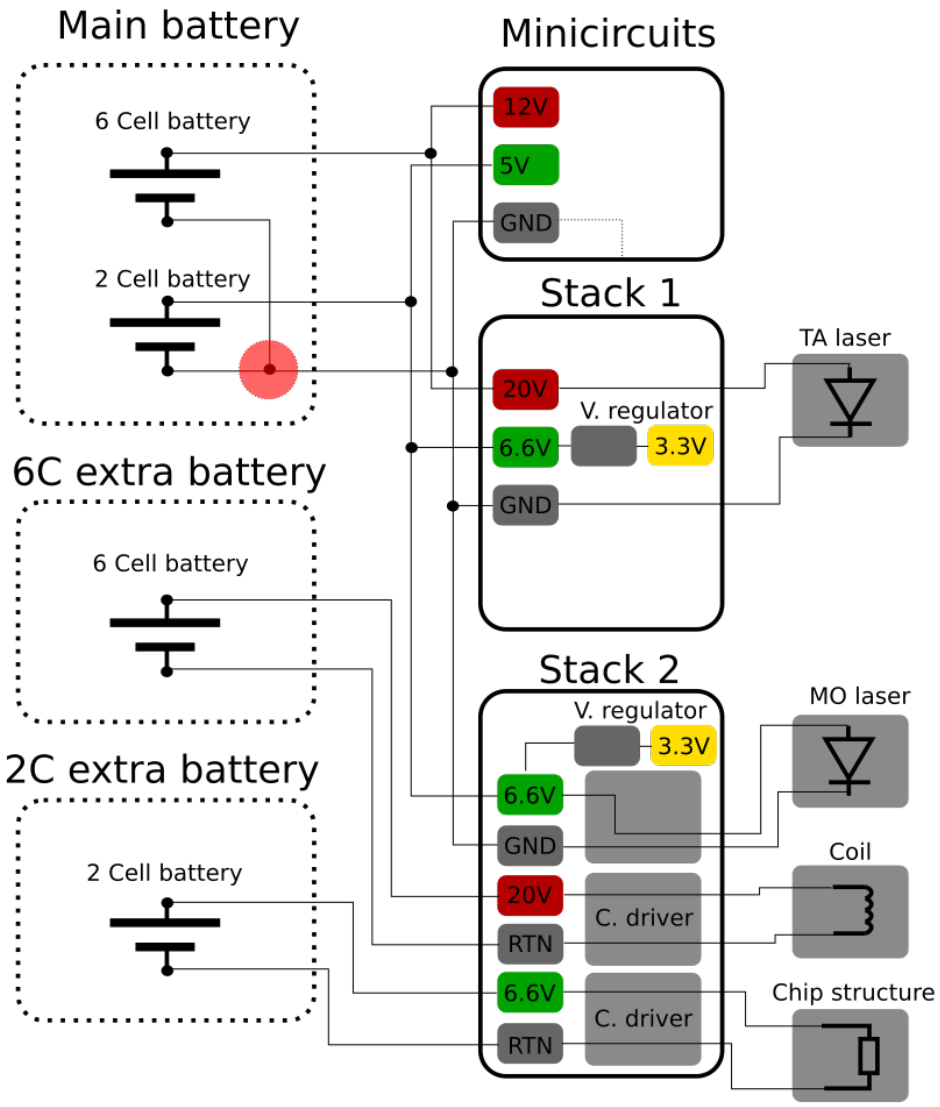

Figure B.46: Schematic picture of the overall supply and grounding concept. The main battery supplies the TBus Stacks. The outputs of chip and coil current drivers are supplied by the two cell and six cell extra batteries. The red marked grounding point in the main battery is the central grounding point of the electronic system. The dashed line between mini circuits ground input and case represents an expected parasitic connection due to the shielding of the SMA connectors.

B.1.2 extra batteries

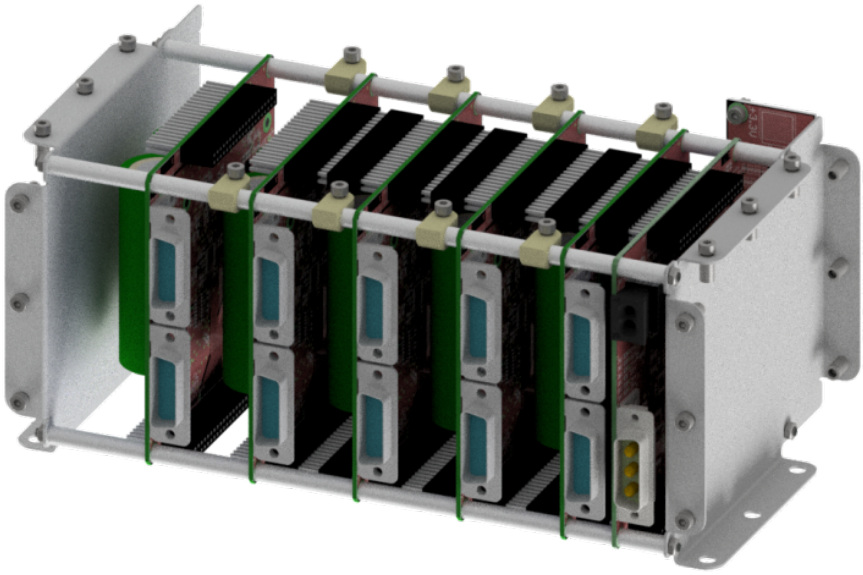

Figure B.47: CAD drawing of the two cell extra battery stack, the casing is partially not shown.

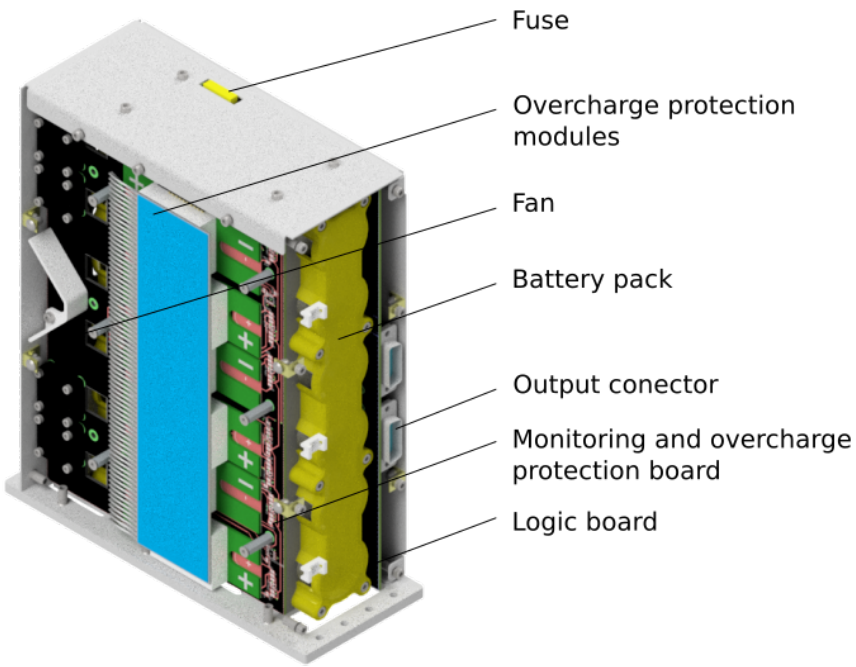

Figure B.48: CAD drawing of the six cell extra battery, the casing is partially not shown.

B.2 Laser electronic module

B.2.1 Stack case for TBus cards

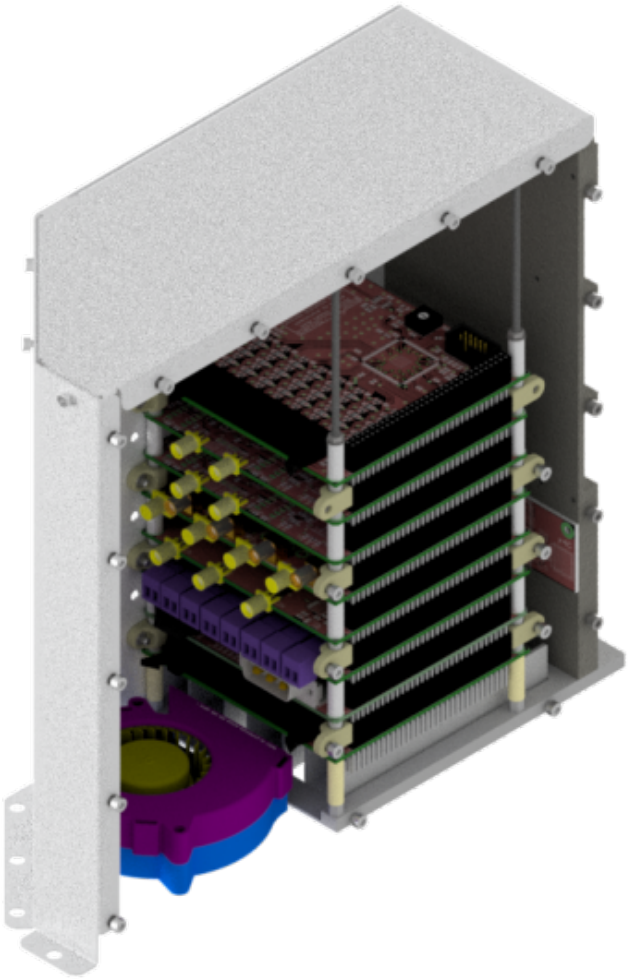

Figure B.49: CAD model of the rubidium laser control stack inside the standard TBus case for the MAIUS-B payload. The back-panel acts as heat-sink. The space in front of the stack leaves room for connectors and wiring between stack and patch-panel. A fan is mounted at the bottom of the case.

B.2.2 Stack case for the chip and coil current driver stack

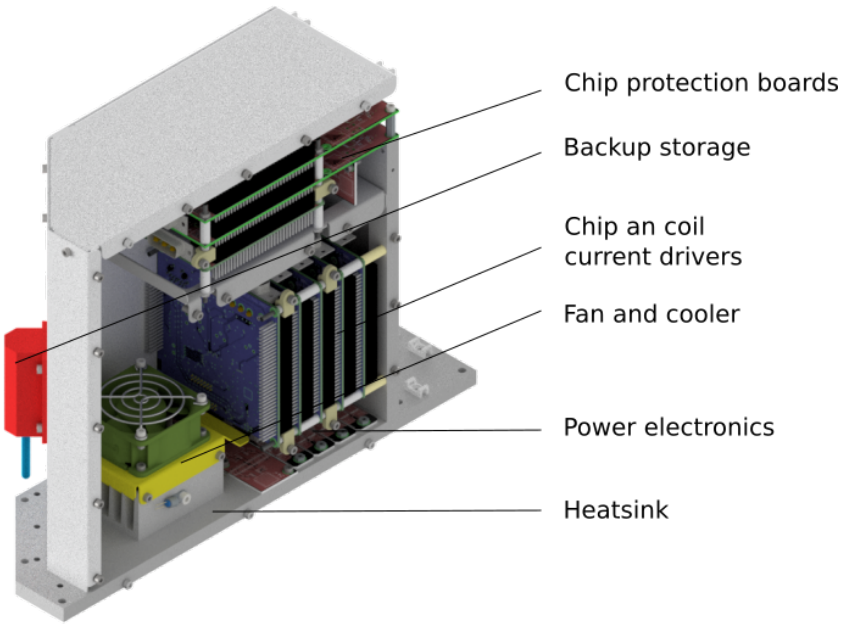

Figure B.50: CAD model of the chip and coil current driver stack inside the modified standard TBus case for the MAIUS-B payload. The bottom panel acts as heat-sink. The stack is tilted by 90 degrees to to fit the power boards directly on the heat-sink. In the upper part the chip safety boards are visible. The space in front of the stack leaves room for connectors and wiring between stack and patch panel. A fan is mounted at the bottom of the case.

B.2.3 Amplifier system for beat and spectroscopy signals

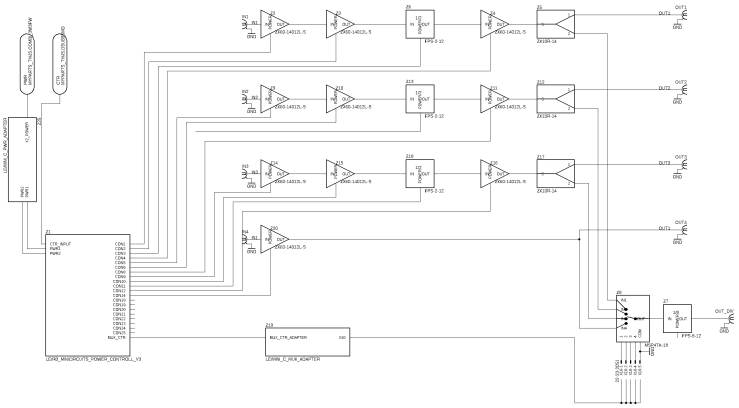

Figure B.51: Schematic of the amplifier system for beat and spectroscopy signals.

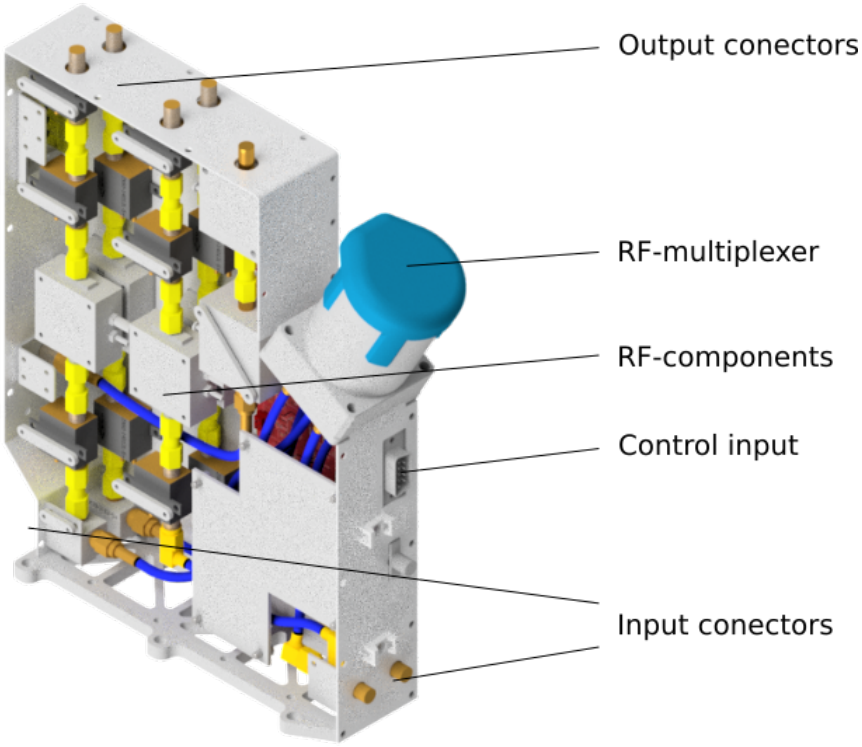

Figure B.52: CAD model of the Minicircuits module, the side panel of the case is not shown. The components are labeled.

B.3 Electronic stack inside the physics package

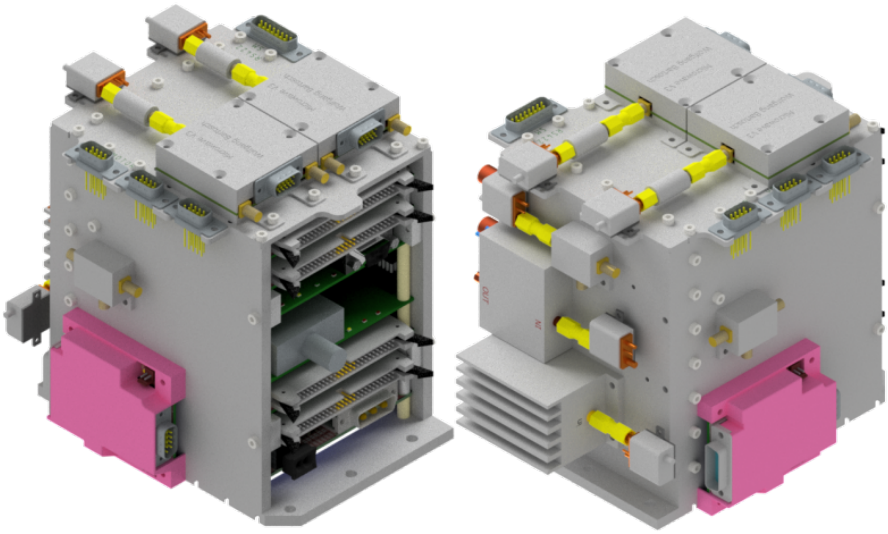

Figure B.53: CAD model of the electronic stack inside the physics package. The stack is shown from two different angles. LHS: Front view with TBus cards visible. RHS: Back view with power amplifiers of the evaporation system visible.

B.4 Other electronics

B.4.1 Switching circuit for power amplifier

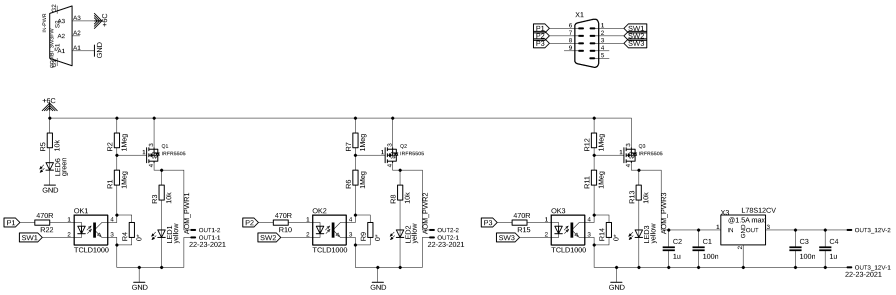

Figure B.54: Schematic of the power amplifier switching circuit.

B.4.2 connection cable for the coupling of disturbances

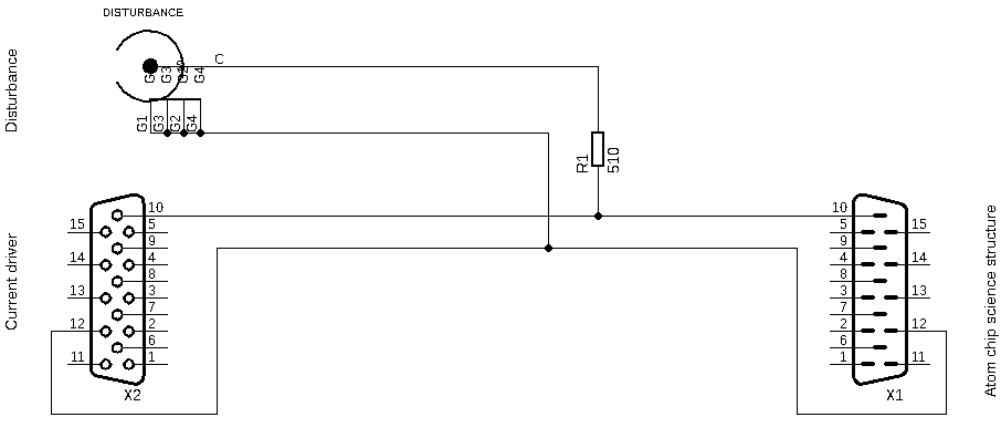

Figure B.55: Schematic of the cable used to create a disturbance on the current driver. The disturbance can be coupled in from a signal generator via the SMA connector X1. X1 is connected over a 510 Ohm resistor to the supply line of the atom chip (pins 10 and 12)

B.5 Literature

Bibliography

[1] A123 Systems. Technical data scheet of: A123 Systems ANR26650M1B, 2500 mAh. Available at: https://shop.lipopower.de/A123-Systems-ANR26650M1B-2500-mAh.

[2] Benjamin P Abbott, Richard Abbott, TD Abbott, MR Abernathy, Fausto Acernese, Kendall Ackley, Carl Adams, Thomas Adams, Paolo Addesso, RX Adhikari, et al. Observation of gravitational waves from a binary black hole merger. *Physical review letters*, 116(6):061102, 2016.

[3] Abracon. Technical data sheet of: Oven controlled crystal oscillator. Available at: https://abracon.com/Precisiontiming/AOCJY2.pdf, (09.02.2021).

[4] Analog Devices. Technical data sheet of: Positive control attenuator HMC 540. Available at: https://www.analog.com/media/en/technical-documentation/data-sheets/hmc540.pdf, (09.09.2020).

[5] Analog Devices. Technical data sheet of: HMC834 Fractional-n Pll with integrated VCO. Available at: https://www.analog.com/media/en/technical-documentation/data-sheets/hmc834.pdf, (09.09.2020). 2020.

[6] ASM. Webcatalog for aerospace materials. Available at: http://asm.matweb.com/search/SpecificMaterial.asp?bassnum=MTP641, (29.05.2020) .

[7] Atmel. Technical data sheet of: ATmega8. Available at https://ww1.microchip.com/downloads/en/DeviceDoc/Atmel-2486-8-bit-AVR-microcontroller-ATmega8_L_datasheet.pdf,(25.08.2020).

[8] D. Becke1 J. Böhm K. Döringshoff M. Elsen J. Grosse M. D. Lachmann M.Mihm M. Popp T. Wendrich E. Rasel B. Piest, W. Bartosch and W. Ertmer. Maius-2/-3: A system for two-species atom interferometry in space.

[9] Wolfgang Bartosch. Automatic frequency lock of a diode laser for rubidium spectroscopy. *Bachelor thesis*, 2013. Bachelorarbeit, Leibniz Univerität Hannover, Institut für Quantenoptik.

[10] Dennis Becker, Maike D Lachmann, Stephan T Seidel, Holger Ahlers, Aline N Dinkelaker, Jens Grosse, Ortwin Hellmig, Hauke Müntinga, Vladimir Schkolnik, Thijs Wendrich, et al. Space-borne bose–einstein condensation for precision interferometry. *Nature*, 562(7727):391–395, 2018.

[11] Katrin Becker, Melanie Becker, and John H Schwarz. *String theory and M-theory: A modern introduction*. Cambridge University Press, 2006.

[12] M Billo, M Henneaux, A Sevrin, S Theisen, W Troost, S Vandoren, and A Van Proeyen. Classical and quantum gravity. *Classical and Quantum Gravity*, 20(12), 2003.

[13] James Henry Breasted. *The Edwin Smith Surgical Papyrus: published in facsimile and hieroglyphic transliteration with translation and commentary in two volumes*, volume 3. University of Chicago Press Chicago, 1930.

[14] Alessia Burchianti, Chiara D'Errico, Sara Rosi, Andrea Simoni, Michele Modugno, Chiara Fort, and Francesco Minardi. Dual-species bose-einstein condensate of k 41 and rb 87 in a hybrid trap. *Physical Review A*, 98(6):063616, 2018.

[15] Alexander Cronin, Jörg Schmiedmayer, and David Pritchard. Optics and interferometry with atoms and molecules. *Review of Modern Physics*, 81:1051, 07 2009.

[16] O'Leary De Lacy. *How Greek science passed to the Arabs*. Ares Publishers, 1949.

[17] Wolfgang Demtröder. Experimentalphysik 3, 1996.

[18] Mona Desai, Rebecca Forrest, Charles Horton, Alex Ignatiev, Mark Sterling, John Strozier, Charles Justiz, and Ron Sega. Vacuum and flow field results from the wake shield facility flight experiment. In *AIP conference proceedings*, volume 325, pages 323–330. American Institute of Physics, 1995.

[19] Analog Devices. Quad-Channel Isolators with Integrated DC-to-DC Converters. Available at: https://www.analog.com/media/en/technical-documentation/data-sheets/ADuM5410-5411-5412.pdf, (22.02.2021) .

[20] A Di Carli, CD Colquhoun, S Kuhr, and E Haller. Interferometric measurement of micro-g acceleration with levitated atoms. *New Journal of Physics*, 21(5):053028, 2019.

[21] Matthieu Dupont-Nivet, Mathias Casiulis, Théo Laudat, Christoph I Westbrook, and Sylvain Schwartz. Microwave-stimulated raman adiabatic passage in a bose-einstein condensate on an atom chip. *Physical Review A*, 91(5):053420, 2015.

[22] Albert Einstein. *The meaning of relativity: Including the relativistic theory of the non-symmetric field*, volume 32. Princeton university press, 2014.

[23] M. Elsen, J. Grosse, R. Rasel, C.Braxmaier, and the MAIUS-Team. The pathway to launch the maius-2/3 payload on a sounding rocket. In *Proc. of the 70th International Astronautical Congress*, 2019.

[24] Michael Elsen. Title not yet determined. Doktorarbeit, Univerität Bremen.

[25] Michael Elsen, Baptist Piest, Wolfgang Bartosch, and et al. A Dual-Species Atom Interferometer Payload for Operation on Sounding Rockets.

[26] FAULHABER. Technical data scheet of: Zwei Phasen, 24 Schritte pro Umdrehung Schrittmotor. Available at: https://www.faulhaber.com/de/produkte/schrittmotoren/.

[27] Ferdinand-Braun-Institut. Micro-integratedmaster oscillator power amplifier.

[28] FLIR. Technical data scheet of: Grasshopper 3 USB-3 vision. Available at: https://flir.app.boxcn.net/s/859w5hl6yv25yo4c5aqvdnl2ask34n4i/file/418656969139.

[29] Ron Folman, Peter Kruger, Jörg Schmiedmayer, Johannes Denschlag, and Carsten Henkel. Microscopic atom optics: from wires to an atom chip. *arXiv preprint arXiv:0805.2613*, 2008.

[30] Howard Georgi and Sheldon L Glashow. Unity of all elementary-particle forces. *Physical Review Letters*, 32(8):438, 1974.

[31] Gooch and Housego. Technical data scheet of: FIBER COUPLED AOM. Available at: https://gandh.com/wp-content/uploads/2018/10/GH-DS-FO-Fiber-Q-application-note.pdf.

[32] Jens Herbig, Tobias Kraemer, Michael Mark, Tino Weber, Cheng Chin, Hanns-Christoph Nägerl, and Rudolf Grimm. Preparation of a pure molecular quantum gas. *Science*, 301(5639):1510–1513, 2003.

[33] Waldemar Herr. Eine kompakte quelle quantenentarteter gase hohen flusses für die atominterferometrie unter schwerelosigkeit. 2013. Doktorarbeit, Leibniz Univerität Hannover, Institut für Quantenoptik.

[34] Paul Horowitz and Winfield Hill. *The art of electronics*. Cambridge Univ. Press, 1989.

[35] Ferdinant Braun Institut. Technical data scheet of: 3rd generation 4th generation ECDL MOPA. Available in internal documentation.

[36] Ferdinant Braun Institut. Technical data scheet of: 3rd generation DFB MO. Available in internal documentation.

[37] Intel. Technical datascheet of: Intel MAX 10 FPGA. Available at: https://www.intel.com/content/dam/www/programmable/us/en/pdfs/literature/hb/max-10/m10_datasheet.pdf.

[38] Carsten Klempt, T Van Zoest, T Henninger, E Rasel, Wolfgang Ertmer, J Arlt, et al. Ultraviolet light-induced atom desorption for large rubidium and potassium magneto-optical traps. *Physical Review A*, 73(1):013410, 2006.

[39] Peter Krüger, Xiao Luo, Matthias W Klein, Karolina Brugger, Albrecht Haase, Stephan Wildermuth, Sönke Groth, Israel Bar-Joseph, Ron Folman, and Jörg Schmiedmayer. Trapping and manipulating neutral atoms with electrostatic fields. *Physical review letters*, 91(23):233201, 2003.

[40] Maike Diana Lachmann. Materiewelleninterferenzenim weltraum.

[41] Claus Lämmerzahl. The search for quantum gravity effects. In *Quantum Gravity*, pages 15–39. Springer, 2006.

[42] LEM. Technical data scheet of: Current transducer CASR series. Available at: https://docs.rs-online.com/f58a/0900766b8142e857.pdf.

[43] KG Libbrecht and John L Hall. A low-noise high-speed diode laser current controller. *Review of scientific instruments*, 64(8):2133–2135, 1993.

[44] LINANO. Technical data scheet of: Balancer 2, 1.5 A 1 Zelle LiFePo4 LiNANO, Lastmodul mit LED (95mm). Available at: https://shop.lipopower.de/Balancer-15A-fuer-1-Zelle-LiFePo4-LiNANOZ-Lastmodul-mit-LED-95mm.

[45] LINANO. Technical data scheet of: Balancer 2,1A 1 Zelle LiFePo4 LiNANO, Lastmodul mit LED (95mm). Available at: https://shop.lipopower.de/Balancer-21A-fuer-1-Zelle-LiFePo4-LiNANOZ-Lastmodul-mit-LED-95mm.

[46] Meerstetter. Technical datasheet of: Meerstetter TEC-1091 TEC. Available at: https://www.meerstetter.ch/de/produkte/tec-controller/tec-1091.

[47] S Merlet, Q Bodart, N Malossi, A Landragin, F Pereira Dos Santos, O Gitlein, and L Timmen. Comparison between two mobile absolute gravimeters: optical versus atomic interferometers. *Metrologia*, 47(4):L9, 2010.

[48] Harold J Metcalf and Peter Van der Straten. *Laser cooling and trapping*. Springer, 1999.

[49] Microchip. Technical data scheet of: 16-Bit Analog-to-Digital Converter. Available at: http://ww1.microchip.com/downloads/en/DeviceDoc/22072b.pdf.

[50] Microsemi. Technical data scheet of: IGLOO2 FPGA and SmartFusion2 SoC FPGA family. Available at: https://www.microsemi.com/product-directory/fpgas/1688-igloo2.

[51] Minicircuits. Technical data scheet of: Power splitter/combiner gp2s1+. available at: https://www.minicircuits.com/pdfs/GP2S1+.pdf.

[52] Minicircuits. Technical data scheet of: Power splitter/combiner gp2x1+ 2800 - 7200 mhz. available at: https://www.minicircuits.com/pdfs/GP2X1+.pdf.

[53] Minicircuits. Technical data scheet of: Sp4t switch msp4ta-18+. available at: https://www.minicircuits.com/pdfs/MSP4TA-18+.pdf.

[54] Minicircuits. Technical data scheet of: Surface MountMonolithic Amplifier LEE-39+. Available at: https://www.minicircuits.com/pdfs/LEE-39+.pdf.

[55] Minicircuits. Technical data scheet of: Ultra wide band amplifier zx60-14012l. available at: https://www.minicircuits.com/pdfs/ZX60-14012L.pdf.

[56] Minicircuits. Technical data scheet of: Wideband Microwave Amplifier. Available at: https://www.minicircuits.com/pdfs/ZX60-183A-S+.pdf.

[57] Minicircuits. Technical data scheet of: ZVE-8G+. Available at: https://www.minicircuits.com/pdfs/ZVE-8G.pdf.

[58] Isaac Newton, Daniel Bernoulli, Colin MacLaurin, and Leonhard Euler. *English translation of: Philosophiae naturalis principia mathematica*, volume 1. excudit G. Brookman; impensis TT et J. Tegg, Londini, 1833.

[59] Opto Electronics. Technical data scheet of: AMPA-B-30. Available at: http://acoustooiw.cluster023.hosting.ovh.net/aaoptoelectronic.com/wp-content/uploads/documents/AMPA-1W-2.5W-2014.pdf.

[60] Ariovaldo Felix Palmerio, José Pedro Claro Peres da Silva, Peter Turner, and Wolfgang Jung. The development of the vsb-30 sounding rocket vehicle. In *European Rocket and Balloon Programmes and Related Research*, volume 530, pages 137–140, 2003.

[61] Alexandos Papakonstantinou. Title not yet determined. Doktorarbeit, Leibniz Univerität Hannover, Institut für Quantenoptik.

[62] PCO. Technical data scheet of: Pco 1400 ccd camera. available at: https://www.pco.de/de/support/schnittstellentreiber/scientific-kameras/pco1400/.

[63] Pfeiffer. Technical data scheet of: IKR 270, metallgedichtet, DN 40 CF-F. Available at: https://www.pfeiffer-vacuum.com/productPdfs/PTR21251.de.pdf.

[64] Baptist Piest. Double-species bose-einsteincondensation on an atom chip for a sounding rocket mission. Diplomarbeit, Leibniz Univerität Hannover, Institut für Quantenoptik.

[65] Manuel André Popp. Compact, low-noise current drivers for quantum sensors with atom chips. 2018. Diplomarbeit, Leibniz Univerität Hannover, Institut für Quantenoptik.

[66] Ernst M Rasel, Markus K Oberthaler, Herman Batelaan, Jörg Schmiedmayer, and Anton Zeilinger. Atom wave interferometry with diffraction gratings of light. *Physical Review Letters*, 75(14):2633, 1995.

[67] Ernst M Rasel, Dennis Schlippert, and Etienne Wodey. Der VLBAI-Teststand: Ein Fallturm für Atome. *Unimagazin 3/4 (2018)*, 2018. Leibniz Univerität Hannover, Institut für Quantenoptik.

[68] G Reinaudi, T Lahaye, Z Wang, and D Guéry-Odelin. Strong saturation absorption imaging of dense clouds of ultracold atoms. *Optics letters*, 32(21):3143–3145, 2007.

[69] Allen F Repko. *Interdisciplinary research: Process and theory*. Sage, 2008.

[70] RIGOL. Technical data scheet of: Function- Arbitrary Waveform Generator. Available at: https://www.rigol.eu/Public/Uploads/uploadfile/files/20201109/20201109215420_5fa94a0cb2392.pdf.

[71] Rohde und Schwarz. Technical data scheet of: SMC100A Signal Generator. Available at: https://www.rohde-schwarz.com/de/produkt/smc100a-produkt-startseite_63493-10181.html.

[72] RTD.com. Technical data scheet of: CPU Board IDAN-CMA34CRQ2100HR. Available at: https://www.rtd.com/NEW_manuals/hardware/cpumodules/CMA34CR_BDM610000083J.pdf.

[73] Jan Rudolph, Waldemar Herr, Christoph Grzeschik, Tammo Sternke, Alexander Grote, Manuel Popp, Dennis Becker, Hauke Müntinga, Holger Ahlers, Achim Peters, et al. A high-flux bec source for mobile atom interferometers. *New Journal of Physics*, 17(6):065001, 2015.

[74] Maral Sahelgozin. *Design and construction of a transportable quantum gravimeter and realization of an atom-chip magnetic trap*. PhD thesis, Hannover: Institutionelles Repositorium der Leibniz Universität Hannover, 2019.

[75] Max Schiemangk, Kai Lampmann, Aline Dinkelaker, Anja Kohfeldt, Markus Krutzik, Christian Kürbis, Alexander Sahm, Stefan Spießberger, Andreas Wicht, Götz Erbert, et al. High-power, micro-integrated diode laser modules at 767 and 780 nm for portable quantum gas experiments. *Applied optics*, 54(17):5332–5338, 2015.

[76] Stephan Schlamminger, K-Y Choi, Todd A Wagner, Jens H Gundlach, and Eric G Adelberger. Test of the equivalence principle using a rotating torsion balance. *Physical Review Letters*, 100(4):041101, 2008.

[77] Dennis Schlippert, Jonas Hartwig, Henning Albers, Logan L Richardson, Christian Schubert, Albert Roura, Wolfgang P Schleich, Wolfgang Ertmer, and Ernst M Rasel. Quantum test of the universality of free fall. *Physical Review Letters*, 112(20):203002, 2014.

[78] Karl Ulrich Schreiber, T Klügel, J-PR Wells, RB Hurst, and A Gebauer. How to detect the chandler and the annual wobble of the earth with a large ring laser gyroscope. *Physical Review Letters*, 107(17):173904, 2011.

[79] Stephan Tobias Seidel. Eine quelle für die interferometrie mit bose-einsteinkondensaten auf höhenforschungsraketen. 2014. Diplomarbeit, Leibniz Univerität Hannover, Institut für Quantenoptik.

[80] Christian Spindeldreier. *Design und Evaluation vonHardware-Architekturen zur Stabilisierungverstimmbarer Diodenlaser unterWeltraumbedingungen*. PhD thesis.

[81] Andreas Stamminger, Josef Ettl, Jens Grosse, Marcus Hörschgen-Eggers, Wolfgang Jung, Alexander Kallenbach, Georg Raith, Wolfram Saedtler, Stephan Seidel, John Turner, et al. Maius-1-vehicle, subsystems design and mission operations. In *Proceedings 22nd ESA Symposium on European Rocket and Balloon Programmes and Related Research*, pages 183–190. ESA Communications, 2015.

[82] Daniel A Steck. Rubidium 87 d line data (2003). http://steck.us/alkalidata/rubidium87numbers.pdf, 2003.

[83] TEN. Isolating DC/DC converter. Available at: https://www.tracopower.com/de/deu/din-rail/dcdc-wandler, (22.02.2021) .

[84] Wendrich Thijs. Lasus Wiki Electronics, Leibniz Univerität Hannover, Institut für Quantenoptik. Lasus Wiki Electronics, 2013.

[85] TG Tiecke. Properties of potassium. *University of Amsterdam, The Netherlands, Thesis*, pages 12–14, 2010.

[86] Pierre Touboul, Gilles Métris, Manuel Rodrigues, Yves André, Quentin Baghi, Joël Bergé, Damien Boulanger, Stefanie Bremer, Patrice Carle, Ratana Chhun, et al. Microscope mission: first results of a space test of the equivalence principle. *Physical review letters*, 119(23):231101, 2017.

[87] Rohde und Schwarz. Technical data scheet of: FSWP Phase Noise Analyzer. Available at: https://scdn.rohde-schwarz.com/ur/pws/dl_downloads/dl_common_library/dl_brochures_and_datasheets/pdf_1/FSWP_dat-sw_en_3607-2090-22_v0900.pdf.

[88] Roland v. Eötvös, Desiderius Pekár, and Eugen Fekete. Beiträge zum Gesetze der Proportionalität von Trägheit und Gravität. *Annalen der Physik*, 373(9):11–66, 1922.

[89] Tim van Zoest, N Gaaloul, Y Singh, H Ahlers, W Herr, ST Seidel, W Ertmer, E Rasel, M Eckart, E Kajari, et al. Bose-einstein condensation in microgravity. *Science*, 328(5985):1540–1543, 2010.

[90] Jerry Wellington. *Secondary science: Contemporary issues and practical approaches*. Routledge, 2002.

[91] JG Williams, RH Dicke, PL Bender, CO Alley, WE Carter, DG Currie, DH Eckhardt, JE Faller, WM Kaula, JD Mulholland, et al. New test of the equivalence principle from lunar laser ranging. *Physical Review Letters*, 36(11):551, 1976.

B.6 List of abbreviations

AC Alternating Current
ADC Analog Digital Converter
AOM Acousto-Optic Modulator
ARP Adiabatic Rapid Passage
ARCS-System Attitude and Rate Control System
BEC Bose-Einstein-Condensate
BECCAL Bose Einstein Condensates and Cold Atom Laboratory
CCD Charge-Coupled Device
CPLD Complex Programmable Logic Devices
DAC Digital Analog Converter
DC Direct Current
DDS Direct Digital Synthesis
DFB Distributed Feedback
DKC Delta Kick Colimation
DLR Deutsches Zentrum für Luft- und Raumfahrt
DLL Dynamic Link Library
ECDL External Cavity Diode Laser
FPGA Field Programmable Gate Array
GSE Ground Support Equipment
HV High Voltage
IGP Ion Getter Pump
ISS International Space Station
LASUS Laser Unter Schwerelosigkeit
LIAD Light-Induced Atomic Desorption
LSB Least Significant Bit
LVDS Low Volt Differential Signal
MO Maser Oscillator
MOPA Master Oscillator Power Amplifier
MOT Magneto-Optical Trap
MTS Modulation Transfer Spectroscopy
NASA National Aeronautics and Space Administration
PFD Phase Frequency Detector
PID Proportional Integral Derivative Controller
PLL Phase Locked Loop
POF Plastic Optical Fibre
QUANTUS Quantengase unter Schwerelosigkeit
RF Radio Frequency

SPI Serial Peripheral Interface

SSC Swedish Space Corporation

STIRAP Stimulated Raman Adiabatic Passage

TA Tapered Amplifier

TEC Thermo Electric Cooler

TSP Titanium Sublimation Pump

UHV Ultra High Vacuum

VCO Voltage Controlled Oscillator

ZARM Zentrum für angewandte Raumfahrttechnologie und Mikrogravitation

APPENDIX C

Danksagung und Eigenständigkeitserklärung

C.1 Danksagung

Diese Arbeit wurde von vielen verschiedenen Menschen überhaupt erst ermöglicht, von denen ich einigen an dieser Stelle danken möchte. Danken möchte ich zuerst meinen Kollegen in der MAIUS Kollaboration, die für mich ein sehr gutes Arbeitsumfeld geschaffen haben und immer für alle Fragen und Anmerkungen offen waren. Namentlich möchte ich dabei meine direkten Kollegen Maike, Baptist und Alexandros danken. Besonderer Dank aber gilt Thijs Wendrich, der meinen weg vom Studium bis zum heutigen Tag mit unendlicher Geduld begleitet hat. Und immer, egal wie oft ich fragen musste, auf alle Fragen geantwortet hat. Weiterhin danke ich Ernst M. Rasel für seine bemerkenswerte Unterstützung und sein Verständnis während meiner Promotion. Auch möchte ich an dieser Stelle meinem Lehrmeister Dirk Papenburg und den Gesellen meiner Lehrfirma danken, die das Fundament meiner Ausbildung gelegt haben. Ebenso gilt ein großer Dank meinen Eltern Martina und Stefan, ohne die diese Promotion nicht möglich gewesen wäre. Zu guter Letzt gelten Dank und Entschuldigung meiner Frau Janina und meinem Sohn Kjell. Die Jahre dieser Promotion waren nicht immer gut und dass die beiden trotz aller Widerlichkeiten diese Zeit mit mir duchgestanden haben zeugt von Ihrer Stärke.

C.2 Eigenständigkeitserklärung

Erklärung der Eigenständigkeit Hiermit versichere ich, die vorliegende Arbeit eigenständig verfasst und keine anderen als die angegebenen Quellen und Hilfsmittel benutzt sowie die Zitate deutlich kenntlich gemacht zu haben.

(Wolfgang Bartosch)